

**Expected damage to accelerator equipment due to the
impact of the full LHC beam: beam instrumentation,
experiments and simulations.**

DISSERTATION
ZUR ERLANGUNG DES DOKTORGRADES DER NATURWISSENSCHAFTEN
VORGELEGT BEIM FACHBEREICH PHYSIK DER GOETHE-UNIVERSITÄT IN
FRANKFURT AM MAIN.

VON:
Florian BURKART
aus Oberkirch

Frankfurt/ Main 2016
(D30)



vom Fachbereich Physik der Goethe - Universität als Dissertation angenommen.

Dekan: Prof. Dr. Joachim Stroth

Gutachter:

Prof. Dr. Ulrich Ratzinger,

Prof. Dr. Oliver Kester,

Dr. Daniel Wollmann (CERN)

Datum der Disputation: 31.08.2016

Das Schönste, was wir erleben können, ist das Geheimnisvolle. Es ist das Grundgefühl, welches an der Wiege von wahrer Kunst und Wissenschaft steht. Wer es nicht kennt und nicht mehr staunen kann, der ist sozusagen tot und seine Augen erloschen.

Albert Einstein

CONTENTS

1. <i>Introduction</i>	11
2. <i>CERN accelerator chain</i>	15
2.1 High power and high stored energy accelerators	15
2.2 CERN	15
2.3 Accelerator Chain and LHC	16
2.4 Future Hadron Accelerator	21
3. <i>Beam Interaction with material</i>	25
3.1 Particle - matter interaction	25
3.1.1 Cross section and mean free path	25
3.1.2 Charged particle interactions	26
3.1.3 Multiple coulomb scattering	28
3.1.4 Electromagnetic showers	30
3.1.5 Interactions with a nucleus	31
3.1.6 Hadronic showers	32
3.1.7 Nuclear spallation	33
3.2 Warm Dense Matter	33
3.3 Hydrodynamic Tunneling	35
3.4 Simulation Tools	35
3.4.1 FLUKA	35
3.4.2 BIG2	36
4. <i>Failure scenarios for accelerators</i>	37
4.1 Damage potential of proton beams	37
4.2 Machine Protection for LHC	43
4.2.1 LHC - cycle	43
4.2.2 LHC Beam Dump System	44
4.2.3 Collimators	47
4.2.4 Failure cases	49
4.2.5 Failure detection and interlocking	53
4.3 Material damage	54
4.3.1 HiRadMat - Facility	55
4.3.2 Damage experiments	56

5.	<i>Diamond particle detectors for damage experiments</i>	61
5.1	Diamond material	61
5.2	Signal creation in a diamond based detector	63
5.3	Properties of the used dBLMs	65
6.	<i>Hydrodynamic tunneling experiment</i>	67
6.1	Description of the experiment	67
6.2	Target investigations	70
6.3	Cylinder cutting and microscopic analysis	75
6.4	Final result	83
6.5	Removal of the target	86
6.6	Future work - Further analysis of irradiated copper cylinders	88
7.	<i>Simulations with experimental beam parameters</i>	89
7.1	Motivation	89
7.2	Geometry, parameters and simulation routine	90
7.3	Simulation results	93
7.4	Comparison experimental and simulation results	98
8.	<i>Damage simulations for FCC</i>	105
8.1	Future high energy circular colliders	105
8.2	Geometry and simulation routine	105
8.3	Results	106
9.	<i>Characterization of diamond detectors</i>	111
9.1	Motivation	111
9.1.1	Measurements during hydrodynamic tunneling experiment	111
9.2	Efficiency and Linearity of dBLMs	112
9.2.1	BTF at INFN, Frascati	112
9.2.2	Experimental setup	113
9.2.3	Results of dBLM characterization	118
9.2.4	Response measurements	123
9.2.5	Efficiency measurements	126
9.3	Applications of dBLMs	128
9.3.1	Alignment	128
9.3.2	Online tunneling measurement	130
9.3.3	Bunch structure measurements around LHC	130
9.3.4	Abort gap monitoring	131
9.4	Future work - CALIFES	131
10.	<i>Conclusion</i>	133
11.	<i>Deutsche Zusammenfassung</i>	135
12.	<i>Acknowledgements</i>	143
13.	<i>Acronyms used in this PhD thesis</i>	145

ABSTRACT

The Large Hadron Collider (LHC) is the biggest and most powerful particle accelerator in the world, designed to collide two proton beams with particle momentum of 7 TeV/c each. The stored energy of 362 MJ in each beam is sufficient to melt 500 kg of copper or to evaporate about 300 liter of water. An accidental release of even a small fraction of the beam energy can cause severe damage to accelerator equipment. Reliable machine protection systems are necessary to safely operate the accelerator complex. To design a machine protection system, it is essential to know the damage potential of the stored beam and the consequences in case of a failure. One (catastrophic) failure would be, if the entire beam is lost in the aperture due to a problem with the beam dumping system.

This thesis presents the simulation studies, results of a benchmarking experiment, and detailed target investigation, for this failure case. In the experiment, solid copper cylinders were irradiated with the 440 GeV proton beam delivered by the Super Proton Synchrotron (SPS) at the High Radiation to Materials (HiRadMat) facility at CERN. The experiment confirmed the existence of the so-called hydrodynamic tunneling phenomenon for the first time. Detailed numerical simulations for particle-matter interaction with FLUKA, and with the two-dimensional hydrodynamic code, BIG2, were carried out. Excellent agreement was found between the experimental and the simulation results that validate predictions for the 7 TeV beam of the LHC. The hydrodynamic tunneling effect is of considerable importance for the design of machine protection systems for accelerators with high stored beam energy. In addition, this thesis presents the first studies of the damage potential with beam parameters of the Future Circular Collider (FCC).

To detect beam losses due to fast failures it is essential to have fast beam instrumentation. Diamond based particle detectors are able to detect beam losses within a nanosecond time scale. Specially designed diamond detectors were used in the experiment mentioned above. Their efficiency and response has been studied for the first time over 5 orders of bunch intensity with electrons at the Beam Test Facility (BTF) at INFN, Frascati, Italy. The results of these measurements are discussed in this thesis. Furthermore an overview of the applications of diamond based particle detectors in damage experiments and for LHC operation is presented.

1. INTRODUCTION

High energy hadron colliders, like LHC, store bunched hadron beams for several hours to deliver a high collision rate, measured as luminosity, to allow the particle physicists to discover new particles. In the LHC 2808 bunches can be stored with a bunch spacing of 25 ns. At a nominal particle momentum of 7 TeV/c, this leads to a stored beam energy of 362 MJ per beam. This energy is sufficient to melt ~ 500 kg copper. Studies for the next generation of hadron colliders, the so-called Future Circular Collider (FCC), even deal with up to 10600 bunches, a bunch spacing of 25 ns and a particle momentum of 50 TeV/c, which would lead to a stored beam energy of ~ 8.5 GJ.

At the end of luminosity production or in case of a failure the beams have to be dumped on a specially designed beam dump block. This requires a highly reliable and complex safety system. A malfunction of this machine protection system or an accidental release of only a small fraction of the stored energy would lead to massive damage to the accelerator equipment, costly downtime of the accelerator and activation of the surrounding area. One catastrophic failure would be, if the entire beam is lost in the aperture due to a problem with the beam dumping system. Fortunately, the probability for such an accident of this scale is very small, nevertheless, it is very important to be aware of the consequences of such a catastrophic event, if it ever occurs.

This thesis assesses the damage potential of the present LHC and the future FCC by simulating the damage caused by a beam impacting on solid material. To study this behavior detailed numerical simulations for particle-matter interaction with FLUKA were carried out, to evaluate the energy deposition as a function of beam size and beam energy.

In addition, iterative simulations with FLUKA and the two-dimensional hydrodynamic code, BIG2, were performed to study the so-called hydrodynamic tunneling process. To gain confidence in these simulations, an experimental verification of the results was required.

As damage experiments at LHC are not possible, an experiment was carried out at CERNs High Radiation to Materials (HiRadMat) facility. In the experimental phase solid copper cylinders with a total length of 1.5 m were irradiated with the 440 GeV proton beam delivered by the Super Proton Synchrotron (SPS). Different beam sizes and intensities were used to study the hydrodynamic tunneling process. First results were already published in [43]. The experiment was then simulated with a refined simulation model using the experimental beam parameters. The results of these simulations showed that due to the hydrodynamic tunneling process, the penetration length of the full LHC beam and its showers in a target is extended by

more than an order of magnitude compared to that of a single proton. The results are discussed in detail within this thesis.

In addition, a detailed analysis of the target after the irradiation was carried out. Using metal cutting technology, the targets used in the experiments have been dissected into finer pieces for a visual and microscopic inspection in order to establish the precise penetration depth of the protons and their shower.

The results of the simulations were compared to the experimental results. Excellent agreement was found between the experimental and the simulation results that validate predictions for the 7 TeV beam of the LHC.

This gave high confidence in the simulation model with FLUKA and BIG2. The hydrodynamic tunneling effect is of considerable importance for the design of machine protection systems for accelerators with high stored beam energy. To assess for the first time the damage potential of the FCC a simulation model and routine was developed. This thesis presents and discusses the results of these studies.

Comprehensive understanding of beam losses around the LHC is required to ensure full machine protection and efficient operation. As mentioned above bunches in the LHC are separated by 25 ns. This makes a monitoring of bunch-by-bunch losses to a difficult task as most of the particle detectors have a longer response time. The LHC Beam Loss Monitoring (BLM) system, based on ionization chambers, is not adequate to resolve losses with a rise time below some $10 \mu\text{s}$. Ionization chambers are also not adequate to measure very large transient losses, e.g. beam impacting on collimators.

For the experiment in HiRadMat diamond based particle detectors (dBLM) were used for the first time to measure beam losses with a nanosecond time resolution. The dBLMs used during this experiment were specially developed for a high fluence environment, including radiation hardness and 5 ns peak-to-peak resolution. These detector types consist of polycrystalline diamond (pCVD) as active material. In addition, tests were performed during other HiRadMat experiments and they were used to align accelerator equipment to the beam. The analysis of the measurement data showed that a better understanding of the detector properties is required.

It was decided, to characterize the dBLMs with a high intensity electron beam. An experimental setup was designed, including detector holder, collimator, reference detector and read-out system. FLUKA fluence simulations were carried out to evaluate the thickness of the shielding required by radio-protection. The experiments were performed at the Beam Test Facility (BTF) at INFN, Frascati, Italy. The detector efficiency and response has been studied for the first time over 5 orders of bunch intensity, between 10^4 and 10^9 electrons per pulse. In addition, the properties of different read-out systems, standard LHC 50Ω and a specially designed 1Ω system for high fluence applications, were studied concerning sensitivity and saturation limits. The results of this characterization campaign are discussed in detail within this thesis. Furthermore, an overview of the applications of dBLMs in damage experiments and the first step to a detector test stand at CERN are presented. These dBLMs are also used in the LHC to study fast beam losses, for example in the injection and

extraction regions and dust particles falling through the beam, the so-called UFOs.

2. CERN ACCELERATOR CHAIN

This chapter will introduce CERN and its accelerator chain. The present design studies for a future collider will be briefly explained.

2.1 *High power and high stored energy accelerators*

Storage rings like LHC, Hera and Tevatron increased their stored beam energy over the last years. The stored beam energy in the LHC is already a factor 200 higher than it was in the Tevatron. For fast cycling machines, like spallation sources, accelerators for neutrino production or FRIB in Oak Ridge the beam power is the figure of merit. And it will be constantly increased, as an example ESS will reach up to 5 MW average power with up to 125 MW peak power. There is a clear difference between the instantaneous power and the stored beam energy and therefore these machine systems requires different machine protection approaches. Pulsed, high power machines, with a low repetition rate required a fast stop of the beams production. Storage rings with high stored beam energy requires that the beam energy is safely extracted and deposited on a beam dump block [2]. The work performed during this PhD is only focussed on the storage rings with high stored beam energy.

2.2 *CERN*

CERN (European Organization for Nuclear Research) is the largest particle accelerator facility in the world, hosting more than 11.000 visiting engineers and physicist and ~ 2250 staff employees. It is located in Geneva at the border between Switzerland and France. Founded in 1954, it has currently 22 member states, two international organizations (UNESCO, European Commission) and four countries with observer status (Japan, India, Russia and United States). In addition it also has co-operation agreements with 39 other countries in the world. Besides the high-energy accelerators it also hosts test facilities for future particle accelerators, like the Compact Linear Collider (CLIC) test facility [3] for a linear accelerator, an Advanced Wakefield Experiment (AWAKE) for plasma-wakefield acceleration [4]. Also de-accelerators were built at CERN to study the behavior of antiprotons [5]. In addition, experiments to study the properties of atomic nuclei, like Isotope mass Separator on-line facility (ISOLDE) [7], fixed target experiments, the Alpha Magnetic Spectrometer (AMS - located at the International Space Station) [6]. In addition, a theory department is located at CERN.

2.3 Accelerator Chain and LHC

The LHC is CERN's largest accelerator with a circumference of 26.659 km in the underground (average 100 m depth) of the Swiss-French border region near Geneva. It is installed in the tunnel of the former Large Electron-Positron Collider (LEP) [8]. A chain of smaller particle accelerators is used as pre-injectors to deliver beam to the LHC. This injector chain begins with a linear accelerator (LINAC 2), where the protons are bunched by an RFQ and afterwards accelerated with an Alvarez structure to an energy of 50 MeV. Followed by the Booster synchrotron, the first circular machine, consisting of 4 superimposed rings, accelerating the protons to 1.4 GeV. Afterwards the protons are injected into the Proton Synchrotron (PS) where the bunches are split and accelerated to 26 GeV. 288 bunches of the PS are injected into the Super Proton Synchrotron (SPS) and further accelerated to 450 GeV, the injection energy of the LHC [1]. An overview of the CERN accelerator complex is given in Figure 2.1 [9]. From the source the protons have to travel through LINAC 2, Booster, PS, SPS before they are injected clockwise and counter-clockwise into the collider LHC. Ions are delivered via LINAC3, Leir, PS, SPS to the LHC. CTF3 is used as a test stand for the future linear collider, CLIC. Neutrino production in CNGS was stopped in 2012. The so-called North-Area is used for fixed target experiments. nTOF is a facility, to measure the time of flight of neutrons. In the AD, the antiproton decelerator, the behavior of antiprotons is studied. The injector chain will be upgraded in the view of the so-called high luminosity LHC project.

The basic layout of the LHC is formed by eight arcs, hosting 23 so-called FODO cells, and eight straight sections, the so-called Interaction Regions (IRs) [1]. In these IRs the four major experiments are located. The beams collide inside the experimental areas at the Interaction Points (IPs), where the experiments ATLAS (IP1), ALICE (IP2), CMS (IP5) and LHCb (IP8) are placed. The two counter rotating beams are injected in IR2 and IR8 respectively and accelerated by superconducting 400 MHz radio frequency cavities, positioned in IR4, up to a maximum allowed particle momentum of 3.5 TeV (2011), 4 TeV (2012), 6.5 TeV (2015) and 7 TeV (nominal). After the acceleration the beams are squeezed to reduce the beam size and then they are brought into collision. Under normal conditions the beams can be stored for up to 14 hours. At the end of physics operation or in case of failures the beams are dumped by the beam dumping system into the beam dump block, installed in a distance of 900 m from IR6, at the end of the two beam dump lines. The LHC layout is schematically shown in Figure 2.2. The LHC is also capable to collide lead ions, but this thesis will focus only on protons, as measurements and simulations were done with these particles.

One of the main goals of the LHC was the discovery of the Higgs Boson (2012) and detailed study of its properties. Other LHC goals are finding insights of physics beyond the standard model, studying the quark-gluon plasma, CP symmetry violation, super symmetry and extra dimensions. The discovery potential of the LHC is directly connected to the center of mass energy at collision and to the number of

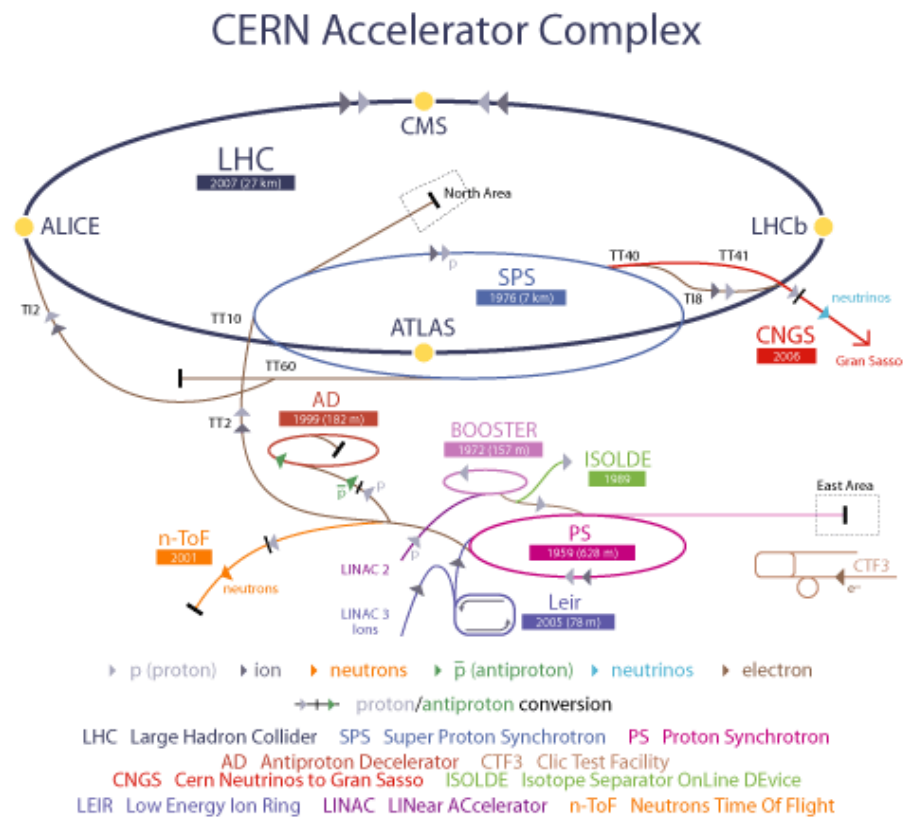


Fig. 2.1: CERN accelerator complex. From the source the protons have to travel through LINAC 2, Booster, PS, SPS before they are injected clockwise and counter-clockwise into the collider LHC. Ions are delivered via LINAC3, Leir, PS, SPS to the LHC.

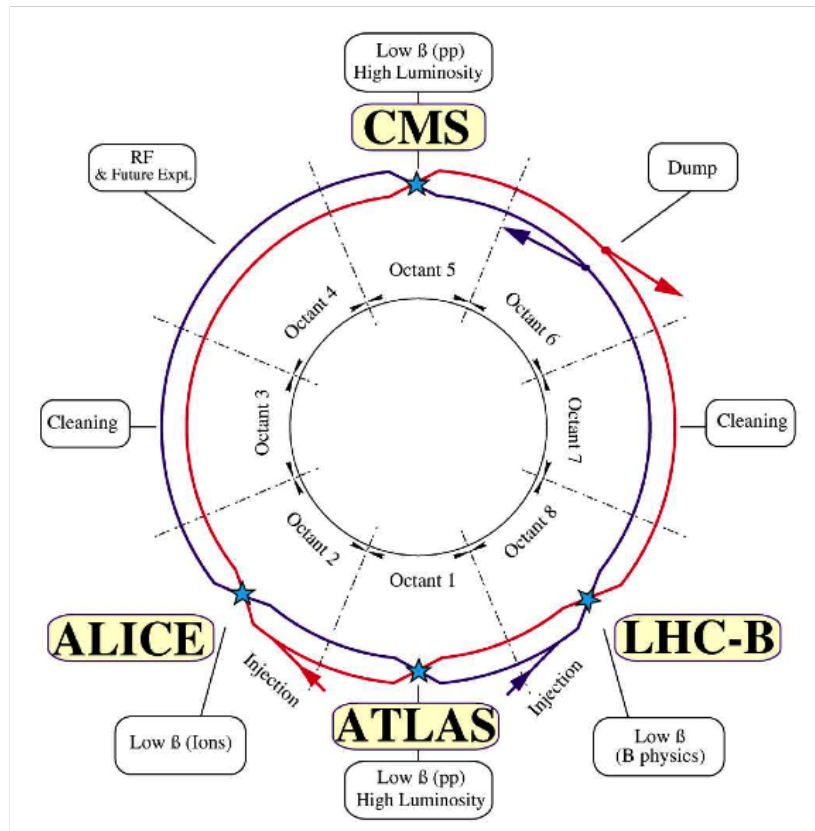


Fig. 2.2: LHC Layout: The LHC is segmented in 8 octants. The four experiments are located in IR1, IR2, IR5 and IR8, the beam is injected in IR2 and IR8. One beam dump per beam is installed at the end of the dump lines in IR6. The collimators are installed in IR3 and IR7.

collisions per unit time per area, the so-called luminosity L :

$$L = \frac{N_b^2 n_b f_{rev} \gamma}{4\pi \epsilon_n \beta_z^*} \cdot F, \quad (2.1)$$

with the number of particles per bunch N_b , the number of bunches per beam n_b , the revolution frequency f_{rev} , the relativistic gamma γ , the transverse normalized emittance ϵ_n and the value of the beta-function at the IP β_z^* . A geometric correction F is necessary to take into account the luminosity reduction induced by the fact that the beams do not collide head-on but under a crossing angle. The LHC design nominal luminosity is 10^{34} ($\text{cm}^{-2} \text{s}^{-1}$), which is two orders of magnitude higher than the peak luminosity at Tevatron, the former biggest collider in the world.

An overview of some of the LHC parameters is given in Table 2.1 [1]. Note, that the LHC just finished a two years long shutdown. Thus, 2015 is a year of (re-)start-up of the LHC

Tab. 2.1: Main beam parameters of the LHC for 2011, 2012, 2015 and nominal.

	2011	2012	2015	Nominal
Proton Energy (TeV)	3.5	4.0	6.5	7
Bunch Intensity #p	$\sim 1.5\text{E}11$	$\sim 1.5\text{E}11$	$\sim 1.2\text{E}11$	$\sim 1.15\text{E}11$
Number of Bunches	1380	1380	2740	2808
Bunch Spacing (ns)	50	50	25	25
Integrated Luminosity (fb^{-1})	5.7	23.7	10-15	50
Stored Beam Energy (MJ)	~ 116	~ 140	~ 330	~ 362

Only the use of superconducting magnets allows the creation of the required magnetic fields to bend and focus particles with such a high momentum as reached in the LHC. 1232 main dipoles (MB), 386 main quadrupoles (MQ) and more than 4000 corrector magnets are installed in the LHC tunnel. They mainly operate at temperatures of 1.9 K and 4.5 K. A picture of the 15 m long dipole magnets (also called bending magnets) installed in blue cryostats in the LHC tunnel can be seen in Figure 2.3.

The main bending magnets are made of cables with superconducting niobium-titanium filaments with a surrounding copper matrix. They reach a maximum magnetic field on beam axis of 8.3 T at currents of 12.84 kA in the coils. The main dipole magnets are used to keep the particles on their orbit around the machine. Quadrupole magnets are needed to focus the beams. In addition multipole magnets were installed to correct focussing errors (sextupoles) and higher multipole errors in the magnet system (octupoles, decapoles). These superconducting magnets are very sensitive to heat released by particle losses. When the energy deposition reaches a limit of 10 mJ/cm^3 the magnet will loose its superconductivity, this is called quench. In this case the stored energy of the magnet ($\sim 1.2 \text{ GJ}$ in one circuit of 154 dipole magnets) is dissipated as heat and the beams are dumped. In contrast to this, the stored beam energy per beam (362 MJ (nominal)) is sufficient to melt 500 kg of copper. The stored beam energy is a factor 200 higher than any other proton machine,

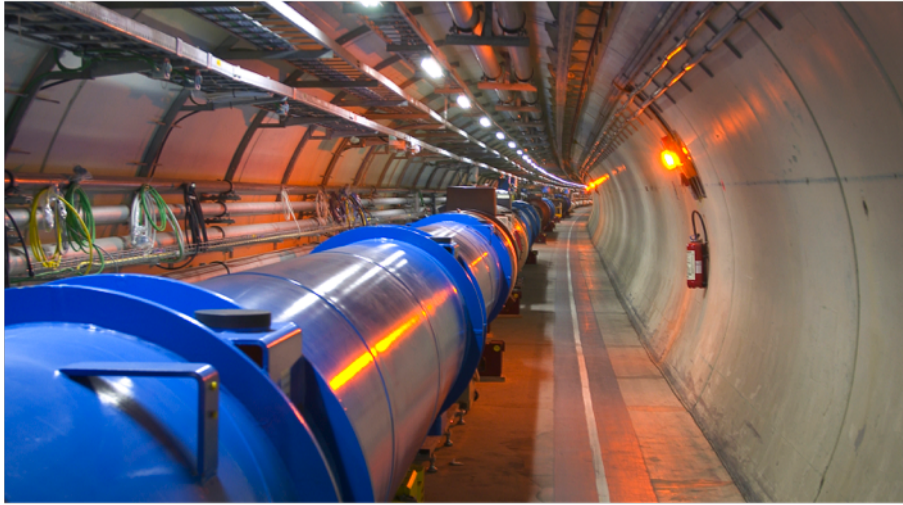


Fig. 2.3: LHC bending magnets in the blue cryostat installed in the LHC tunnel.

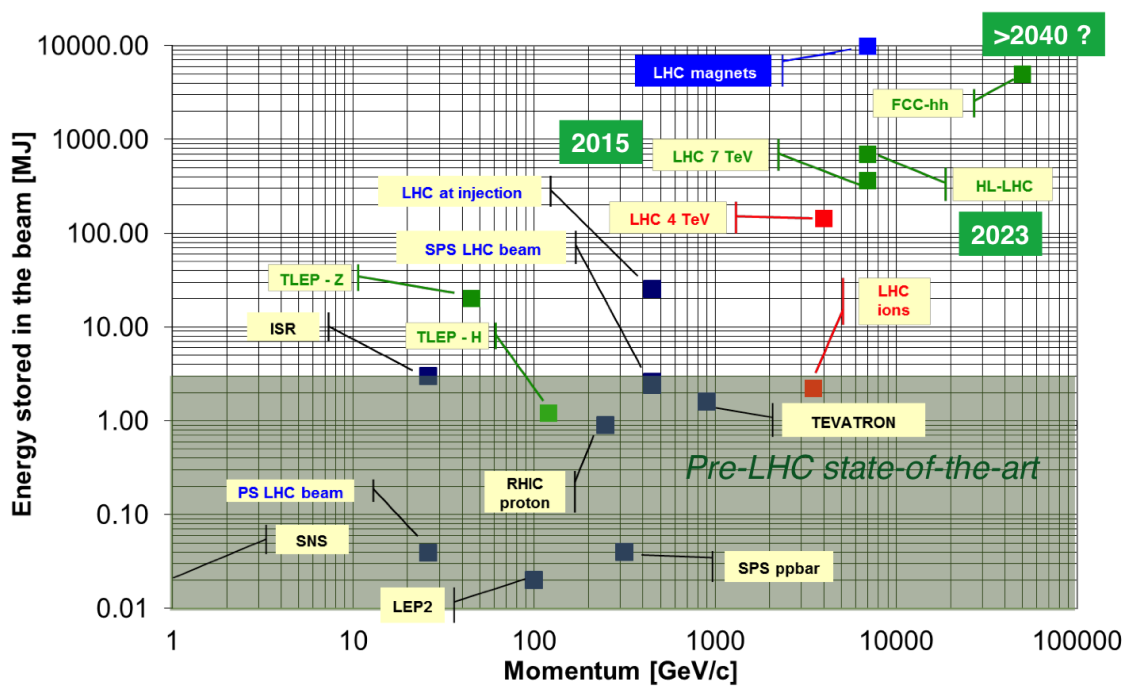


Fig. 2.4: Stored beam energy versus momentum for different accelerators. LHC values are marked in red. [2]

see Figure 2.4. These numbers explain the necessity of a reliable machine protection system.

The machine protection system needs a detection system to react in case of failures, therefore over 1000 of Beam Position Monitors (BPMs) are installed in the ring. Another important system is the Beam Loss Monitor (BLM) system to detect particle losses all around the ring. More than 3500 of these BLMs are installed in the LHC.

2.4 Future Hadron Accelerator

The European Strategy for Particle Physics started a design study for a potential high-energy frontier circular collider at CERN for the post-LHC era. Following the recommendation made in the 2013 update of the European Strategy for Particle Physics [10], [11], the so-called Future Circular Collider (FCC) will be studied. The FCC is a hadron collider with a centre-of-mass energy of 100 TeV. Assuming a nominal dipole field of 16 T, such an accelerator would have a circumference of 100 km. Figure 2.5 shows a schematic drawing of the possible location for the FCC in the Geneva area. The machine should accommodate two main experiments that are operated simultaneously and have a peak luminosity of up to $5 \times 10^{34} \text{ cm}^{-2} \text{ s}^{-1}$. The layout should also accommodate two additional special-purpose experiments to study the physics at the highest energies. The corresponding hadron injector chain is included in the study, taking into account the existing CERN accelerator infrastructure and long-term accelerator operation plans.

High-field superconducting magnets are a key technology for the FCC hadron collider. The 8 Tesla dipole magnets currently used in the LHC are current state-of-the-art. Shortening the collider ring to 80 km and keeping a particle energy of 50 TeV per beam would require fields in the range of 20 Tesla. Reaching such fields demands considerable research and development effort in superconducting magnet technology, like improvement of the LTS material Niobium-Tin (Nb3Sn) performance.

A table with the main beam parameters of the FCC hadron accelerator can be found in Table 2.2.

Tab. 2.2: Main parameters for FCC.

Beam momentum (TeV)	50
Bunch intensity #p	$\sim 1\text{E}11$
Number of bunches	10600
Beam size (mm)	0.2

The FCC aims using high-energy particle colliders to answer some of the most important questions in physics, like:

- What are the exact properties of the Higgs Boson?
- What are the fundamental laws that govern nature?



Fig. 2.5: Possible location of the FCC (dashed line). The present LHC is marked in blue. The lake geneva is on the top of the picture.

- What are the smallest constituents of matter?
- What is dark matter?
- Why is the origin of the matter-antimatter asymmetry in the universe?
- Why are neutrino masses so small, and do heavy partners of the neutrinos exist?
- Can the Standard Model be extended to accommodate a solution to these questions?
- Do particles have supersymmetric partners?
- Are there other forces in nature, which are too weak to have been observed so far?
- Can all known forces be unified? [11]

3. BEAM INTERACTION WITH MATERIAL

In this thesis the damage potential of high-energy particle beam will be described and discussed. To understand the beam matter interaction this chapter will give a short overview of the relevant processes. It will also describe the relevant material states and the so-called hydrodynamic tunneling process. In addition the simulation tools used within this thesis will be explained. A more detailed description of beam interaction with material can be found in literature [12], [13], [14] [15].

3.1 Particle - matter interaction

High energetic particles interact with matter in different ways. Charged particles, hadrons and leptons, interact almost entirely via ionization. Photons interact via various interaction processes with the atomic shells or the nuclei. This sub-chapter will briefly introduce the physics of the different types of interactions. The focus lies here on the interactions of high energetic protons with matter.

3.1.1 Cross section and mean free path

A particle traveling in a material will have a certain probability to interact with the target nuclei and electrons. In a thin target slice the probability for interaction is proportional to the thickness of the slice and the number of interaction partners per unit volume in the target. It is also influenced by the type of interaction, which is expressed by the so-called cross section σ [12]. For a single incident particle the cross section is correlated to the probability of a particle-matter interaction dP which is given by:

$$dP = N_t \cdot dx \cdot \sigma, \quad (3.1)$$

with the number of scattering centers N_t per unit volume and the thickness of the slice dx . The cross section itself has the dimensions of an area, cm^2 , or in particle physics: barn = 10^{-24}cm^2 . As a particle can interact in different ways, for example it can scatter elastically at a nucleus (kinetic energy preserved) or it can scatter and excite the nucleus (kinetic energy not preserved), the total cross-section is given by the sum of its particle cross-sections.

$$\sigma_{tot} = \sigma_{elastic} + \sigma_{inelastic} \quad (3.2)$$

The average distance λ before a particle's first collision can be expressed by integrating the probability density function $P(x)$:

$$\lambda = \int_0^{\infty} P(x)x dx = \int_0^{\infty} e^{-xN_t\sigma} N_t\sigma x dx = \frac{1}{N_t\sigma} \int_0^{\infty} e^{-x} x dx = \frac{1}{N_t\sigma} \quad (3.3)$$

with

$$P(x) = N_t\sigma e^{-xN_t\sigma} \quad (3.4)$$

This distance is called mean free path and describes the average distance between two interactions and gives a measure of the probability of a particle-target interaction.

3.1.2 Charged particle interactions

A charged particle traveling through a material can excite atoms or cause ionization by interacting with target electrons, depending on the amount of energy transferred. The electrons are kicked out of their shell and the material gets ionized. Through this process the high energetic particles lose a part of their energy. The average energy loss, also called stopping power, dE per unit length dx is described by the Bethe equation [16], [17], [18] :

$$-\frac{dE}{dx} = \frac{n_e z^2 e^4}{4\pi\epsilon_0^2 m_e \beta^2} \cdot \left[\ln \left(\frac{2m_e c^2 \beta^2}{E_b \cdot (1 - \beta^2)} \right) \beta^2 \right] \quad (3.5)$$

with the electron density n_e , the charge number of the ionizing particle z , the elementary charge e , the vacuum permittivity ϵ_0 , the mass of the electron m_e , the speed of light c , the mean excitation energy E_b and $\beta = \frac{v}{c}$, with the speed of the particle v . The stopping power has the unit $\text{MeV g}^{-1} \text{cm}^{-2}$.

The Bethe equation is incorrect for electrons as they get scattered significantly, which is not taken into account in the Bethe equation. For very low energies additional terms have to be included to take into account the non-participation of inner electrons in the collision process. These terms are called shell correction. In the case of a relativistic particle with speed close to speed of light ($\beta \approx 1$) dE/dx is minimal. A particle with these parameters is called Minimum Ionizing Particle (MIP) [12]. An overview of the mean energy loss for different elements and impacting particles is given in Figure 3.1.

Additional radiative effects lead to an energy loss for charged particles. The dominating effect for light charged particles like electrons, which get scattered and thereby receive a negative acceleration, is bremsstrahlung. This type of energy loss is dependent on the particle energy. Above a certain threshold, depending on target and particle type, this radiation loss becomes more important than the energy loss due to ionization. Taking into account radiation effects dE/dx can be expressed by:

$$\left(\frac{dE}{dx} \right)_{rad} = \frac{4n_a Z^2 \alpha^3 (\hbar c)^2 E_e}{m_e^2 c^4} \cdot \ln \left(\frac{a(E)}{Z^{1/3}} \right), \quad (3.6)$$

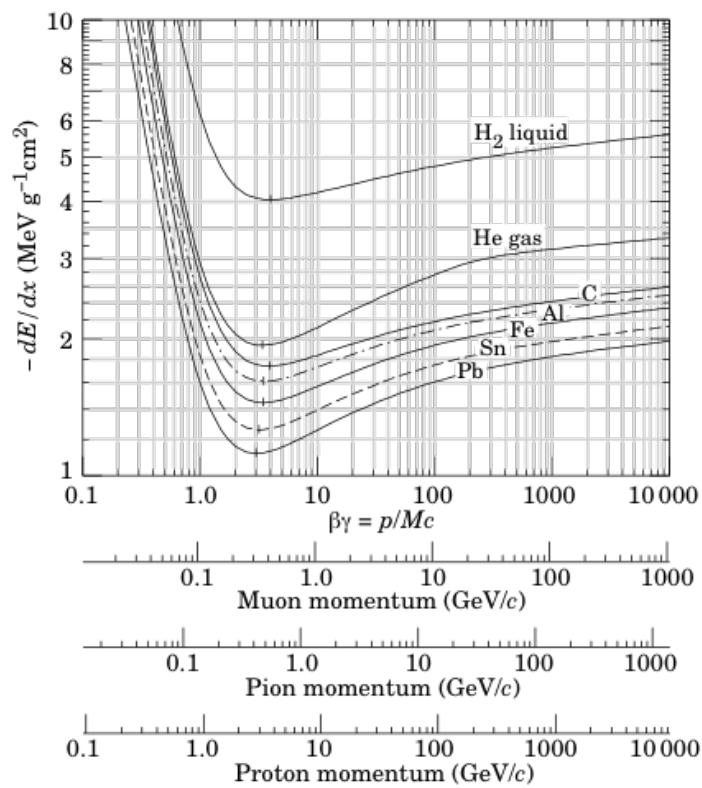


Fig. 3.1: Solutions of the Bethe equation for liquid hydrogen, gaseous helium, carbon, aluminum, iron, tin and lead as a function of the energy [14]. The range is given in $\text{MeV g}^{-1} \text{cm}^{-2}$.

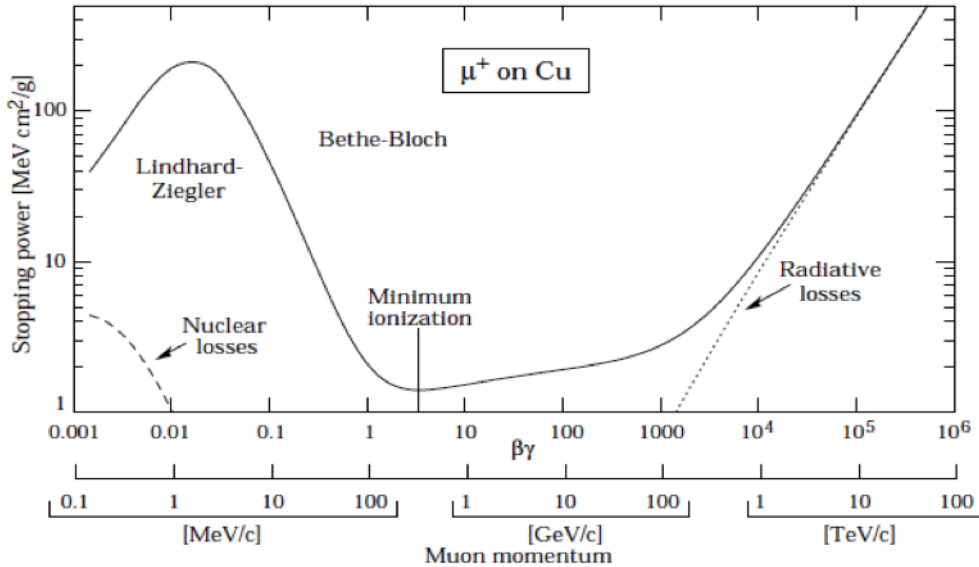


Fig. 3.2: Stopping power of Muons in Copper as a function of particle energy. The different contributions to the energy loss is shown, for the low energy region the energy loss is dominated by nuclear losses, the minimum of the Bethe-Bloch equation indicates the MIP, for higher energies radiative losses become more important, for energies above 1 TeV they dominate [14].

with the kinetic energy of the incident particle E_e , the atomic density of the material n_a , the charge of the target nuclei Z , the fine structure constant α , the Dirac constant \hbar , the speed of light c , and a numerical correction factor $a(E)$, which takes into account the impact parameters needed to produce radiative energy loss. An example for the stopping power of Muons in copper is given in Figure 3.2. Muons are a factor ~ 9 lighter than protons. It shows the different contributions to the energy loss, for the low energy region, which is dominated by nuclear losses. The minimum of the Bethe-Bloch equation indicates the MIP. For higher energies radiative losses become more important. Above 1 TeV the radiative losses are dominant [12].

3.1.3 Multiple coulomb scattering

Particles scattered in a material will change their direction. This deflection by a small angle is mostly due to Coulomb scattering at the nucleus. This kind of erratic changes in the direction of a particle is therefore called Multiple Coulomb Scattering or direction straggling [19]. In the case of hadrons, also the strong interaction contributes to this effect. For small deflections angles, the probability distribution of the angle is more or less Gaussian. The root mean square direction deviation of a particle passing through a slice of material with thickness L is given by:

$$\sqrt{\theta^2} = \frac{Z}{Pc\beta} \cdot (20 \text{ MeV}) \sqrt{\frac{L}{X_0}}, \quad (3.7)$$

with the scattering angle relative to the incoming particle in radians θ , the par-

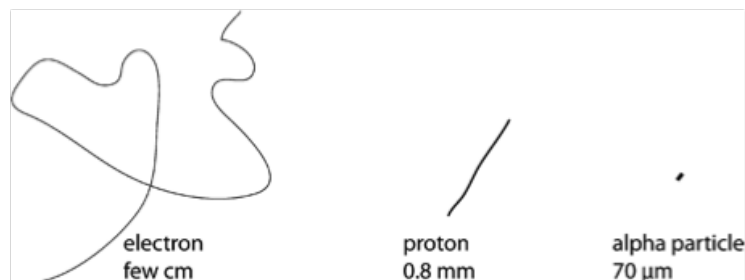


Fig. 3.3: Typical trajectory of a 10 MeV electron, proton and alpha particle in silicon. Note: the length of the drawn trajectories do not have the same scale [43].

ticle momentum P , the speed of light c , the relativistic β , the atomic number Z and the radiation length of the material X_0 . The radiation length defines the interaction between charged particles or gamma rays with material. It is the distance along which an electron has lost $1/e$ of its initial energy by Bremsstrahlung. X_0 depends on the density and the charge of the nucleus. An overview of the radiation length for different materials can be found in Table 3.1.

θ represents the angle in space of the scattering process, θ_p is the angle projected on the plane of the incoming particle. They are both related via:

$$\sqrt{\theta_p^2} = \frac{1}{\sqrt{2}} \sqrt{\theta^2} \quad (3.8)$$

Tab. 3.1: Radiation length for different materials [14].

Material	Radiation length (cm)
Air	304
Water	36
Aluminum	8.9
Concrete	11
Lead	0.56

Alpha particles and protons of a few MeV travel a small fraction of the radiation length, as they are stopped before they are scattered over a big angle. Electrons are strongly affected by multiple scattering, therefore the distance they travel on a straight line is usually much shorter than the actual length of the trajectory. A schematic of the typical trajectories of electrons, protons and alpha particles with an energy of 10 MeV in silicon can be found in Figure 3.3. Note: the length of the trajectories do not have the same scale.

At low energies, the energy loss of an electron is dominated by ionization, with contributions of Moller and Bhabha scattering and positron annihilation. At higher energies (> 10 MeV) the energy loss is dominated by Bremsstrahlung. An overview of the fractional loss per radiation length in lead as a function of electron or positron

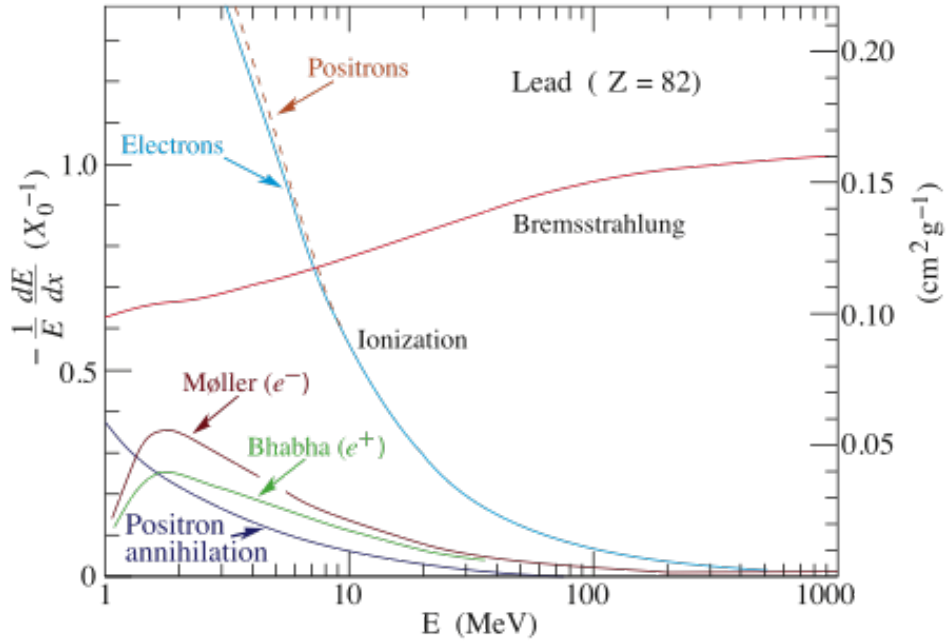


Fig. 3.4: Fractional energy loss per radiation length in lead as a function of electron or positron energy. The critical energy is 7.3 MeV [14].

energy is given in Figure 3.4. The energy at which the energy lost due to ionization and bremsstrahlung are equal is called critical energy, it can be approximated by:

$$E_c = \frac{610 \text{ MeV}}{(Z + 1.24)} \quad (3.9)$$

for solid materials.

Photons lose only a minor part of their energy due to direct energy deposition. The dominating interactions with matter are elastic scattering due to Rayleigh and Thompson scattering, inelastic scattering and absorption in the electron shell, absorption by a nucleus, the excitation of the nucleus and pair production, i.e. creation of pairs of electrons and positrons.

3.1.4 Electromagnetic showers

At high energies, an electron or positron will lose its energy mainly by emitting Bremsstrahlung, radiating a photon. High energy photons will lose their energy mainly due to pair production, which will afterwards radiate other photons [20]. This process will continue and will grow exponentially until the energy of the particle drops below the critical energy, when it will lose energy by ionization and excitation. A schematic drawing of an electromagnetic cascade can be found in Figure 3.5. About 90 % of the electromagnetic showers are maintained within the so-called Moliere radius, R_M [21]. The Moliere radius is a property of the target material. It is described as:

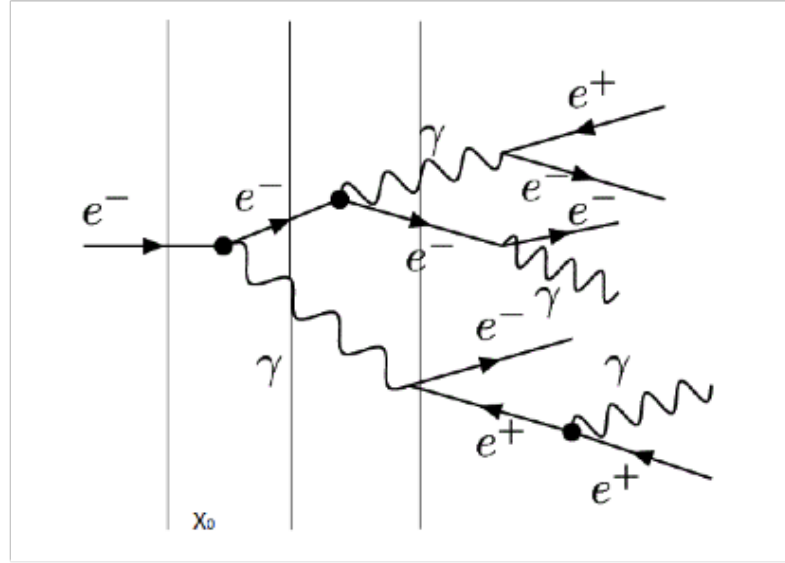


Fig. 3.5: Schematic drawing of an electromagnetic cascade. The primary electron radiates a photon due to Bremsstrahlung, this photon will then lose its energy due to pair production [85].

$$R_M = 0.026 \cdot X_0 \cdot (Z + 1.2). \quad (3.10)$$

The Moliere radius of solid copper is 1.67 cm.

3.1.5 Interactions with a nucleus

If a proton collides with a nucleus, it will transfer some of its energy to the nucleus and its direction will be changed or it will be bounced backwards. Protons are much lighter than most of the nuclei and the collision with a nucleus will cause little energy loss [12]. Using non-relativistic kinematics, energy and momentum conservation, the maximum energy transferred in an elastic collision of a proton with its mass m and speed v and the nucleus of mass M can be calculated by:

$$\Delta E_{max} = 0.5mv^2 \left(\frac{4mM}{(m + M)^2} \right). \quad (3.11)$$

If m is much smaller than the mass of the nucleus M equation 3.11 can be simplified to:

$$\Delta E_{max} = 0.5mv^2 \left(\frac{4m}{M} \right). \quad (3.12)$$

For extremely heavy nuclei the energy transfer within a proton-nucleus collision is very small, compared to a proton-electron collisions. As a result, the change of

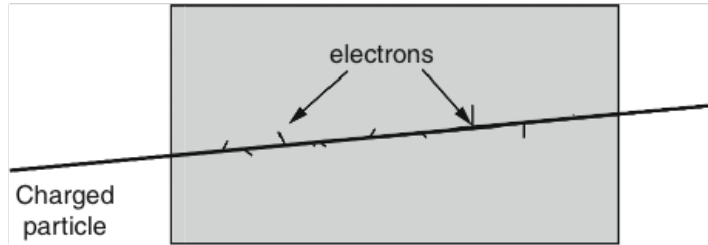


Fig. 3.6: Schematic drawing of a charged particle traveling in matter and leaving a trace of excited atoms (on the particle trajectory) and free electrons behind [43].

direction of the proton is small and most of the energy loss of the proton is due to the collisions with the shell-electrons. Nevertheless most of the change of direction is caused by the collisions with the nucleus.

A charged particle, traveling in matter will lead to a trace of excited atoms (on beam axis) and free electrons that have acquired energy in the collision. A schematic drawing of this process can be found in Figure 3.6.

Most of these electrons have only received a very small amount of energy but some of the electrons acquire sufficient energy to travel macroscopic distances in matter. These high-energy electrons are called δ -electrons. Some of them have sufficient energy themselves to excite or ionize atoms in the medium.

3.1.6 Hadronic showers

High energy protons can create a trace of secondary particles when they interact with the target material. These showers can interact with the target material and can create new secondary particles if they themselves have a sufficient energy [12]. If the particle energy exceeds the pion production threshold of 290 MeV, then the production of π_0 and η mesons will start to transfer energy from the hadronic shower to electromagnetic showers as they decay into e^\pm and γ particles. These particles themselves will start electromagnetic showering processes, as explained above. A schematic of the hadronic and electromagnetic showers behavior can be found in Figure 3.7.

The shower particles with the highest energy are concentrated around the beam axis. The energy deposition profile around the beam axis is dominated by the stopping power of the particles and the electromagnetic showers. The interaction of low energy neutrons (ex. recoils and photons) defines the energy deposition profiles at the radial tails.

Neutron interaction at moderate to low energies are dominating. The longitudinal shower development is defined by high energy shower particles, as they carry a big fraction of the energy. In addition, they have a long interaction length. The high energy cascade can be identified with the aid of pions as they can only be produced by shower particles [43].

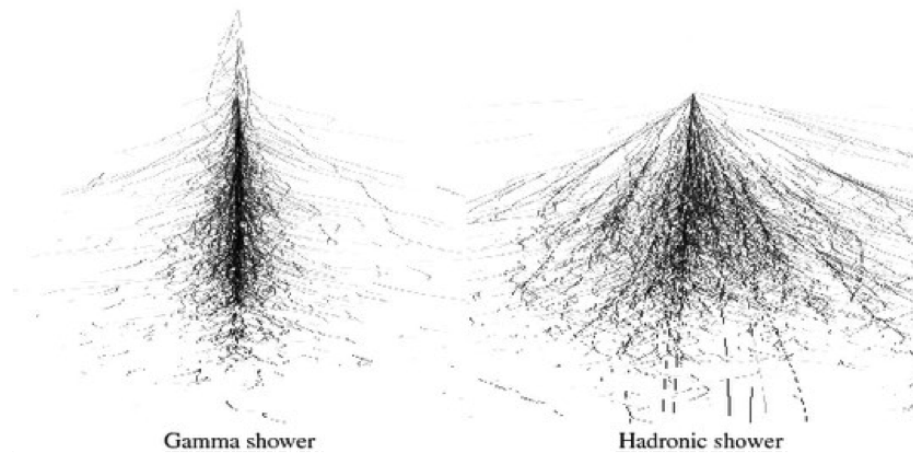


Fig. 3.7: Schematic of and electromagnetic (left) and hadronic showers (right) [86].

3.1.7 Nuclear spallation

Nuclear spallation processes occur by an interaction of a high energetic projectile (above 100 MeV) with a target atomic nucleus. For this process, high power accelerators are needed. Nuclear spallation can be described as a two-stage process. In the first stage, the projectile (neutron or proton) reacts with the neutrons and protons of the nucleus. The following reactions create an intra-nuclear cascade of high-energy (above 20 MeV) protons, neutrons, and pions within the nucleus. Some hadrons can escape as secondary particles, others deposit their kinetic energy in the nucleus leading to an excited state.

In the second stage (the so-called nuclear de-excitation), evaporation takes place when the excited nucleus relaxes by emitting low-energy (below 20 MeV) particles, mainly neutrons. These neutrons produced during nuclear de-excitation are important in a spallation source because they can be moderated to even lower energies for use as research probes.

Secondary high-energy particles produced during the intra-nuclear cascade can interact with other nuclei in the target, leading to a series of secondary spallation reactions that generate more secondary particles and low-energy neutrons. The so-called hadronic cascade is the accumulation of all reactions caused by primary and secondary particles in a target [22]. Spallation facilities are located for example in Lund, Sweden (European spallation source), at PSI, Switzerland (SINQ) and Oak Ridge, USA (Spallation neutron source). Spallation is also used for transmutation, for example at Myrrha, Mol, Belgium.

3.2 *Warme Dense Matter*

The matter humans can see is made of baryonic matter, where protons, electrons and neutrons form atoms. This includes stars, planets and humans. But this is only $\sim 4.9\%$ of the matter in the universe, the rest is made of dark matter ($\sim 26.8\%$) and dark energy ($\sim 68.3\%$). Dark matter does not interact with the electromagnetic

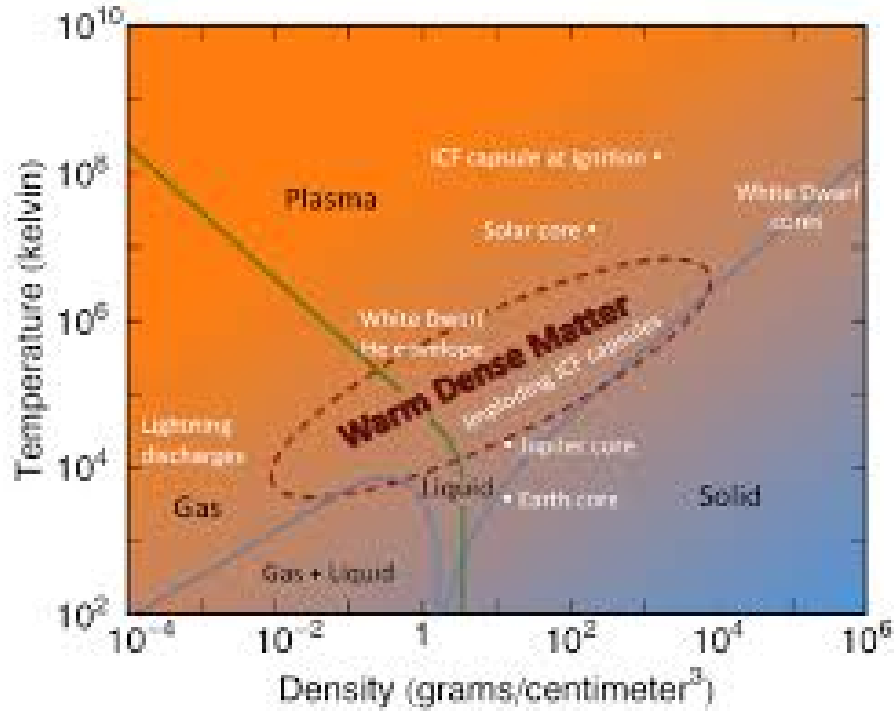


Fig. 3.8: Phase diagram as a function of temperature and density. The red dashed line indicates the region, where Warm Dense Matter applies. Courtesy: M. Desjarlais.

force. This means it does not absorb, reflect or emit light. The existence of dark matter can only be deduced from the gravitational effect it has on visible matter. The baryonic matter on earth is in solid, liquid or gaseous state, but $\sim 99\%$ of the visible matter in the universe is in a plasma state. Plasmas occur on earth as lightning, polar aurorae, the ionosphere and (artificially made) in plasma TV screens, fluorescent lamps, fusion energy research and during laser welding. So-called hot plasmas can be found in cores of stars, low density plasmas form the intergalactic medium. Warm dense matter (WDM) is a not clearly defined state of matter [87], [23]. WDM has a density comparable to a solid material (between 0.01 and 100 g/cm³) and a temperature of a few tens of thousands of kelvins (between 1 and 100 eV) with pressures in the order of Mbars. It is too dense to be described by plasma physics and it is too hot to be described by condensed matter physics. WDM is expected to appear in solids that are warmed up to plasmas. Cores of some large planets, like Jupiter and Saturn, might be made of WDM. To produce WDM in the lab dynamic methods like impact of high power lasers or ion beams on condensed targets are used. Therefore WDM can be studied in a reproducible way with particle accelerators, by fixed target experiments [24], [25], [26]. The region of the WDM in the temperature - density phase diagram is shown in Figure 3.8.

No relations between temperature, pressure and density have been formulated for this phase state, therefore the Equation of State (EOS) are based on empirical data. Using accelerators allows to improve the EOS. This will influence also astrophysics as well as plasma physics.

3.3 Hydrodynamic Tunneling

Previous theoretical work on beam target heating has shown that in case of a bunched particle beam, like the one stored in the LHC, the energy deposited in the target by the first few tens of proton bunches and their showers, cause strong heating of the solid material that leads to substantial increase in the temperature. The heated material undergoes phase transitions that include liquefaction, evaporation and even conversion into weakly ionized plasma and WDM. The high temperature in the absorption zone generates high pressures which launch a radially outgoing shock wave causing substantial density depletion along the axis. As a consequence, the protons that hit the target in the subsequent bunches, penetrate much deeper into the target. This phenomenon is called hydrodynamic tunneling. The continuation of this process during the irradiation, leads to a significant lengthening of the projectile range compared to an instantaneous energy deposition. This phenomenon therefore has very important implications on the machine protection system design. During this thesis the existence of hydrodynamic tunneling was proved and the simulation tools were benchmarked [27], [28], [29].

3.4 Simulation Tools

This section briefly describes the key simulation tools used during this thesis, FLUKA and BIG2. They were used for energy deposition studies, fluence and dose rate simulations (FLUKA) and for the study of hydrodynamic processes in an irradiated target (BIG2).

3.4.1 FLUKA

Energy deposition studies, fluence and dose rate studies were performed using the Monte-Carlo Code FLUKA [33], [34]. It is a general purpose tool for simulations of interactions with matter. It covers a wide range of applications from proton and electron accelerator shielding to target and detector design, from activation studies to dosimetry, cosmic ray studies and calorimetry. FLUKA is able to simulate interactions and secondary shower propagation in matter of about 60 different particles with high accuracy including photons and electrons (1 keV to thousands of TeV), neutrinos, muons of any energy, hadrons of energies up to 20 TeV (up to 10 PeV by using the DPMJET code) and all the corresponding antiparticles, neutrons down to thermal energies and heavy ions. The code can also handle polarized photons (e.g. synchrotron radiation) and optical photons. Complex geometries can be constructed by using Combinatorial Geometry (CG). It allows to track charged particles in magnetic and electric fields [35]. FLUKA includes 25 predefined single-element materials and several predefined compounds. New compounds can be built with their atoms, mass or volume fractions. The stopping power of charged particles is calculated from the Sternheimer parameters and the ionization potential. The FLUKA physical models have been described in several journal and conference papers.

3.4.2 *BIG2*

BIG2 is a 2D hydrodynamic computer code based on explicit Gudonov type scheme (flux through volumes is conserved) using curvilinear adaptive moving grids with second order accuracy in space [36]. The computational region can be divided into different sub-regions so that the code can also handle complicated multi-layered targets. The adaptive grid is generated inside every sub-region at every step in time. The code can deal with sharp gradients as well as with large target deformations. It also includes ion beam energy deposition and thermal conduction. The different phases of the target material are treated using a semi-empirical Equation-of-State (EOS) model [37]. Elastic-plastic effects are also included using the Prandtl-Reuss constitutive model [42].

4. FAILURE SCENARIOS FOR ACCELERATORS

This chapter describes the damage potential of a proton beam as a function of beam energy. This directly shows the need of a machine protection system, therefore machine protection systems of the LHC, including collimators and the LHC beam dumping system will be discussed. In the second part of this chapter the HiRadMat-Facility and the material damage experiments performed in this facility will be introduced. The last part is dedicated to beam loss instrumentation (diamond based particle detectors) to detect fast particle losses in case of fast failures. An introduction to the working principle of diamond particle detectors is given.

4.1 *Damage potential of proton beams*

With the request for more beam power at proton accelerators, the risk of beam induced damage is continuously increasing [44] [45]. At CERN, this is not limited to accelerators with large stored beam energy such as LHC, but also for lower energy machines in the injector chain some incidents have been observed. The interaction of protons with accelerator equipment may cause activation of material, quenches of superconducting magnets as well as damage, e.g. deformation or melting of material.

In this section the damage potential of proton beams as a function of particle momentum and beam size is discussed. The energy deposition of a proton beam with a momentum in a very large range from 50 MeV/c (typical momentum in the proton linac) and 40 TeV/c (minimum momentum suggested for FCC) is shown [50]. The effect of beam sizes between $\sigma = 0.1$ mm and $\sigma = 5$ mm is addressed. The damage potential for copper is calculated using the general purpose tool for calculations of particle transport and interactions with matter, FLUKA. Copper was chosen as material due to the fact that a lot of accelerator equipment is made of copper, like the coating of the beam screen and also the superconducting cables with their copper matrix surrounding the superconducting niob-titanium filaments. To define safe beam parameters additionally the number of particles needed to melt 1 mm³ copper was calculated.

For the simulations the following proton energies were studied: 50 MeV (linac extraction), 100 MeV, 200 MeV, 500 MeV, 600 MeV, 1 GeV (PSB), 26 GeV (PS), 50 GeV, 100 GeV, 200 GeV, 300 GeV, 450 GeV (SPS), 7 TeV (LHC) and 40 TeV (FCC). Five different beam sizes were considered: $\sigma = 0.1$ mm, 0.2 mm, 0.5 mm, 1 mm and 5 mm, to study the dependence on the energy deposition density. A Gaussian beam profile was chosen in both horizontal and vertical planes. The simulation target consists of a copper cylinder with a radius $R = 5$ cm and a length either $L = 25$ cm

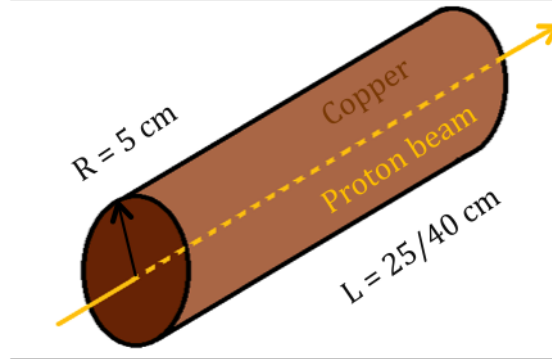


Fig. 4.1: Target for damage potential simulations. A length of 25 cm was used for particle energies below 450 GeV. The beam hits the target at $R = 0$ cm.

and 40 cm, for protons with an energy below and above 450 GeV, respectively. Two target lengths were chosen as for higher particle energies the maximum energy deposition will move deeper into the material, caused by shower particles, as described in chapter 3. For these simulations a instantaneous energy deposition was assumed. A schematics of the target can be found in Figure 4.1.

For the calculation of the numbers of protons needed to melt 1 mm^3 of copper a constant heat capacity C_p (mJ/K/cm^3) for small temperature increases was used. The amount of energy Q needed to increase the temperature of a unit of copper from $T_0 = 300 \text{ K}$ to the melting point $T_{melt} = 1360 \text{ K}$ is calculated using the following equation [46]:

$$Q = \sum_{i=T_0}^{T_{melt}} C_{p_i}(T) \cdot \Delta T_i \quad (4.1)$$

with the start temperature T_0 and the corresponding C_{p_i} for the given small temperature increase T_i . The corresponding number of protons N is found through the relation:

$$N_{300K-1360K} = \frac{Q}{E_{dep,FLUKA}} \quad (4.2)$$

with the energy deposition $E_{dep,FLUKA}$, calculated by FLUKA. To calculate the additional number of protons $N_{melting}$ needed for melting copper, the latent heat of copper $L = 176 \text{ J/g}$ and the density of copper $\rho = 8.96 \text{ g/cm}^3$ were taken into account [46].

$$N_{melting} = \frac{L \cdot \rho}{E_{dep,FLUKA}} \quad (4.3)$$

The total number of protons $N_{critical}$ can be found as:

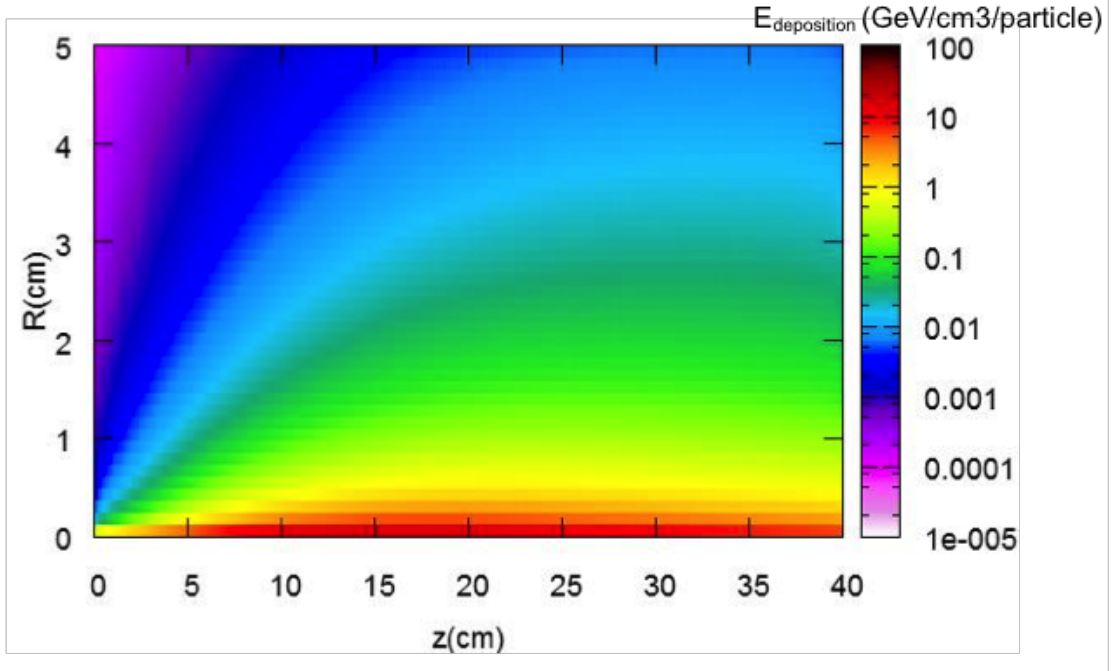


Fig. 4.2: 2D map of the energy deposition of a 450 GeV proton beam in the copper target along the beam axis. The beam with a $\sigma = 0.2$ mm is impacting on the left side at $R = 0$ cm.

$$N_{critical} = N_{300K-1360K} + N_{melting}. \quad (4.4)$$

Figure 4.2 shows as an example of the 2D energy deposition map of a 450 GeV proton beam with $\sigma = 0.2$ mm in the copper target. Most of the energy is deposited in a narrow volume along the beam axis and a fast decay of the dose with the radius is observed. This effect is shown in Figure 4.3 for four different energies. The radial bin size of 1.2 mm is clearly visible in the plot.

Figure 4.4 shows an overview of the energy deposition for the projectile energy range from 50 MeV to 40 TeV at a beam size of $\sigma = 0.2$ mm. At energies up to 100 MeV the interaction of the beam particles with the electrons of the target makes most of the energy being deposited in a small region called Bragg peak (see Figure 4.5). Above 600 MeV, the dose delivered by secondary projectiles is higher than the energy deposition from the primary beam, see Figure 4.6. The Bragg peak is covered by the losses from the secondary particles. Therefore, the Bragg peak cannot be seen in the figure. Both behaviors overlap in the region from 200 MeV to 600 MeV. The energy density gets smaller as the beam size increases, which leads to a reduction of the maximum energy deposition. At 50 MeV, the maximum energy deposition value is 2 times higher for $\sigma = 0.1$ than for $\sigma = 1$ mm. In the case of 450 GeV, the difference is a factor 1.6 for these beam sizes.

$N_{critical}$ was calculated for a volume at the surface and at the maximum energy deposition along the beam axis as a function of energy and beam size. The two volumes are schematically shown as an example at the energy deposition curve for

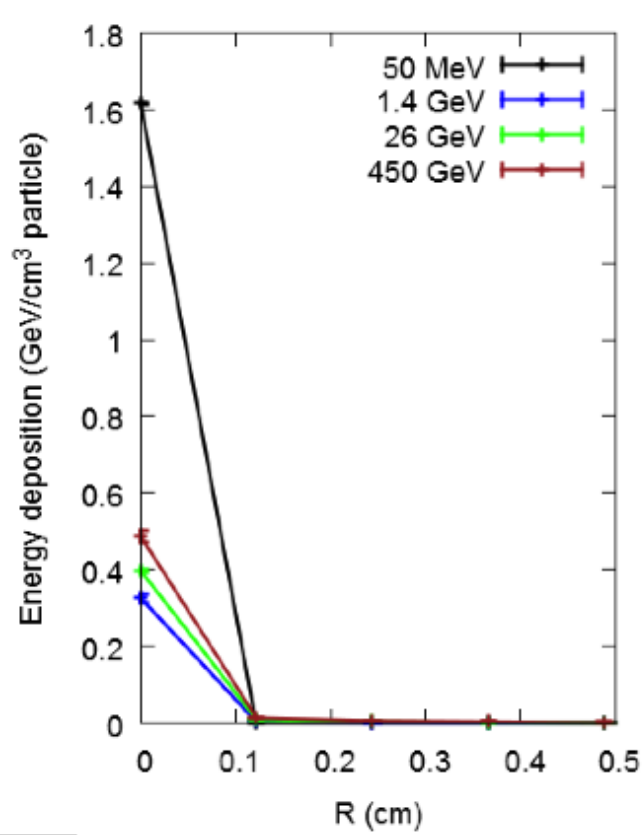


Fig. 4.3: Radial energy deposition per proton in GeV cm^{-3} for a beam sigma of 0.2 mm. A bin size of 1.2 mm in radial direction was used.

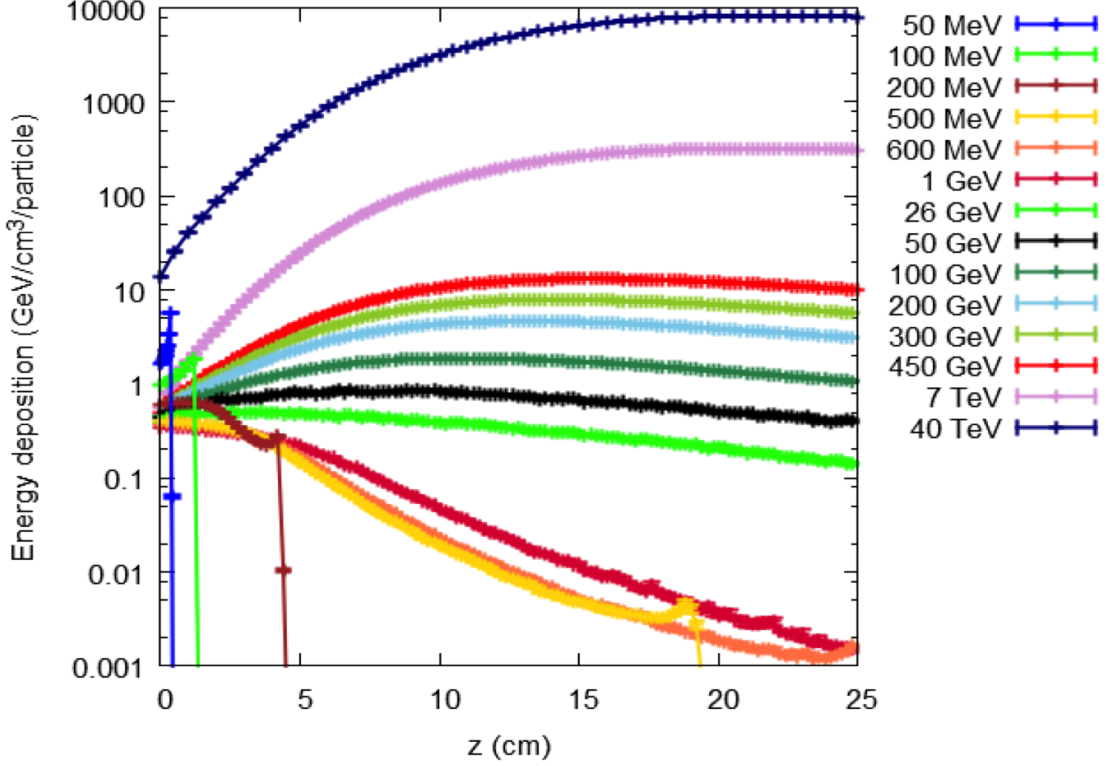


Fig. 4.4: Energy deposition overview in the range between 50 MeV and 40 TeV along beam axis and $\sigma = 0.2$ mm. The energy deposition is shown per proton in GeV cm^{-3} . At energies up to 100 MeV the interaction of the beam particles with the electrons of the target makes most of the energy being deposited at the Bragg peak. Above 600 MeV, the dose delivered by secondary projectiles is higher than the energy deposition from the primary beam. The Bragg peak is therefore covered by the losses from the secondary particles. Both behaviors overlap in the region from 200 MeV to 600 MeV.

450 GeV in Figure 4.7. $N_{critical}$ represents a threshold for damaging copper. At the LHC, where superconductive magnets are installed, 285% of the nominal bunch intensity at 450 GeV and 13% at 7 TeV is needed to melt the material in case of orthogonal impact and a beam with $\sigma = 0.2$ mm.

Table 4.1 summarizes $N_{critical}$ for Booster, PS, SPS and LHC injection and extraction energies and two different beam sizes: $\sigma = 0.2$ mm and $\sigma = 5$ mm.

Booster, PS and SPS are normal conducting accelerators (i.e. magnets at ~ 300 K) and LHC is a superconducting machine with most magnets operating at 1.9 K. Therefore the required energy to increase the temperature of the superconducting magnets from 1.9 K up to the melting point was taken into account. Despite the large difference between the surface and the maximum energy deposition values at 50 MeV, the damage potential is only 1.6 times higher in the Bragg peak, for $\sigma = 0.2$ mm. This is due to the fact that most of the energy is deposited in this small region. At 7 TeV, the number of protons needed to damage is 580 times less at the maximum than at the surface. The obtained results for 450 GeV (Table 4.1) agree with experiments

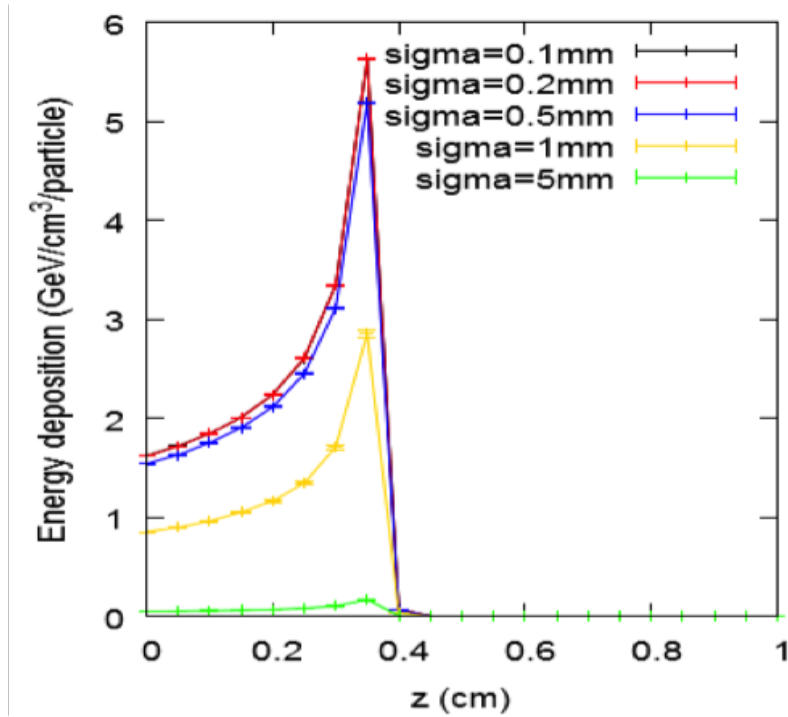


Fig. 4.5: Energy deposition for a proton beam at 50 MeV. 5 different beam sizes are shown. The Bragg peak is clearly visible and is located at 0.35 cm. The height of the Bragg peak depends on the beam size and therefore the energy density.

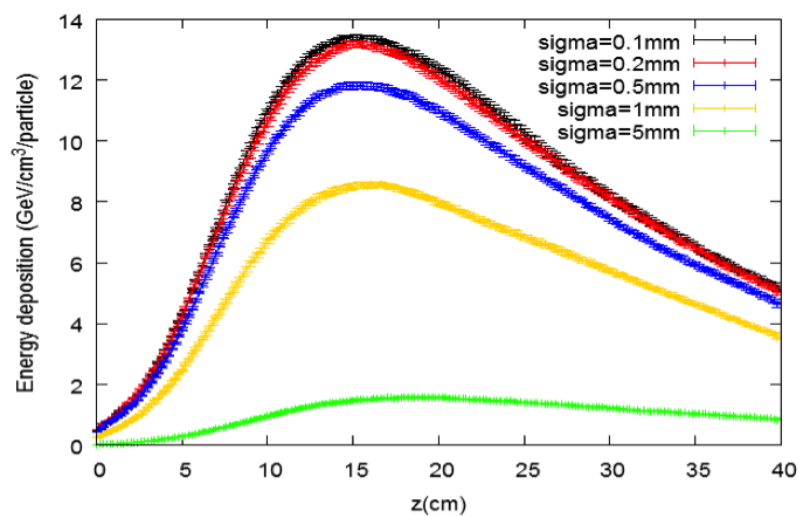


Fig. 4.6: Energy deposition for a proton beam of 450 GeV along beam axis for 5 different beam sizes. The peak energy deposition can be found at ~ 15.5 cm.

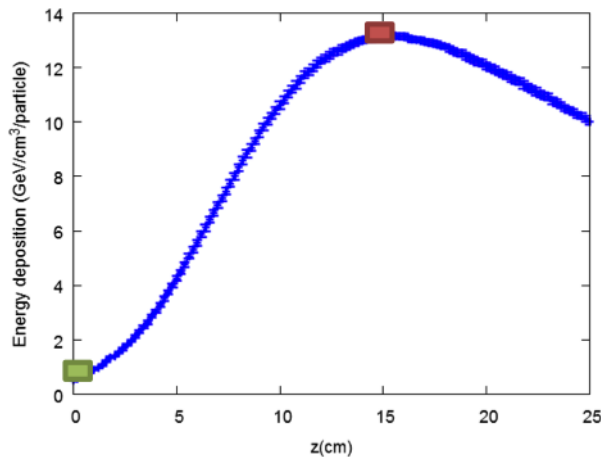


Fig. 4.7: Volumes at the surface (green) and the maximum energy deposition (red) along beam axis used to calculate the number of protons needed to melt 1 mm^3 of copper. The corresponding calculated number of protons can be found in Table 4.1.

performed for testing the damage induced by a proton beam extracted from SPS. As no damage was observed at intensities below 10^{12} protons. Note: a bigger beam size was used during these experiments [47], [48], [49]. The number of protons obtained for $\sigma = 0.2 \text{ mm}$ at 450 GeV at the maximum is slightly lower which, taking into account the beam size, is consistent with the experimental result [47]. The threshold for 7 TeV was calculated at 10^{10} protons, which is in very good agreement with the results obtained in the present study.

4.2 Machine Protection for LHC

This section will describe the LHC machine protection system. Due to the complexity of the system only the relevant parts needed for this thesis are described. To understand the different failure cases during LHC operation, this section will start with a short overview of the standard LHC operational cycle. It will explain the procedure to properly clean and dump the particle beams. In addition, this section will give a short introduction of the LHC Beam Interlock System (BIS).

4.2.1 LHC - cycle

At the beginning of a fill a so-called pilot bunch ($\sim 10^{10}$ protons) is injected into the LHC ring to guarantee the correct functioning of the magnet system. Only after this pilot bunch is circulating, the high intensity physics bunches (1.15×10^{11} p per bunch) can be injected. These physics bunches are normally injected in so-called trains. In 2012 the trains consisted usually of 288 bunches. With 50 ns bunch spacing a maximum number of 1380 bunches per beam was stored (nominal: 25 ns bunch spacing, 2808 bunches). The two beams are injected from the CERN Super Proton Synchrotron (SPS) with a particle momentum of 450 GeV. After filling, the beams are ramped up to the final particle momentum (2012: 4 TeV, 2015: 6.5 TeV,

Tab. 4.1: Number of Protons needed to damage and melt copper made accelerator equipment. The calculated energies are the extraction energies of the different accelerators at CERN. For 450 GeV and 7 TeV the additional energy deposition needed to increase the temperature from 1.9 K to room temperature is taken into account.

E (GeV)	σ (mm)	$N_{critical}$ (protons)	
		Surface	Maximum
0.05	0.2	2.1E12	1.3E12
	5	7.5E13	4.5E13
1.4	0.2	1.1E13	1.1E13
	5	3.1E13	3.1E13
26	0.2	9.6E12	7.4E12
	5	2.8E14	9.4E13
450	0.2	7.9E12	2.9E11
	5	2.5E14	2.6E12
450 sc magnets	0.2	8.9E12	3.3E11
	5	2.8E14	2.9E12
7000 sc magnets	0.2	8.4E12	1.4E10

nominal: 7 TeV). Thereby the current in the main dipole magnets is increased. The particles are accelerated with the help of 8 superconducting cavities installed in both beams. These cavities operate with an accelerating gradient of 5.5 MV/m and at a frequency of 400 MHz [1]. During the ramp the parameters of the different systems (e.g. magnet current, collimator positions, etc.) are automatically driven by time dependent functions. At top energy the beams are then squeezed to arrive at the appropriate beta-function before they are brought into collision in the experimental IPs. The operational mode when the beams collide is called “*stablebeams*”. After up to 17 hours of stable beams and luminosity production the beams are dumped, the magnets are ramped down, all systems are put to injection settings and a new fill can start [76].

4.2.2 LHC Beam Dump System

Each LHC beam stores an energy of 362 MJ, with beam sizes down to $\sigma = 0.2$ mm. The damage potential of this beam requires a dedicated system for the beam extraction. This extraction system is used to safely fast-extract the beam and to transport it to an external absorber, the so-called dump block TDE. This system is located at IR6 of the LHC. The TDE is placed at the end of a ~ 800 m long tunnel in order to allow a beam dilution to avoid an overheating of the absorber material [88].

The underground tunnels and caverns at IR6 and the two beam dump lines (red) are shown in Figure 4.8. The LHC beam dumping system LBDS is shown schematically in Figure 4.9 and comprises, for each ring [88]:

- 15 extraction kicker magnets MKD located in the LHC ring to kick the beam horizontally out of his circulating orbit into the high-field gap of the MSD sep-

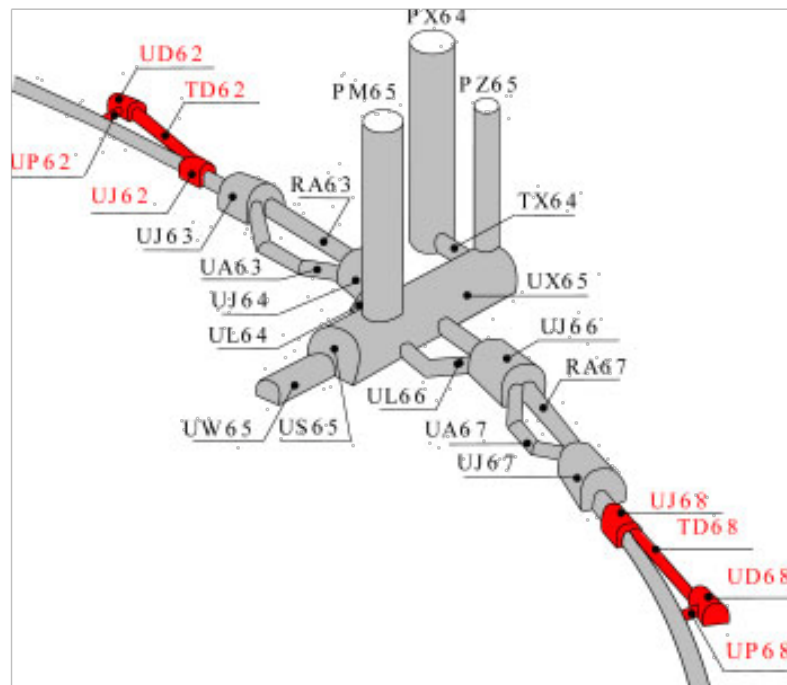


Fig. 4.8: Underground tunnels and caverns at IR6 of the LHC. The beam dump lines are marked in red [89].

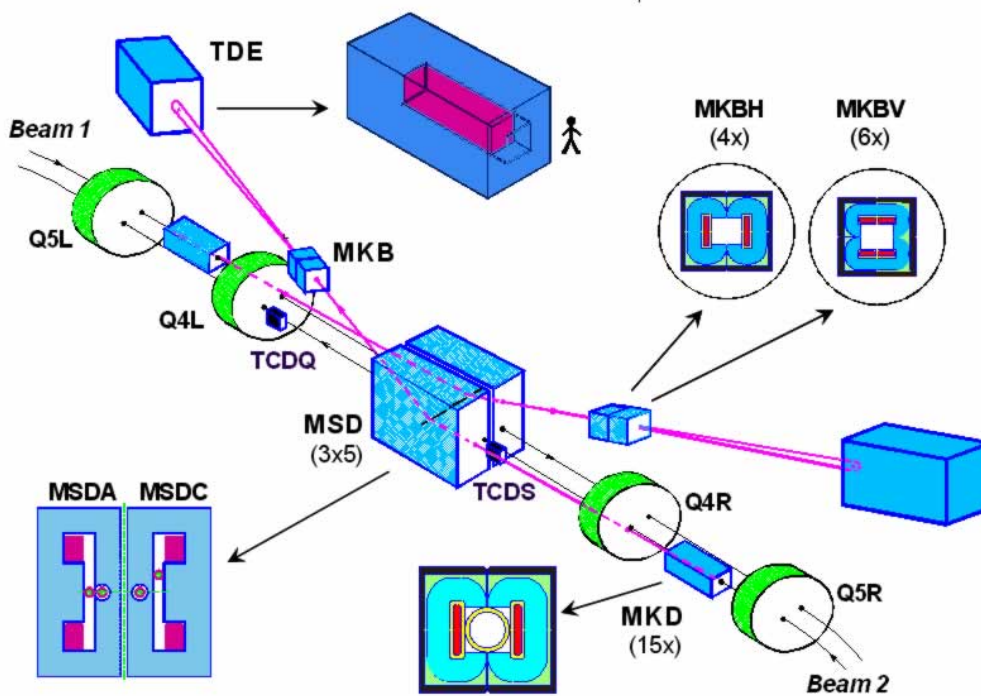


Fig. 4.9: The key magnetic elements of the LBDS. The kicker magnet (MKD) deflects the beam horizontally into the septum magnet (MSD). The beam dump line hosts the dilution kickers (MKD) and the beam dump block (TDE). In addition the drawing shows the protection elements (TCDQ and TCDS) and the last two sc LHC quadrupole magnets per beam (Q4R, Q5R and Q4L, Q5L) [89].

tum. The beam energy tracking system BETS will ensure the correct deflection strength of the MKD kicker magnets for the respective particle energies;

- 15 steel septum magnets MSD to provide a vertical deflection to raise the beam above the LHC machine cryostat before the start of the arc sections;
- 10 modules of dilution kicker magnets, MKB, to sweep the beam in an e - shaped form, with this method the beam is distributed over a surface of $\sim 35 \times 35 \text{ cm}^2$;
- The beam dump comprising the TDE core assembly and associated steel and concrete shielding, situated in the beam dump cavern;
- The TCDS and TCDQ absorbers in the LHC ring to avoid local damage to components in case of fault scenarios.

LHC beams are always extracted by the LBDS system either by a normal end of fill dump or because of a detected failure. The beam extraction trigger signal comes from the Beam Interlock System (BIS) which will be discussed in the following. To achieve a loss-free extraction a particle-free gap in the circulating beam is necessary. During this $3 \mu\text{s}$ long gap the field of the extraction kicker magnets has to rise to its nominal value according to the beam energy at the moment of dumping. This is the so-called abort-gap. After a beam extraction request from the BIS, the LBDS system waits until the abort gap is synchronized with the powering up of the extraction kickers. In case the MKD field rises, when particles are present, the particles will be swept with wrong angles. This failure case is called asynchronous beam dump. These miskicked particles should be absorbed by the TCDQ to protect the superconducting aperture further downstream and the TCDS to protect the septum. Beam profile (BTV) and position (BPM) monitors are placed in the dump line around the extraction septa, after the dilution kickers and in front of the dump block to monitor the particle trajectory along the beam dump line [88]. A screenshot of the so-called BTVDD in front of the TDE is shown in Figure 4.10. A beam dump with 22 bunches is shown.

Each beam dump core was designed as a segmented carbon cylinder of 70 cm diameter and 7.7 m length, shrink-fitted in a stainless steel, water cooled jacket. This inner core is then shielded by ~ 900 tons of iron and concrete blocks. In the case of a nominal LHC beam dump, the temperature in the carbon reaches max. 1250 K. Due to the high destructive power of the LHC beams, the LHC dumping system must have an extremely high reliability criteria.

4.2.3 Collimators

To deliver the nominal design luminosity it is necessary to store beams of up to 362 MJ in the superconducting ring of the LHC. The loss of only a fraction of 10^{-3} of the beam at top energy over 10 seconds can cause a quench in the superconducting magnet system. This requires a highly efficient performance ($> 99.999\%$) of the LHC collimation system to intercept and safely absorb losses and protect the LHC

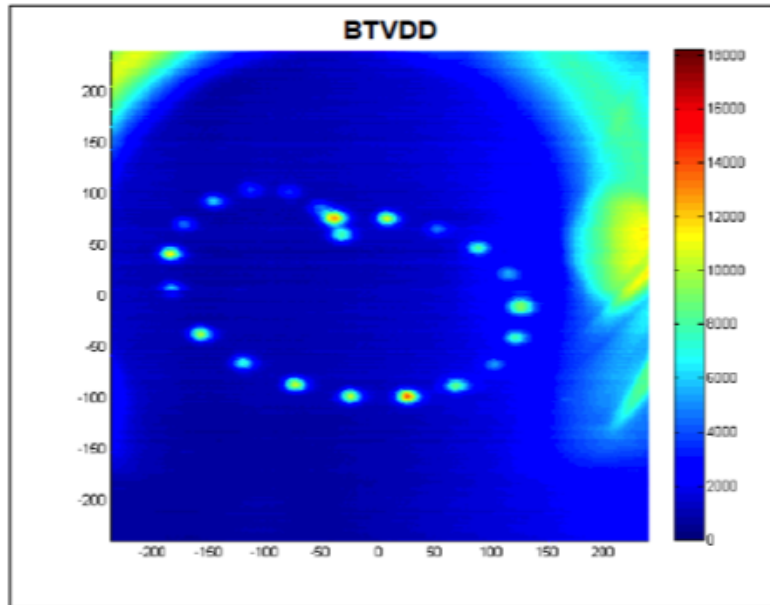


Fig. 4.10: Screenshot of the BTV in front of the beam dump block. The units in this picture are mm. The beam of 22 bunches is diluted in an e-shaped form, this is done by the dilution kicker magnets (MKB).

from avoidable quenches [77]. In addition, the collimation system has to protect all other accelerator equipment and the experimental detectors. The major parts of the collimation system are placed in the long straight sections of IR3 and IR7. IR3 is dedicated to so-called momentum (particles with the wrong momentum) and IR7 to betatron (particles with wrong beta-function) cleaning. In addition, several protection devices are installed in the LHC ring. The settings for various types of collimators depend on their function [81].

The collimation system consists of 108 movable collimators in horizontal, vertical and skew plane, installed in the ring and in the transfer lines to the LHC. It is a four-stage system. The main devices are primary (TCP), secondary (TCSG) and tertiary (TCT) collimators. 5 Absorbers (TCLA), collimators in the injection regions (TCLI and TDI) and in the extraction regions (TCDQA) complement the collimation system in the LHC. The TCTs are installed upstream of the experimental IRs to protect the triplet magnets, which perform a strong focussing of the particle beams into the IPs. Special absorbers are placed downstream of the IPs to collect the debris from physics operation. An overview of all collimators in the LHC is given in Figure 4.13 [78], [79].

To deliver the high efficiency, the gap opening of the collimators has to be small (tightest collimators have a gap opening of ~ 2.3 mm), but in addition, the collimator should not intercept the core of the beam and increase the impedance by putting materials too close to the beam. The losses should mainly be intercepted by the primary collimators, which are supposed to be the aperture bottleneck of the LHC. In the concept of a collimator hierarchy the primary collimators have to stay closest to the beam, followed by secondary collimators. With a small retraction be-

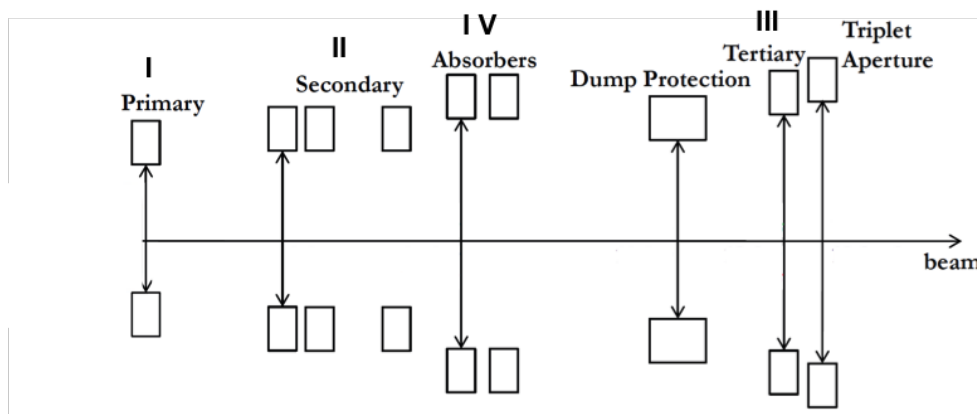


Fig. 4.11: Principal sketch of the four-stage cleaning system. The TCPs closest to the beam followed by the TCSGs and absorbers and the TCTs in front of the experimental triplet magnets.

tween secondary and primary collimators this makes tight tolerances and excellent movement control (step sizes of $\sim 5 \mu\text{m}$) necessary [80]. A sketch of the collimator hierarchy is shown in Figure 4.11.

In the LHC a collimator is made of two movable jaws. To find a good compromise between particle absorption, robustness and impedance, carbon-reinforced material was used for the primary and secondary collimators, which require the highest robustness. The tertiary collimators and the absorbers are made of tungsten jaws, because they have to absorb the tertiary halo and the particle showers from the primary and secondary collimators. The jaws are water cooled to conduct the heat load of impacting protons. The jaws have an active, flat part, a tapering and RF-fingers, which provide contact for the radio-frequency fields and currents between collimator and vacuum flanges, at both ends [82], [83]. A picture of an open collimator tank can be found in Figure 4.12.

The requirements for the collimator jaws are defined as such:

- The collimators jaws have to withstand beam impacts of up to 500 kW deposited energy.
- The surface of a jaw must remain flat on the 10-25 μm level.
- The choice of materials must be acceptable regarding impedance [82].

During run 1 the LHC collimation system was working with $\sim 99.99\%$ efficiency and no beam induced magnet quenches were observed during operation at 3.5 and 4 TeV.

4.2.4 Failure cases

In accelerators particles are distributed in a beam core and the surrounding beam halo. The size of the beam halo is limited by the aperture. The stable trajectory

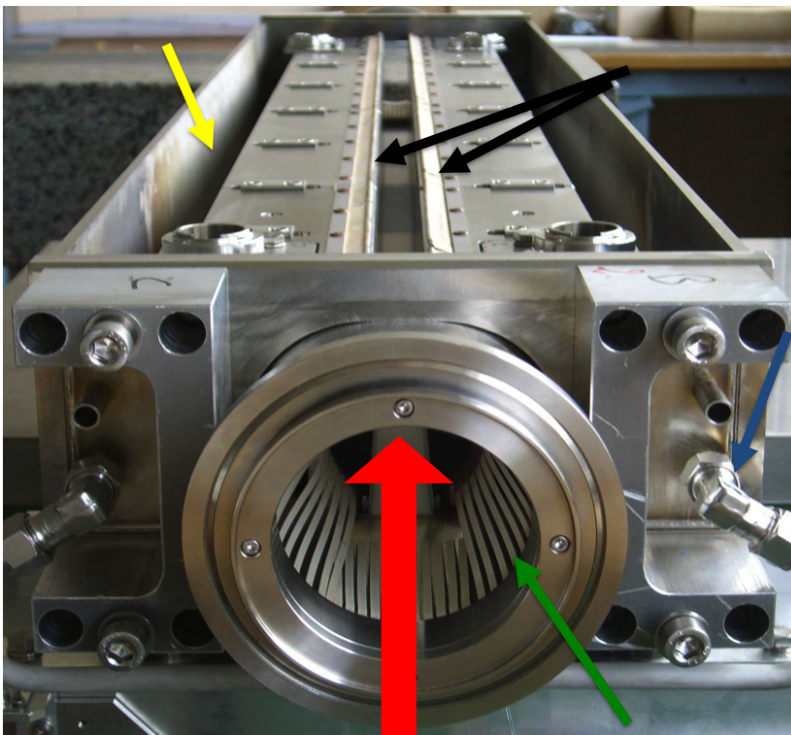


Fig. 4.12: Picture of the 1.2 m long TCSG collimator. One can see the beam direction (red arrow), the connection to the water cooling (blue arrow), the RF-fingers (green arrow), the two jaws (black arrows) who are mounted in the vacuum tank (yellow arrow).

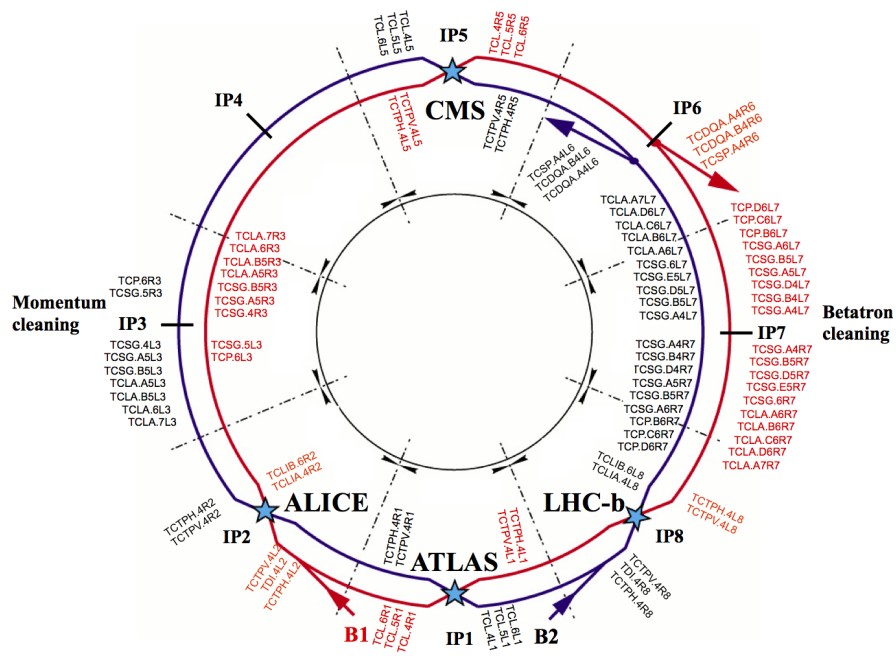


Fig. 4.13: All collimators installed in the LHC. In total 108 movable collimators are installed around LHC and in the transfer lines to LHC. Courtesy: B. Salvachua.

where a particle can perform a large number of turns is limited by the dynamic aperture, the stable region of phase space in a circular accelerator. Particles outside of the dynamic aperture get lost. In the LHC they should get lost at the collimators. A particle can be kicked out of the dynamic aperture for various reasons, for example due to diffusion. These processes create the beam halo and are called regular losses. Regular losses are unavoidable and make the collimation system necessary to minimize their effect on the accelerator equipment. The reasons which induce these regular losses are listed in the following:

- Intra Beam Scattering (IBS),
- Interaction with residual gas molecules,
- Emittance growth through coulomb scattering,
- Synchrotron radiation,
- Beam-beam effects. [76]

So-called irregular losses will be caused in case of failures [80], [81]. As this thesis is focussed on irregular ultra-fast losses, failures should be grouped according to their time structure [91].

- Ultra- fast losses occur in less than four LHC revolution turns,
- Fast losses occur in between $356 \mu\text{s}$ and 10 ms,
- Intermediate losses occur in between 10 ms and 10 s,
- Slow losses occur 10 s to 100 s.

Ultra-fast losses can cause high losses on the timescale of a couple of LHC turns ($\sim 100 \mu\text{s}$). Examples for these are:

- Injection errors,
- Failure of kicker magnets,
- Failure of RF system,
- Failures in the powering of the nc magnets.

Ultra-fast losses can only be absorbed by passive protection devices like collimators, absorbers and fixed masks [91] as active protection systems have reaction times higher than the time scale of the loss. Ultra-fast losses are dangerous because of the high damage potential of the LHC beam. Another ultra-fast and fast loss is the so-called UFO event, when a dust particle is falling through the beam [90]. Due to this interaction very high losses can be created within several LHC turns. An overview of the different failures and their surveillance elements is shown in Figure 4.14.

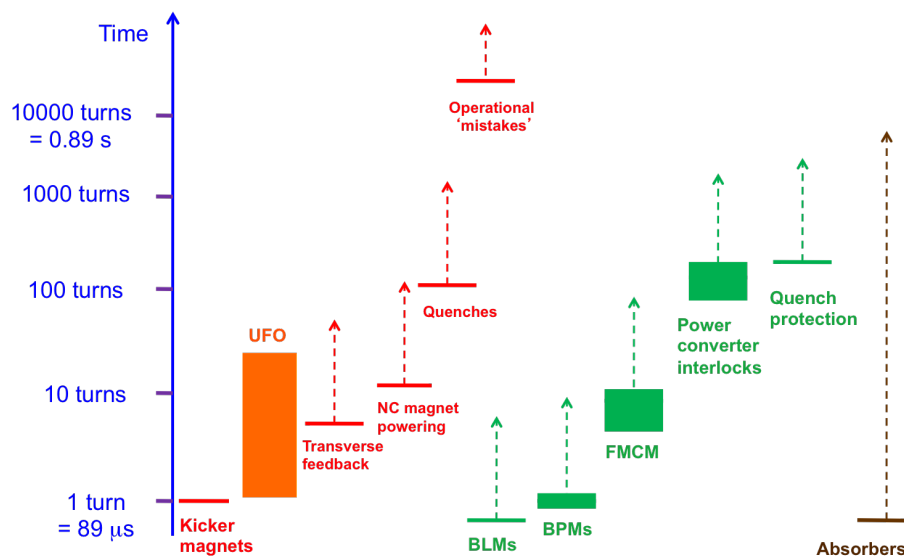


Fig. 4.14: Timescales of ultra-fast and fast failures in the LHC and the reaction times of the respective protection system. Courtesy: J. Wenninger

4.2.5 Failure detection and interlocking

During LHC operation losses have to be monitored and in case of crossing the threshold the beam operation has to be stopped by sending a beam dump request. This subsection gives a short introduction to the Quench Protection System, the different beam loss monitors and the beam interlocking system (BIS).

Quench Protection System

The Quench Protection System (QPS) protects against magnet quenches. The QPS system monitors the voltage across the superconducting magnets and bus-bars. When the QPS detects a significant rise of the voltage across a sc magnet the beam dump will be initiated [92].

Beam Loss Monitors

The Beam Loss Monitor (BLM) system is installed to detect particle losses all around the LHC. More than 4000 of these BLMs are installed in the LHC. They are ionization chambers [94], [95]. The lost beam particles create hadronic showers by passing through the magnets and other machine components. These shower particles are detected by the monitors installed on the outside of the accelerator equipment. The BLM system triggers a beam dump via the BIS, in case losses above a certain, equipment, energy and loss duration dependent threshold. This active protection system reacts on the timescale of $40 \mu\text{s}$. All these detectors are interlocked [96].

In regions where high losses are expected (collimation IRs, beam dump section, beam dump line) secondary electron emission monitors (SEM) and low ionization chambers (LIC) were installed to avoid saturation effects in the standard ionization chambers [97].

During 2012 run also diamond based particle detectors were installed. As they have a very fast reaction time in the order of nanoseconds, their application is the detection of bunch-by-bunch losses, injection and extraction losses and other fast loss scenarios (UFOs, etc.) [99], [61]. For the 2015 run it is planned to measure in addition the abort gap population in IR4 with this kind of detector [100]. This detector type is not yet interlocked, but their data will be saved in the post-mortem storage.

Beam Interlock System

The LHC Beam Interlock System (BIS) is required to safely operate the LHC with beam. The BIS permits injection into the LHC when all systems connected to the Beam Interlock System are ready for beam. When the beam is circulating, it transmits any beam dump request from more than 20 connected User Systems to the Beam Dumping System. Examples for User Systems are the Beam Dumping system itself, QPS, Beam Loss Monitors, Powering Interlock Systems for superconducting and normal conducting magnets, collimators, RF system, Injection Kickers, Vacuum system, Access Safety System, SPS extraction, the LHC experiments, etc. All these users have an interface to the Beam Interlock System. Besides this, functionality plays an important roll for diagnostics of all connected systems during LHC operation [43] [93]. Furthermore the system should:

- Avoid triggering unnecessary beam dumps.
- In case of beam dump or other failures, send a correct diagnostic messages to the operator. For multiple alarms when one initial failure causes subsequent failures, the system should register the time sequence for the failures as they appear.
- Assist the operation of the machine: The diagnostics for failures should be easy to understand.

There are more than 10000 interlock conditions to abort the beam.

The BIS consists of 17 controllers (BIC) distributed around the LHC. The users systems are connected to the nearest BIC. Each controller collects beam permit signals (TRUE for no failure and FALSE in case of a failure) from the user systems creates a local beam permit signal. In case of a failure the BIC act as an optical switch transmitting (local beam permit = TRUE) or not transmitting (local beam permit = FALSE) a generated frequency around the LHC. A distortion in the frequency (removal of beam permit) of this signal will be detected by the LBDS and it will trigger the extraction process [43]. The whole process, from the failure detection, removing the beam permit signal until the beam is extracted takes not more than 3 LHC turns.

4.3 Material damage

In the new generation of high-power accelerators the stored beam energy has sufficient power to reach and to pass over the damage thresholds of the most robust

materials. For the near beam components like collimators which can potentially hit by the beam, lot of effort has been put in the material choice and design, their robustness at beam impact has been studied with simulation tools but it is difficult to predict their behavior in an accidental case. To avoid destructive accidents during operations, which will lead to costly down-time of the accelerator, new devices should be tested before their installation for sufficient robustness. These tests should be performed in as realistic as possible conditions to their future operation. The goal of this experiments is to demonstrate the dimensions of the damage. In 2011 a new dedicated facility, High Radiation to Materials, designed to study beam impacts on materials and accelerator components went operational.

4.3.1 HiRadMat - Facility

The High-Radiation to Materials (HiRadMat) facility at CERN was designed to provide high-energy and high-intensity pulsed beams, extracted from the Super Proton Synchrotron (SPS), to an irradiation area where material samples like accelerator component assemblies can be tested in comparable conditions as during realistic failure cases (e.g. asynchronous beam dump, beam impact on collimator) in an accelerator [38], [39].

Previous assumptions for the damage limit were based on static Monte-Carlo simulation tools like FLUKA. In these cases the bunch structure of the beam was not taken into account. In the case of the full LHC beam impacting into the aperture the damage would be much more severe than static simulations would predict. Therefore the effects of bunched beam impacting on material have been studied since 2004 [30], [31], [32]. With the HiRadMat facility it was possible to study these effects experimentally. Beyond that, experiments in HiRadMat can contribute to the understanding of the behavior of materials under beam impact, providing important feedback for the design of new high-power accelerators and spallation target stations.

HiRadMat is located in the West Area of the Super Proton Synchrotron (SPS), in the so called TNC tunnel. It shares the extraction line TI2 from SPS to the Large Hadron Collider (LHC). The beam is extracted with a particle momentum of 440 GeV/c and with single bunch intensities from 1×10^8 to 1.7×10^{11} protons. A maximum of 288 nominal bunches (i.e. total 4.89×10^{13} protons) with a total pulse energy of 3.4 MJ can be extracted. The bunch spacing is adjustable within 25, 50, 75 or 150 ns. The beam size can be tuned from $\sigma = 0.1$ mm to 2 mm to match the needs of the respective experiment. The facility consists of three platforms for experiments. The beam has a focal point at the beginning of each test stand. A beam dump is located downstream of the experimental area. A crane is available in the facility to allow a remote installation and removal of the equipment onto the experimental table stations and to the cool-down area, located downstream of the beam dump. Beam instrumentation is installed along the transfer line allowing quantifying beam parameters like transverse positions measured with Beam Position Monitors (BPMs) [38]. Beam Observation TV Monitors based on Screens (BTVs) are installed to monitor the transverse beam size. The bunch intensity is measured by Fast Beam Current Transformers (FBCT) located in the SPS, at the extraction and in the



Fig. 4.15: Picture of the HiRadMat tunnel with the last focussing and bending magnets (light blue), the platforms (yellow on the floor) for the experimental tables and the beam dump at the end of the tunnel.

transfer line. The area is equipped with Beam Loss Monitors (BLMs) to measure beam losses along the beam line. BLMs are also mounted at each experimental table station and at the beam dump block.

Figure 4.15 and Figure 4.16 show two pictures of the HiRadMat tunnel. The first picture shows the beam line including the last focussing and bending magnets (light blue on the left side). The second picture is focussed on the last two experimental table stations (orange on the ground), each one is equipped with a BLM (yellow tube). On the right side the beam dump block is visible (green, yellow, orange blocks).

A schematic drawing of the HiRadMat - tunnel area is shown in Figure 4.17. The entrance area is labeled with TJ7, the experimental tunnel goes to the right (TNC), the beam dump is colored in red and the cool down area is located downstream of the beam dump. The complete area is located in the underground of the BA7 access point to SPS, the access shaft is located in TA7 [38].

4.3.2 Damage experiments

In 2012 nine experiments were performed to study the damage due to proton beam impact using multiple bunches (e.g. target of the radioactive ion beam (RIB) target of ISOLDE, robustness of a SPS absorber block (so-called TPSG), damage test on LHC collimator, hydrodynamic tunneling experiment, robust collimator material development and test for crystal collimation) in addition beam instrumentations (for Radio Protection and BLM) were studied in a high-fluence environment.

During this PhD a contribution to three of these experiment was given, namely, septum protection test, crystal collimation experiment and the hydrodynamic tunneling experiment.

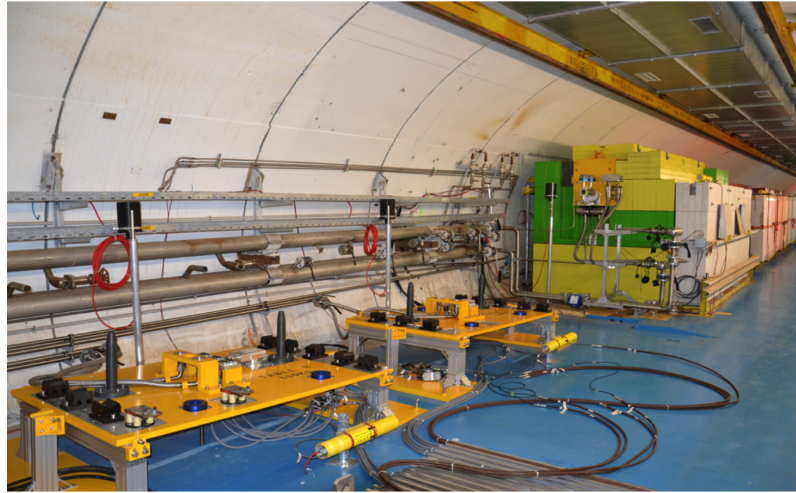


Fig. 4.16: Picture of the HiRadMat tunnel with the focus on the last two platforms (yellow) for the experimental tables and on the beam dump further downstream.

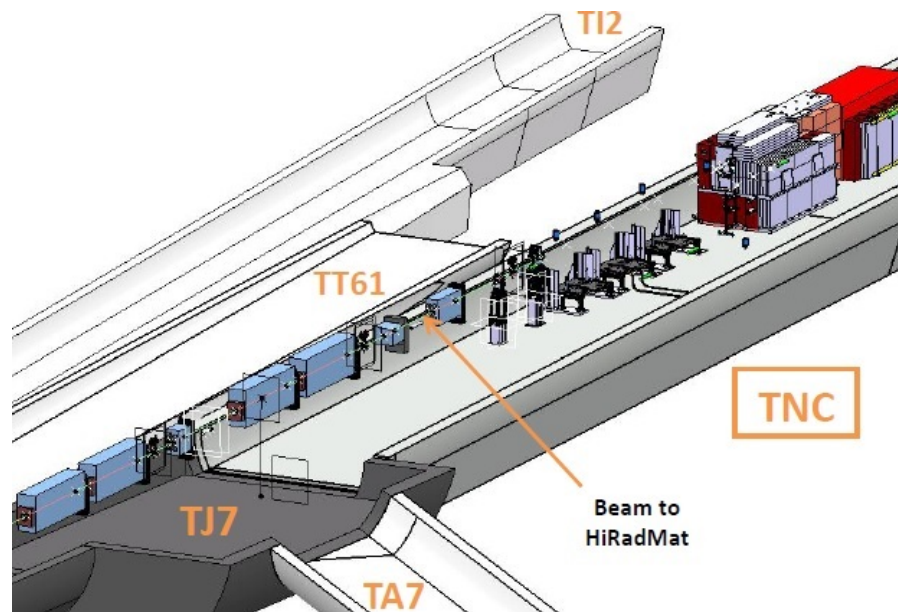


Fig. 4.17: Schematic drawing of the HiRadMat tunnel area, entrance area (TJ7), the experimental tunnel goes to the right (TNC), the beam dump is colored in red and the cool down area is downstream of the beam dump [38].

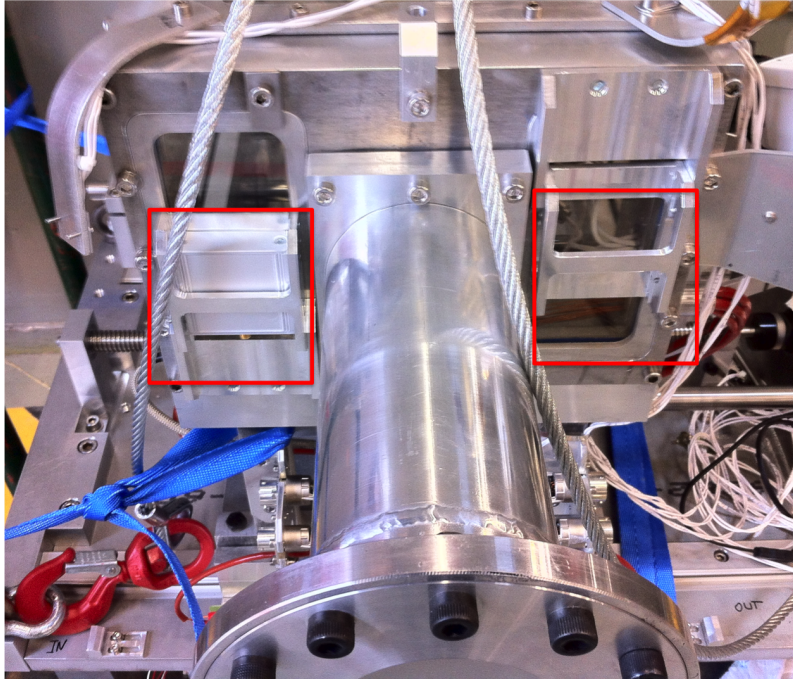


Fig. 4.18: UA9 crystal experiment setup with the support of the dBLMs (red rectangles). The right detector is not yet installed.

Hydrodynamic tunneling experiment

Mid 2012 the 440 GeV SPS proton beam was sent on solid copper cylindrical targets to study the damage potential of high energy beams and to verify simulations which have shown that the full impact of the LHC beam onto solid copper can cause a hydrodynamic tunneling effect [43]. A detailed description of this experiment will follow in Chapter 6.

UA9 crystal experiment

In the second experiment a crystal was irradiated to measure their robustness and integrity. These crystals might be used as primary deflectors in the LHC collimation system in the future. This test was used to evaluate the risk associated to the installation of such a crystal in the LHC [40]. For this experiment 500 μm thick polycrystalline diamond based particle detectors were used for the first time to align the crystal to the beam. The detectors were installed symmetrically to the beam axis on the target tank. Figure 4.18 shows the experimental setup. The red rectangles indicate the position of the diamond particle detectors (dBLM). The left one is already installed, the right detector support is still empty.

A stainless steel strip is fixed in a defined distance from the crystal was installed for alignment purposes. The steel strip was moved through the beam, creating secondary particles. They were detected by two diamond detectors located downstream left and right side of the beam axis. At the maxima of the diamond detector signals, the strip was placed in the beam producing the highest amount of shower particles.

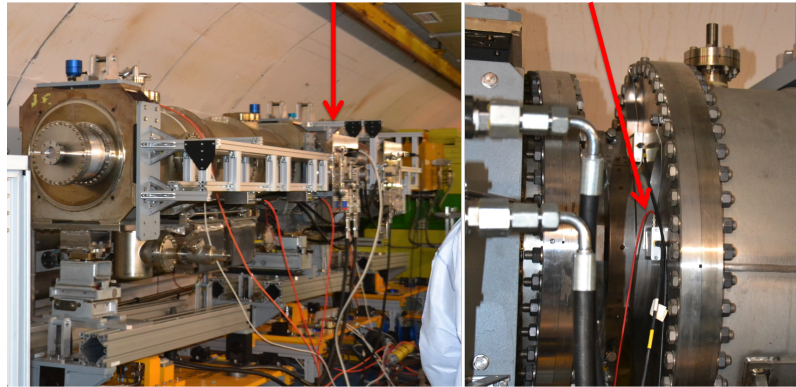


Fig. 4.19: Septum magnet irradiation setup. The red arrows on the left picture indicates the position of the dBLM. The right picture shows a picture from a different perspective with an arrow pointing on the diamond detector.

Septum magnet protection

During the last experiment a SPS-absorber (TPSG) was irradiated. The TPSG protects the septum magnet against damage in case of a kicker failure. The robustness of the device and its protection efficiency for the septum magnet was tested [41]. In this experiment one 500 μm thick polycrystalline diamond based particle detector was installed to ensure that the beam hits the target. A picture of the setup with the tank and the position of the dBLM is presented in Figure 4.19. Fluence simulations in comparison to experimental results showed that the target was hit by the beam.

5. DIAMOND PARTICLE DETECTORS FOR DAMAGE EXPERIMENTS

In the following the properties, structure and behavior of diamond based particle detectors for damage and high fluence experiments are discussed. These detectors have a nanosecond time resolution and they are radiation hard. A short introduction to the diamond material and the signal creation is given. A more detailed overview can be found in literature. In addition, the properties of the dBLMs used within this PhD work will be discussed.

5.1 *Diamond material*

Carbon atoms crystallize in a face-centered cubic (fcc) lattice, with two atoms at each lattice point, one at $[0, 0, 0]$ and the other at $[1/4, 1/4, 1/4]$, and are classified as diamond. The density of diamond is 3.52 g/cm^3 , the molar mass of natural carbon is 12.01. The atomic density of diamond with $1.76 \times 10^{23} \text{ atoms/cm}^3$ [53] is the highest on earth. The Carbon atoms in diamond are strongly bound to each other, with a cohesive energy of 3.62 eV/bond or 7.24 eV/bond respectively [54] [55]. The fact that diamond is the hardest natural material and the relatively high displacement energy of 43 eV/atom result from these strong covalent bonds. The hardness of diamond is dependent on the crystal orientation [56]. Within a natural diamond crystal lattice imperfections can be found, which are due to the formation process of the diamond or irradiation effects. These crystal defects distort the periodicity of the lattice and can change the electronic properties of the material [54].

- Zero-dimensional defects are either carbon or foreign atoms, like nitrogen or hydrogen, which take an irregular place in the lattice. Such point defects the crystal lattice locally. These foreign atoms can be incorporated in the diamond bulk during the production process. The quality of a diamond can be classified after the amount of nitrogen which can be found in the lattice, the best quality diamond material is nearly N free.
- One-dimensional defects can be explained by discontinuity of the crystal plane.
- Grain boundaries are two-dimensional defects. They can be found where two crystal grains with different orientation meet. The electronic quality of diamond depends strongly on the density of these grain boundaries as they act like charge trapping centers.
- Bulk defects are three-dimensional. These are regions where many defects or graphite inclusions and foreign atoms cluster can be found. Especially graphite

inclusions change the electronic properties of a diamond significantly. [54]

Besides of natural diamond, which is very limited, two types of artificial diamond are available [72], high pressure high temperature (HPHT) diamond and chemical vapor deposition (CVD) diamond. With the HPHT method graphite is converted into diamond in an environment of 1500 - 2000 Celsius and pressure of up to 50 - 100 kbar supported by suitable catalysts [57], [58], [54]. The plasma-assisted CVD technique allows to grow diamond on a suitable seed. The principle of this method is based on chemical reactions occurring in a gas phase above a solid surface and consequently deposition of material onto the surface. Methane (CH_4) is generally used as carbon supply for the diamond growth in this technique. In combination with hydrogen gas (H_2) it provides the reactants in the gas phase. Atomic hydrogen in the plasma reduces methane to carbon or reactive radicals like CH_3 , which eventually deposit on the cooled surface of the seed. In addition atomic hydrogen etches graphite from the surface, prevents the built up of polymers and keeps the diamond lattice stable by terminating the surface [54], [59].

Besides the chemical conditions in the reaction chamber, the seed that is used for the diamond growth governs the quality of the resulting diamond and hence its electronic properties. There are two different method for the CVD growth [54]:

- pCVD diamond: For the synthesis of poly-crystalline chemical vapor deposition (pCVD) material, diamond nano crystals or poly-crystalline diamond are used as substrate [71]. The resulting diamond bulk contains grain-boundaries with crystal, growing from different seeds. However, the electronic properties of this material are less favorable as these boundaries act like charge trapping centers for free charge carriers. These diamonds can be used for beam-loss monitoring [60], [61], beam conditions monitoring, in high-fluence environment [62] and time of flight measurements in accelerator environments [54]. A microscopic picture of the pCVD grain structure can be found in Figure 5.1. Within this thesis only pCVD diamonds are discussed.
- sCVD diamond: For the synthesis of high quality single-crystal chemical vapor deposition (sCVD) diamonds the substrate of choice is usually a surface-treated HPHT diamond. The sCVD diamond is separated from the HPHT substrate after the growth by laser-cutting and polished to the desired thickness and surface smoothness. High quality electronic grade diamonds are grown in this way. The area of these diamonds is restricted to about $4.5 \times 4.5 \text{ mm}^2$, due to the size of the HPHT seeds. The thickness of the available substrates is typically $500 \mu\text{m}$ [54].

Diamond is an insulator in terms of conductance. For detector applications it is more suitable to classify it as wide band-gap semiconductor. The band-gap of diamond is 5.47 eV, this leads to a free charge carrier density of less than 10^3 cm^{-3} at room temperature [63]. Therefore diamond is a very low-noise detector material, which can be used at high and cryogenic temperatures [64], [65]. The dielectric constant of diamond is $\epsilon_r = 5.7$ (in comparison to silicon $\epsilon_r = 11.9$), this reduces the capacitance for a given detector-geometry, which is an advantage in measurements.

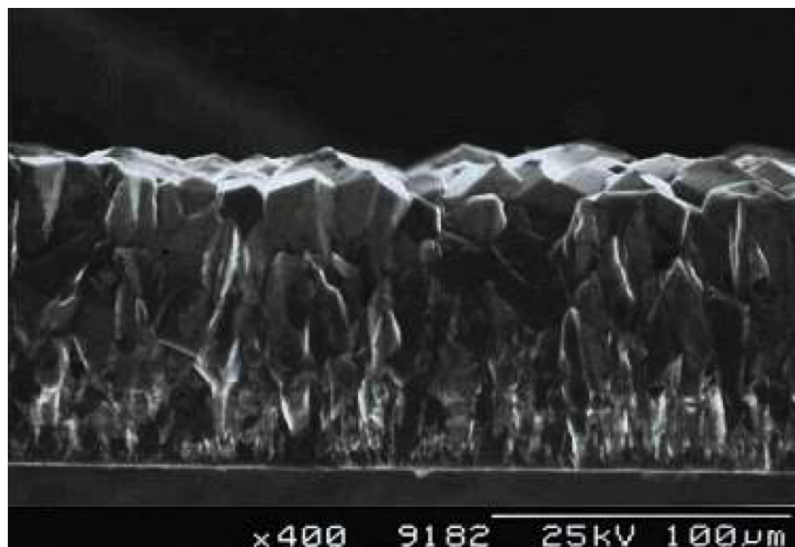


Fig. 5.1: Grain structure of polycrystalline diamond material [43].

The intrinsic resistivity of a sCVD diamond can exceed $10^{16} \Omega\text{cm}$. With a bias voltage of $1\text{V}/\mu\text{m}$ the leakage current is less than 10^{-12}A [54]. Crystal defects can lower the resistivity of diamond up to an electrical shortcut, which would be the case for graphite inclusions which extend through the whole thickness of the diamond bulk. The energy needed to create an electron-hole pair in diamond is predicted to be $\epsilon = 11.6\text{eV}/\text{e-h}$ from theoretical calculations [54]. The published experimental values vary in a range of 11.1-24eV. In this thesis the value $\epsilon = 13.6\text{eV}/\text{e-h}$ is used as a reference [59]. The mobility of charge and therefore their drift velocity values varies over a wide range, depending on the crystal quality. Measurements at CERN showed values for the electrons of $\mu_{0,e^-} = (1530 \pm 160)\text{cm}^2/\text{Vs}$ and for the holes of $\mu_{0,h^+} = (2660 \pm 160)\text{cm}^2/\text{Vs}$ [54]. These measurement are consistent within the range of reported values [66] [67]. The drift velocities explains the nanosecond response of a diamond based particle detector.

5.2 Signal creation in a diamond based detector

The working principle of a diamond based particle detector is similar to a gaseous ionization chamber. The diamond is metallized on both surfaces. A high voltage is applied to the metallization resulting in an electric field in the diamond bulk, usually a field strength of $\sim 1\text{V}/\mu\text{m}$ is used [70].

If an ionizing particle is entering the diamond bulk, free charge carriers, namely electrons (e^-) and holes (h^+) are created. A minimal ionizing particle (MIP) creates on average 36 electron-hole pairs per μm of diamond when it passes through [73]. A charge cloud with density $\rho_{ion}(x, y, z, t)$ forms along the path of the particle. If an electric field is applied, the charges are moving through the diamond bulk to the respective electrode, following the Lorentz force F :

$$F = q \cdot [\mathbf{E} + (v_{drift} \times \mathbf{B})] \quad (5.1)$$

with the particle charge q , the electric and magnetic field \mathbf{E} and \mathbf{B} and the drift velocity v_{drift} . Since self space-charge forces are weak, the uniform bias field and the field from trapped charges (if present and uniform) will dominate and a uni-dimensional model can be assumed. Hence, for a parallel-plate capacitor, with $E = U/d$, where U is the applied voltage and d the thickness of the capacitor and in absence of a magnetic field ($\mathbf{B} = 0$) the above expression simplifies to:

$$F = q \cdot \frac{U}{d} \quad (5.2)$$

Schockley and Ramo expressed the instantaneous current I induced on the electrodes of a vacuum tube by a moving charge q as:

$$I = q \cdot \frac{v_{drift}}{d} \quad (5.3)$$

with the drift velocity v_{drift} and the thickness of the device d [68], [70]. The so-called Shockley-Ramo theorem states that the current can be expressed in an electrostatic way at each moment of charge movement. Neglecting the self space-charge field, v_{drift} can be expressed as a function of the electric field, $v_{drift} = \mu E$, using the mobility μ of charge carriers in a material. With this expression the current becomes a function of E ,

$$I = \mu E \frac{q}{d}. \quad (5.4)$$

Dividing this expression by the active area of the sensor and using the charge density $\rho_{ion}(t)$, leads to an expression for the current density $i(t)$:

$$i(t) = \rho_{ion}(t) \mu_{ion} E. \quad (5.5)$$

The current is a superposition of the electron and the hole movement, where $\rho_{ion}(t) \mu_{ion}$ represents the sum of them:

$$\rho_{ion}(t) \mu_{ion} = [\rho_{e-}(t) \mu_{e-} + \rho_{h+}(t) \mu_{h+}] [54]. \quad (5.6)$$

In natural diamonds, crystal defects in the form of impurity atoms, dislocations, stacking faults and grain boundaries can be found. These defects act as charge trapping centers and can enhance the recombination of free charge carriers. The loss of charge carriers along their path through the bulk can be expressed by their lifetime τ_{ion} . Therefore Equation 5.5 needs to be re-written as:

$$i(t) = \rho_{ion}(t) \mu_{ion} E \exp\left(-\frac{t}{\tau_{ion}}\right) \quad (5.7)$$

For ideal diamond τ_{ion} is infinite and the current density is not affected by the exponential term anymore. In pCVD materials the effect of the exponential term is dominant as charges recombine or get trapped during their drift. The Shockley-Ramo theorem [68] implies that the collected charge at the electrode is equivalent to $q \cdot x_0/d$, where x_0 is the drift path of the free charge carrier with charge q . Only the simultaneous creation of electron-hole-pairs and their respective movement to the opposite electrodes guarantees the effective charge drift over the full length d and hence the full charge collection. The average drift length of the charge is called the charge collection distance (CCD). In fact, the CCD is the sum of the average drift lengths of electrons and holes. The CCD is related to the charge collection efficiency (CCE) by the relation:

$$CCD = CCE \cdot d = \frac{Q_{meas}}{Q_{ind}} \cdot d \quad (5.8)$$

with the measured charge Q_{meas} and the induced charge by the ionizing particle Q_{ind} . The CCD and the equivalent CCE are figures of merit for the quality of a diamond detector. A good quality sCVD diamond can have a CCE of 90 % to 100 % and reaches this value at electric fields of $\sim 0.2 \text{ V}/\mu\text{m}$ [70]. Standard LHC pCVD diamonds have a CCE of 25 % to 45 %, whereas special high-fluence environment pCVD diamonds have a CCE of 4% to 15 %.

For a minimum ionizing particle 36 e-h pairs are on average created per μm . The created charge cloud is extended from one electrode to the other and electrons and holes are absorbed on the corresponding side from the very beginning. This results in a triangular pulse shape as free charge carriers are constantly absorbed by the electrodes. Signals recorded when irradiating a pCVD and a sCVD detector with a ^{90}Sr source can be seen in Figure 5.2. The β particles from this source traverse the 500 μm diamond and can be classified as MIP particles. The signal shapes for both diamond detectors are triangular. The signal from the pCVD detector is smaller, which can be explained by the lower CCE. In addition, the falling edge of the pCVD signal is more exponential than linear. This indicates that free charge carriers are trapped on the way to the electrodes [54].

5.3 Properties of the used dBLMs

During the experiments described in this thesis two types of diamond detectors were used.

- pCVD diamond (from Diamond Materials Company) with a diameter of 5 mm, a thickness of 100 μm and gold electrodes with a diameter of 3 mm [69]. The bias-voltage was 100-130 V, i.e. electric field of 1-1.3 $\text{V}/\mu\text{m}$. The charge collection efficiency (CCE) was measured to be 4 to 15 %. Capacitors of 111 nF are installed to compensate for the detector discharge.
- pCVD diamond (from Element 6 Company) with a surface of 1x1 cm^2 and a thickness of 500 μm [69]. The bias-voltage was 500 V, i.e. electric field of 1 $\text{V}/\mu\text{m}$. The charge collection efficiency (CCE) was measured to be 30 - 40 %.

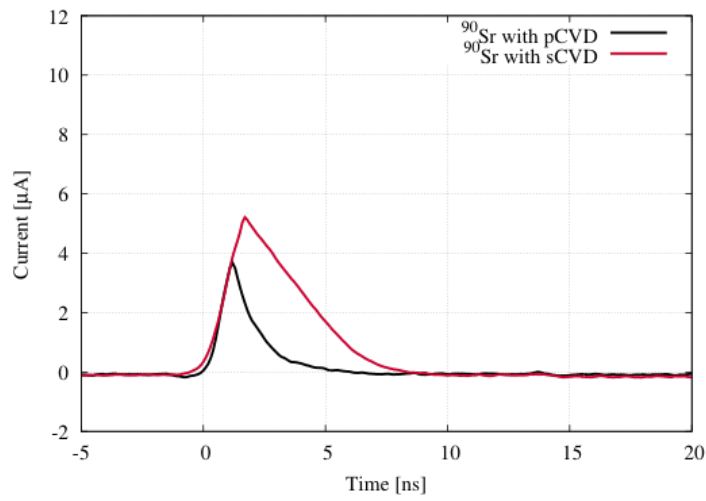


Fig. 5.2: Average signals of a pCVD (black) and a sCVD (red) detector when irradiated with β from ^{90}Sr [54].

These detectors are completely RF-shielded [69]. For the first type a minimal rise time of 1.6 ns and for the second type a minimal rise time of 1.2 ns was measured.

6. HYDRODYNAMIC TUNNELING EXPERIMENT

In 2012, a novel experiment has been performed at CERNs HiRadMat facility to study the impact of a 440 GeV proton beam, extracted from the Super Proton Synchrotron (SPS), on solid copper cylinders [43]. As damage experiments at the LHC are not possible, benchmarking the simulations with the HiRadMat experiment is a necessary step to verify the simulated results, the simulation routine and, afterwards a possibility to extrapolate these results to LHC beam parameters. This chapter gives a detailed description of the experimental setup, the target investigations and the final experimental results.

6.1 *Description of the experiment*

Figure 6.1 shows the target assembly in the workshop before the installation in the HiRadMat facility. The experiment consists of three targets, each comprised of fifteen copper cylinders with a spacing of 1 cm in between. Previous simulations showed that the gap has no impact on the hydrodynamic processes and particle interactions but it will give a way for a visual inspection after the irradiation and cool-down phase [42]. Each cylinder has a radius $R = 4$ cm and length $L = 10$ cm. The three targets are enclosed in an aluminum box that provides rigidity to the setup. The front face of the first cylinder and the rear face of the last cylinder in the three target assemblies are covered with cylindrical aluminum caps. Each cap has a radius of 4 cm, a length of 18.5 cm, and hole of 1 cm diameter that allows the beam to pass through. The end caps and the aluminum box should also protect the area against contamination from ejected material. The target assembly is mounted onto a movable table which allows to center each target into the beam and moving the setup fully out of the beam. The closed target with the aluminum end caps can be seen in Figure 6.2.

For this experiment, the proton beam energy was 440 GeV, the bunch intensity was 1.5×10^{11} protons, a bunch length of 0.5 ns and bunch separation of 50 ns was chosen. Target 1 was irradiated with 144 bunches with a beam size $\sigma = 2$ mm. Target 2 was irradiated with 108 bunches, target 3 was irradiated with 144 bunches both with a beam size $\sigma = 0.2$ mm. The beam parameters for the three experiments are presented in Table 6.1. The first target was used to get a reference in which only less hydrodynamic tunneling is expected, therefore the lowest energy density with $\sigma = 2$ mm was chosen. For target 2 moderate and for target 3 significant tunneling was expected.

The set-up was equipped with 11 temperature sensors (PT 100), three secondary electron multipliers (SEM) and three diamond based particle detectors to measure

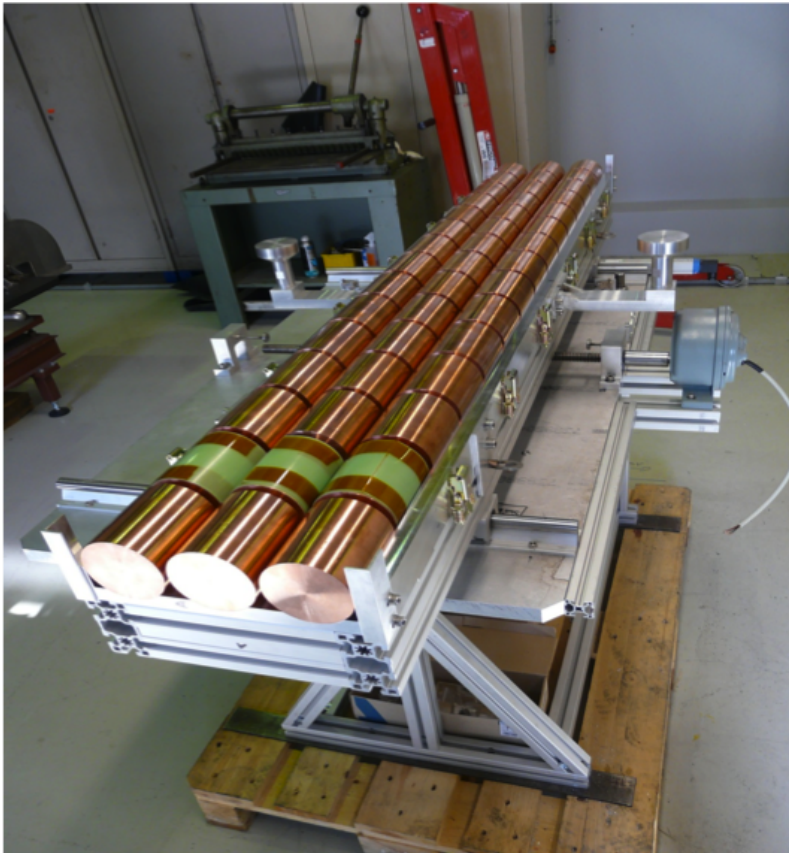


Fig. 6.1: Three target assembly on the movable table in the workshop before its installation in HiRadMat. Each target consists of 15 copper cylinders with a radius of 4 cm and a length of 10 cm lying in the aluminum box. Target 1 (left), target 2 (middle) and target 3 (right). The strain gauges are insulated with green glass epoxy G11.

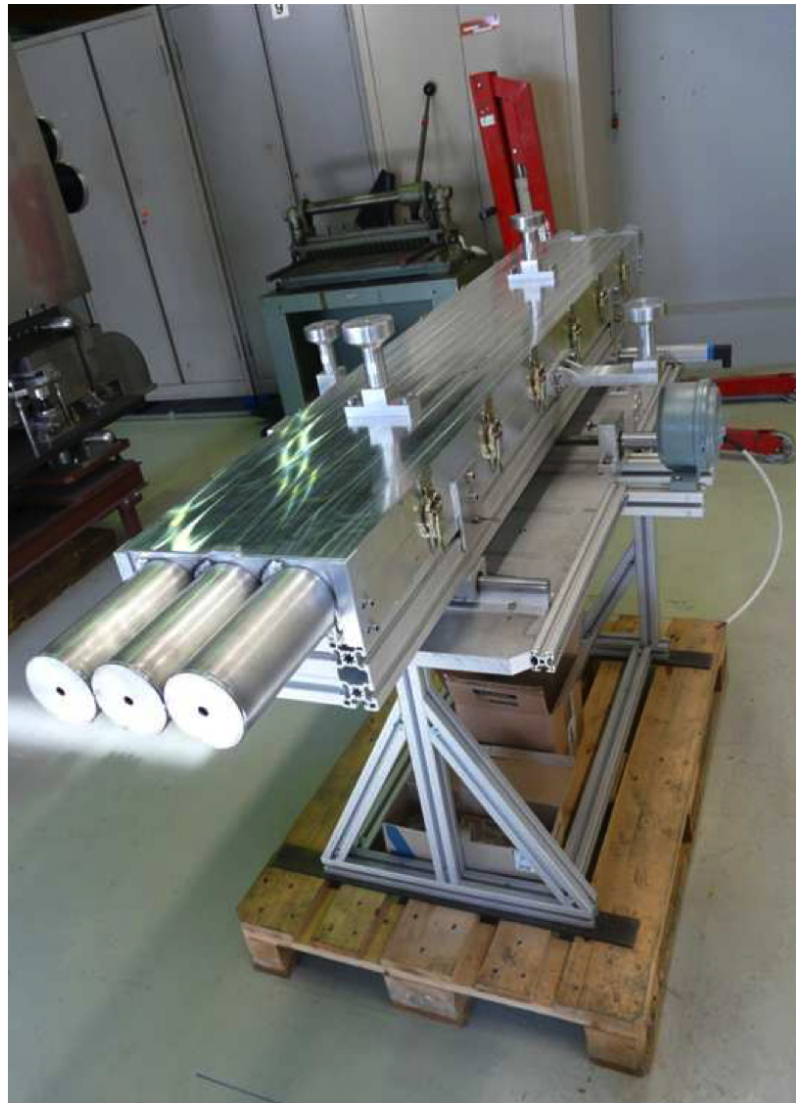


Fig. 6.2: Closed target assembly with the aluminum end caps.

Tab. 6.1: Experimental beam parameters and tunneling expectations for the three targets. The particle energy was 440 GeV.

Target	Number of bunches	Beam $\sigma_{x,y}$ (mm)	Beam energy (MJ)	Expectations
1	144	2.0	1.52	Some tunneling
2	108	0.2	1.14	Moderate tunneling
3	144	0.2	1.52	Significant tunneling

the particle showers. Strain gauges were installed to measure the pressure waves online. This was chosen as the cool-down time before the first visual inspection was expected to be very long (8 month). Unfortunately most of the temperature sensors were destroyed due to radiation damage during the experiment, the SEMs had an electronic problem and strain gauges were blind during the irradiation due to the high radiation. Only the diamond detectors gave reliable results [43]. This thesis is also focussed on diamond detectors, therefore their results will be discussed in chapter 9.

The beam of 144 bunches, respectively 108 bunches were subdivided in trains of 36 bunches with a bunch spacing of 50 ns. The bunch trains were separated by 250 ns. The irradiation time for Target 1 and Target 3 was 7.95 μ s. The irradiation time for Target 2 was 5.9 μ s. Figure 6.3 shows the temporal profile of the delivered 144 bunches proton beam as recorded by the diamond particle detectors. The decay of the amplitude is due to diamond detector electronics, it is the discharge of the supply capacitance in the diamond detector. Figure 6.4 shows a zoom of the time structure around the gap between two neighboring bunch trains. The gap between bunches and between bunch trains is clearly visible.

Figure 6.5 shows the target installed in the HiRadMat-tunnel. The dBLMs are mounted on the three aluminum arms on top of the experimental setup with a distance of 50 cm to the beam axis.

6.2 Target investigations

The target was opened for visual inspection after eight months of cool down in February 2013. It was not allowed at that time to physically touch the targets due to radio-protection issues. Droplets and splashes of molten and evaporated copper have been found on the copper cylinders. Furthermore traces of copper were visible on the aluminum housing at the position of the gaps between cylinders and in the front aluminum caps. Figure 6.6 shows a photograph of the front aluminum caps around the first cylinder of the three target assemblies after irradiation. The cap of target 1 (left) shows no traces of copper. The cap of target 2 (middle) shows some splashes of the molten or evaporated copper, whereas the cap of target 3 (right) shows significantly more material projection. A visual inspection of the target confirmed that the front face of the first cylinder of target 1 was not damaged, while in case of target 2, some damage was observed. For target 3, a damage at the position of the beam impact was clearly visible.

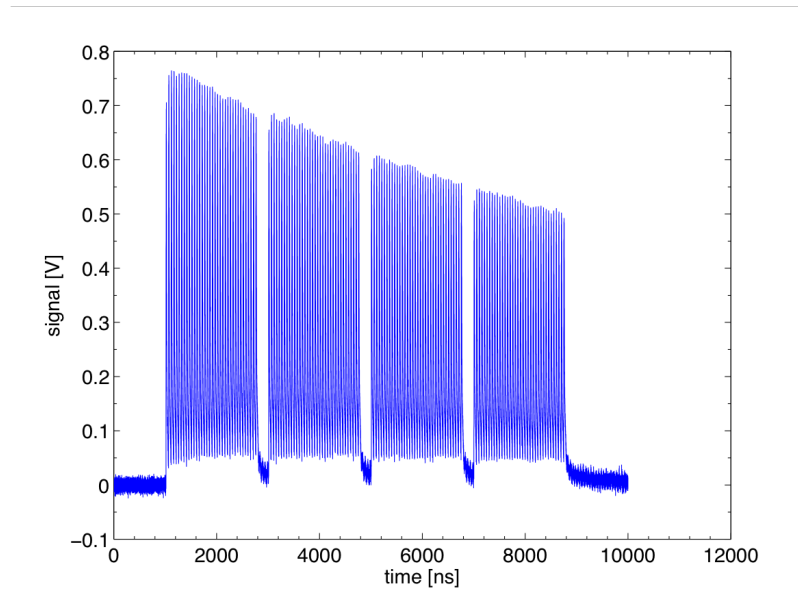


Fig. 6.3: Temporal profile of the 144 bunches proton beam, recorded with a diamond detector. The decay of the signal amplitude does not indicate a droop of the bunch intensity, it is due to a discharge of the supply capacitance in the diamond detector. The bunch intensity was constant along the four trains.

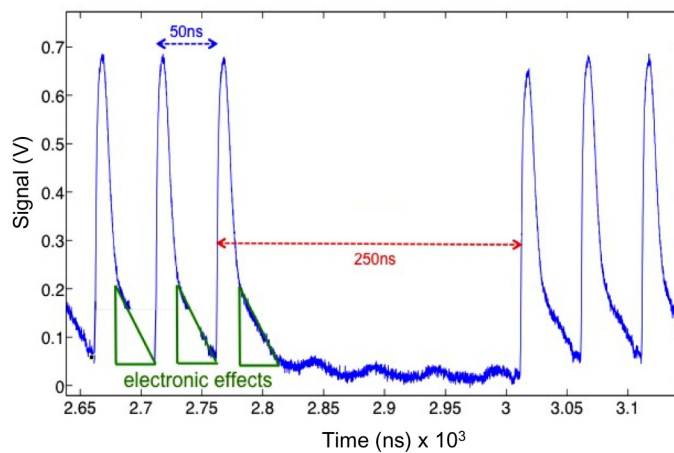


Fig. 6.4: Time structure of the proton beam with 50 ns gap between two bunches and a gap of 250 ns between two bunch trains of 36 bunches. The signals were recorded with one of the installed diamond particle detectors.



Fig. 6.5: Hydrodynamic tunneling experiment installed in the HiRadMat facility. The dBLMs are mounted on the three aluminum arms on top of the experimental setup.

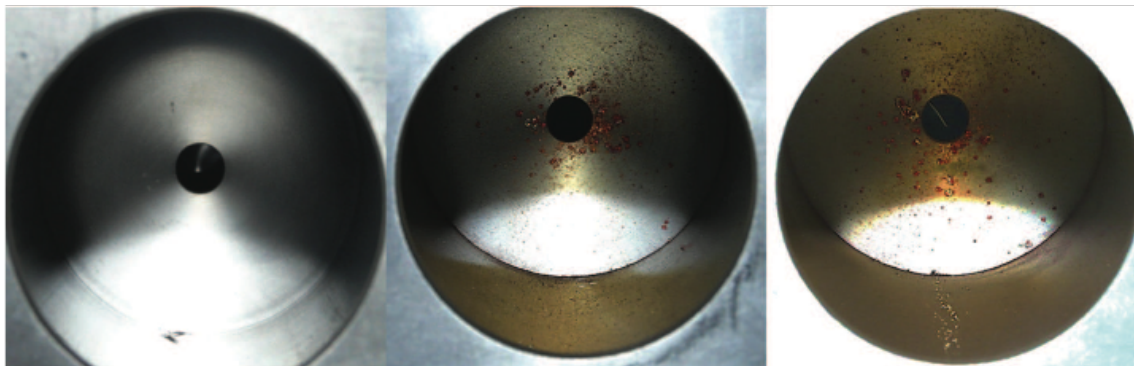


Fig. 6.6: View into the inside of the aluminum end caps mounted at the front end of the experimental setup. Left: Target 1, no splashes, this indicates that the front face of target 1 was not damaged. Middle: Target 2, some splashes in the aluminum cap. Right: Target 3, significantly more material projected from the front face into the aluminum cap.

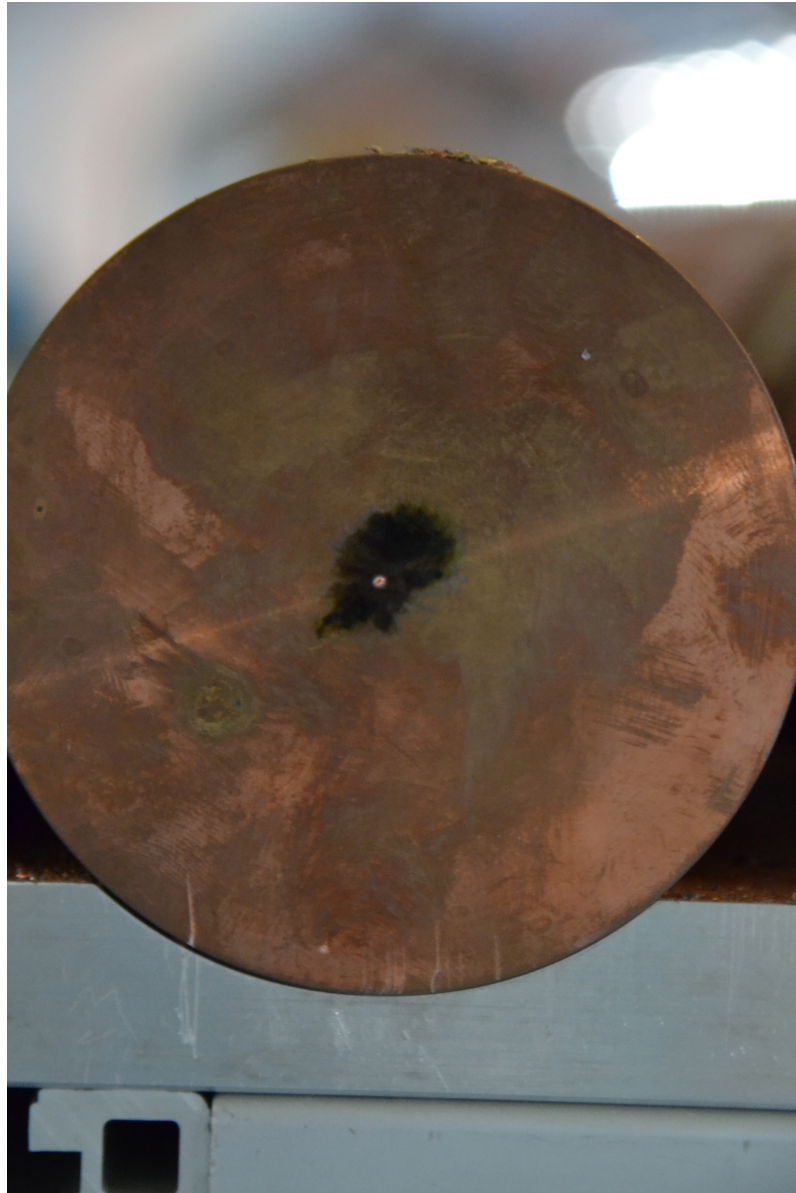


Fig. 6.7: First cylinder of target 3. The bright dot in the middle indicates the point where the beam impacts on the target. This area was molten, a part of the molten copper was ejected to the end caps and the area later solidifies.

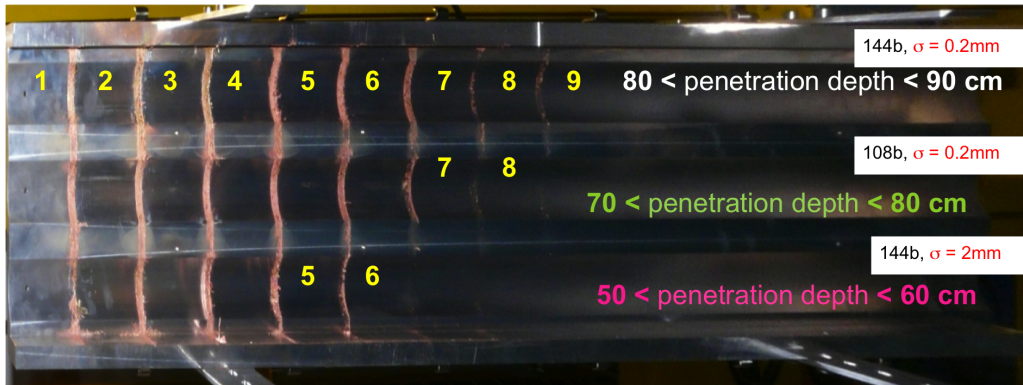


Fig. 6.8: Top cover of the experimental setup after the irradiation. Traces of molten copper on the cover indicate the penetration depth of the proton beam.

A picture of the front face of the first block is shown in Figure 6.7. In Figure 6.8, a photograph of the aluminum top cover of the target is shown. After the beam impact, molten and evaporated material is projected outwards and is deposited on the top cover. The traces of the projected copper between the 10 cm long cylinders are clearly visible. It can be seen that in case of the target 1 (bottom), the splash of molten copper occurs up to the gap between the fifth and the sixth cylinder. That means that the material was molten or evaporated over a length of 55 ± 5 cm. For target 2 (mid), the molten or evaporation zone goes up to the eighth cylinder that means a damage length of 75 ± 5 cm. In target 3 (top), the molten or evaporation zone is extended to the ninth cylinder that means a length of 85 ± 5 cm. These numbers were proved by checking front and end plate of the last damaged cylinder. For the given numbers, the front plate of the cylinder was damaged, whereas the end plate shows no damage. It was decided that the first cylinder of target 3 and the last irradiated cylinders of each target, namely, cylinder 6 of target 1, cylinder 8 of target 2 and cylinder 9 of target 3 should be removed after another 11 months of cool down, during a second inspection of the target, for further investigation.

During the inspection of the target, it was seen, that the method of protecting the area with the end caps was not fully successful. A small part of ejected material escaped through the hole and led to a contamination of the area. As a consequence, future experiments have to be fully closed.

In January 2015 a second inspection was performed to remove the selected cylinders, remove the target from the HiRadMat cool-down area and take pictures of each cylinder. As an example the front and the back faces of each irradiated cylinder of target 3 is shown in Figure 6.9 to 6.17. For each cylinder the front face is shown on the left, the back face on the right. The beam generates a small damage on the front face of the first cylinder which is in accordance with the traces of material deposited at the inner surface of the aluminum end cap. On the back face a much wider hole exists and traces of the ejected material around the hole that has been solidified after the cooling. The simulated temperature curve shows that the material in the left half of the first cylinder (0-5 cm) is liquefied, whereas a two phase liquid-gas state exists in the right half region (5-10 cm). The ejected material from the back



Fig. 6.9: First cylinder of target 3. The beam enters the target on the front plate (left) the surface is damaged, material is ejected towards the aluminum end cap. At the back face of the cylinder (right) a hole is clearly visible, material is ejected towards the front face of cylinder 2. Reflected copper splashes and ejected splashes from cylinder 2 solidified on the surface. The copper in this cylinder was liquid (first half) and in gaseous state (second half).

face of a cylinder is ejected with high speed and collides with the material ejected from the front face of the following cylinder. The material is partly deposited on the inner side of the aluminum cover and it is partly splashed on the opposite faces of the two cylinders.

The material deposited on the faces of the cylinders solidifies as seen in the right part of Figure 6.9 and left part of Figure 6.10. Similar behavior can be seen in the following pictures. It is clearly visible that the beam has penetrated through all 8 cylinders generating holes at both faces of the cylinders and leaving traces of the material that solidifies after ejection. In the 9th cylinder of target 3 only damage on the front face was visible.

6.3 Cylinder cutting and microscopic analysis

The selected cylinders were brought to a workshop for radioactive materials (special radio-protection safety procedures and careful disposal of the radioactive waste) to investigate the depth of the hole generated by the beam. Cylinder 1 of target 3 and Cylinder 6 of target 1 were directly cut longitudinally, Cylinder 8 of target 2 was cut in two slices of 2.5 and 7.5 cm before cutting it longitudinally. The cylinders were cut with a saw, afterwards the surface was treated with a rotating milling cutter to get rid of the coarse traces from the saw. With this method the material was removed in steps of 0.05 mm. Light traces of the milling machine are visible on the copper. A picture of the milling process can be found in Figure 6.18.

The pieces were brought to a microscopic laboratory for further investigation. Figure 6.19 shows the first cylinder of target 3 cut along the beam axis. In the first 2.3 cm micro cavities are observed, further downstream a cone shaped hole is clearly visible. This picture of the surface was made using a standard camera. A detailed

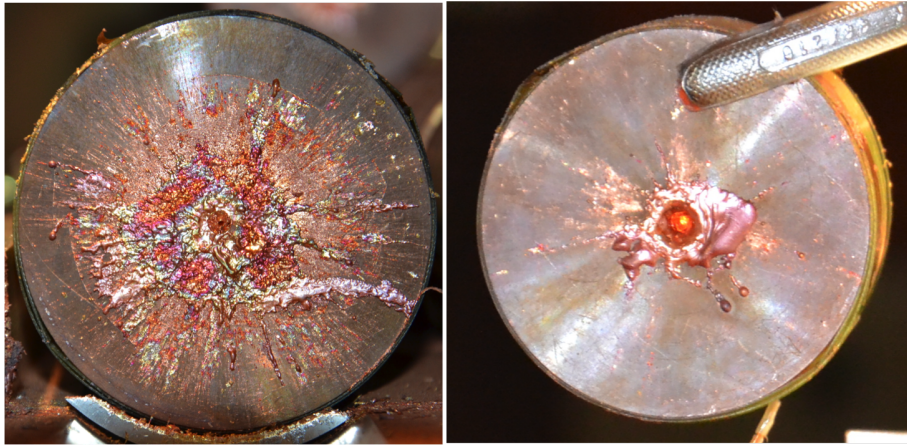


Fig. 6.10: Second cylinder of target 3. On the front face (left) the solidified copper splashes from cylinder 1 are clearly visible. The back shows the hole generated by the beam. The copper on the beam axis was in gaseous state. The highest energy deposition was located in this cylinder. The coloring is real.



Fig. 6.11: Front (left) and back (right) face of the third cylinder. Molten copper is leaking out of the hole, solidified splashes are clearly visible.

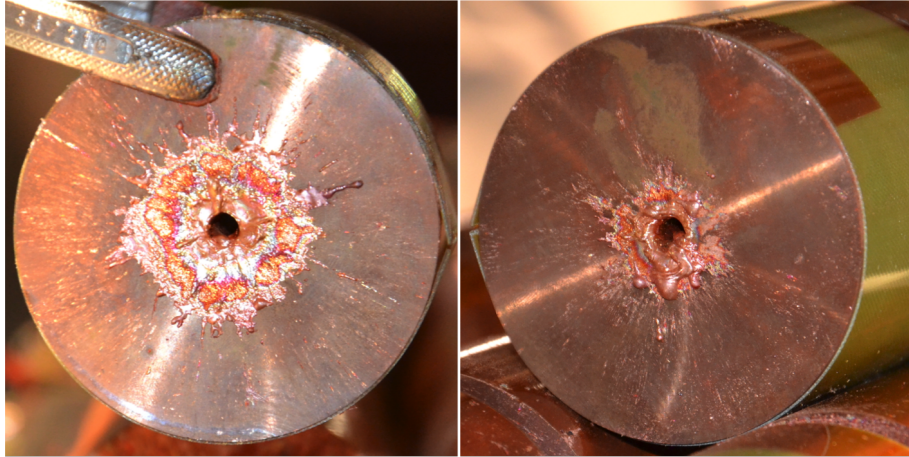


Fig. 6.12: Front (left) and back (right) face of the fourth cylinder of target 3. The hole-diameter and the surface covered by the solidified splashes is getting smaller.



Fig. 6.13: Front (left) and back (right) of the fifth cylinder of target 3. The hole diameter is getting smaller as the energy deposition decreases.

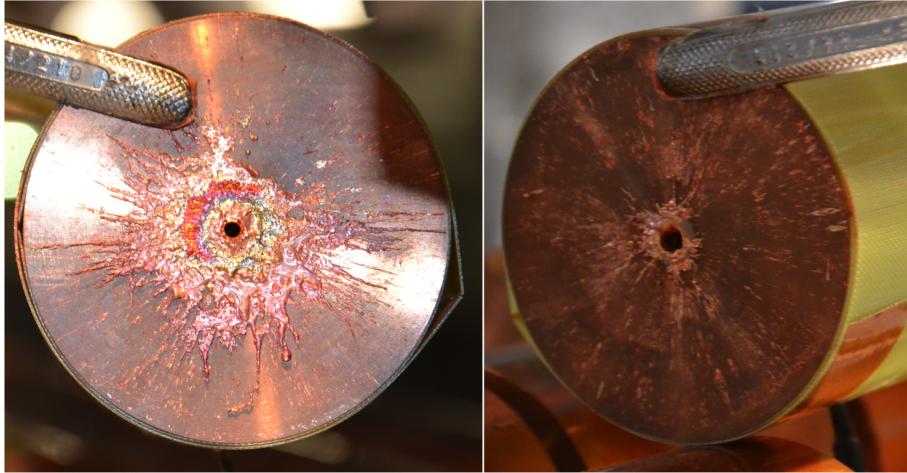


Fig. 6.14: Front (left) and back (right) of the sixth cylinder of target 3. The hole diameter is again decreased compared to the previous cylinder.

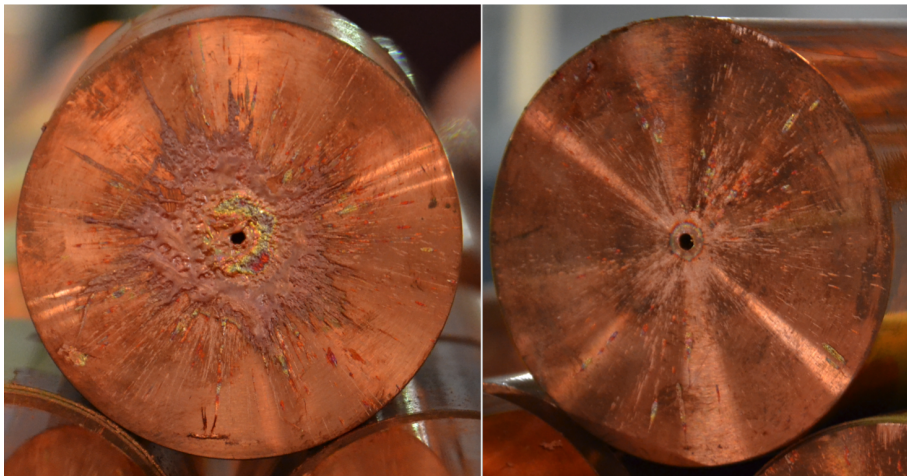


Fig. 6.15: Front (left) and back (right) of the seventh cylinder of target 3. Further decrease of the hole-diameter.

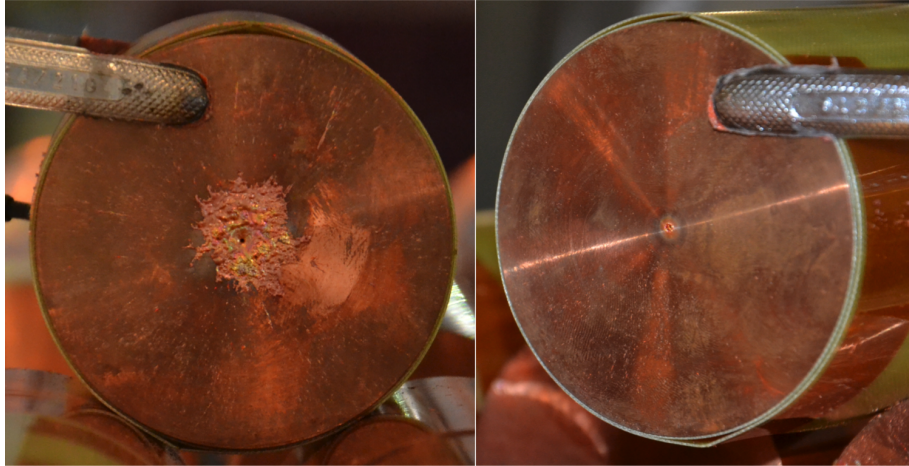


Fig. 6.16: Front (left) and back (right) of the eighth cylinder of target 3. Hole-diameter and covered surface by solidified splashes significantly decreased.



Fig. 6.17: Front (left) and back (right) of the ninth cylinder of target 3. Solidified splashes on the front plate are clearly visible. On the back face a decoloring of the copper on beam axis is visible. No hole detectable from visual inspection.

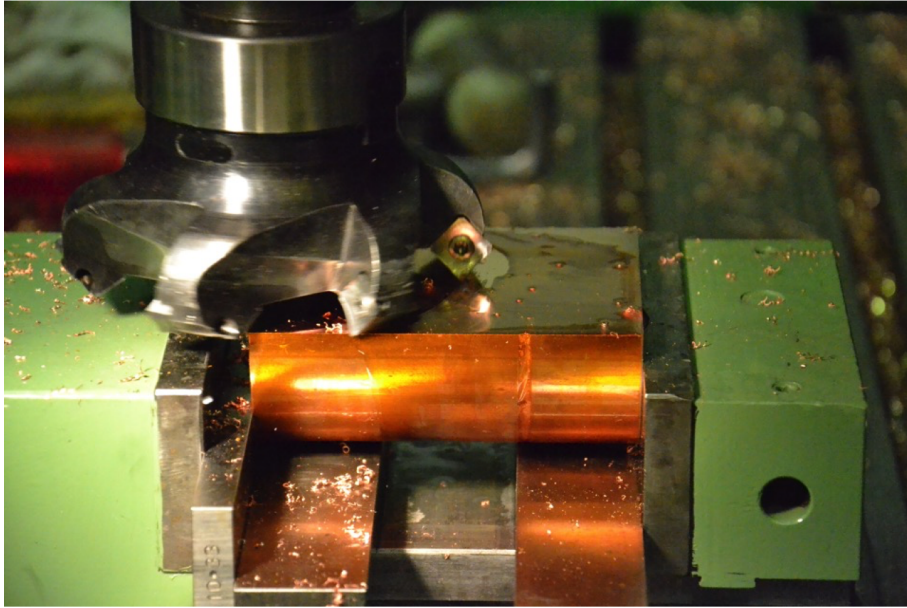


Fig. 6.18: Picture taken during the milling process. The rotating milling cutter is moving from the left to the right over the half of the copper cylinder.

microscopic analysis of the selected cylinders was carried out in order to inspect the region damaged by the beam. In Figure 6.20 different sections of the first cylinder of Target 3 are presented. Figure 6.20 (a) shows the first third, whereas Figure 6.20 (b)-(c) represent the middle third and the last third of the cylinder. Figure 6.20 (a) shows that micro-cavities have been formed in the first 2.3 cm. Beyond 2.3 cm the cone shaped hole starts.

Figures 6.20 (b) and 6.20 (c) show that the hole continues along the cylinder axis until the end. In addition solidification of liquefied copper is clearly visible. In Figure 6.21 a zoom into the beam entrance region is given. It shows the first few mm, the bulge at the beginning was made during the ejection of the solid copper to the aluminum end caps. This is in full agreement with previous simulations [42].

The following pictures 6.22 to 6.25 show three-dimensional high-resolution pictures of the hole drilled by the beam in the first cylinder of Target 3. The region between $z = 2.4 - 2.6$ cm (see Figure 6.22) and the region between $z = 9.3 - 10$ cm (see Figure 6.23) is shown. The coloring is real. Detailed analysis by PC made depth coloring and analysis of the three-dimensional pictures showed that the radius of the hole in Figure 6.24 is $327 \mu\text{m}$, whereas it is 2.3 mm at the end of the cylinder at $z = 10$ cm (see Figure 6.25).

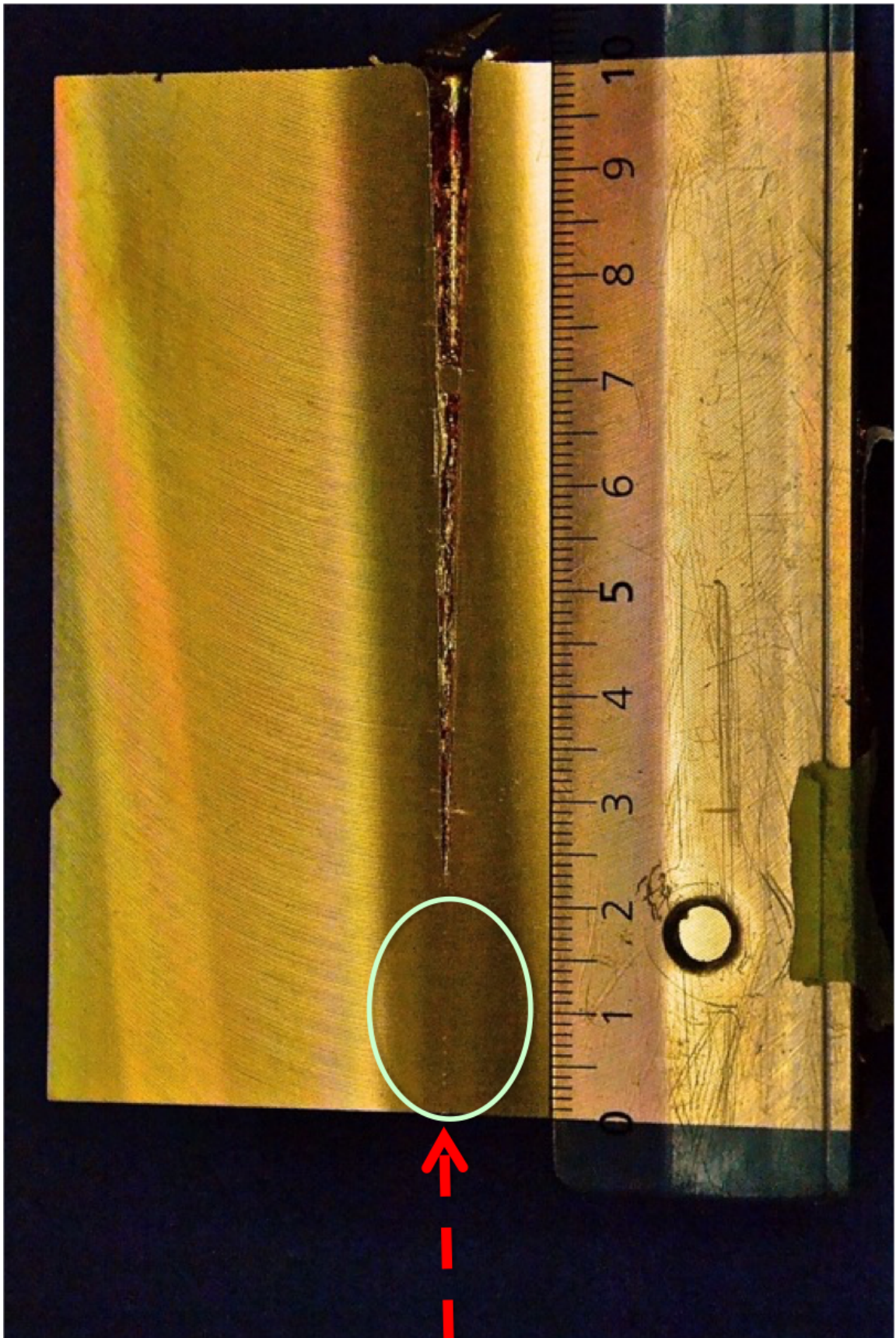


Fig. 6.19: Surface picture of cylinder 1 of target 3 after cutting it longitudinally. In the first 2.3 cm micro cavities are observed, further downstream a cone shaped hole is clearly visible. The entrance of the beam is marked with the red arrow.

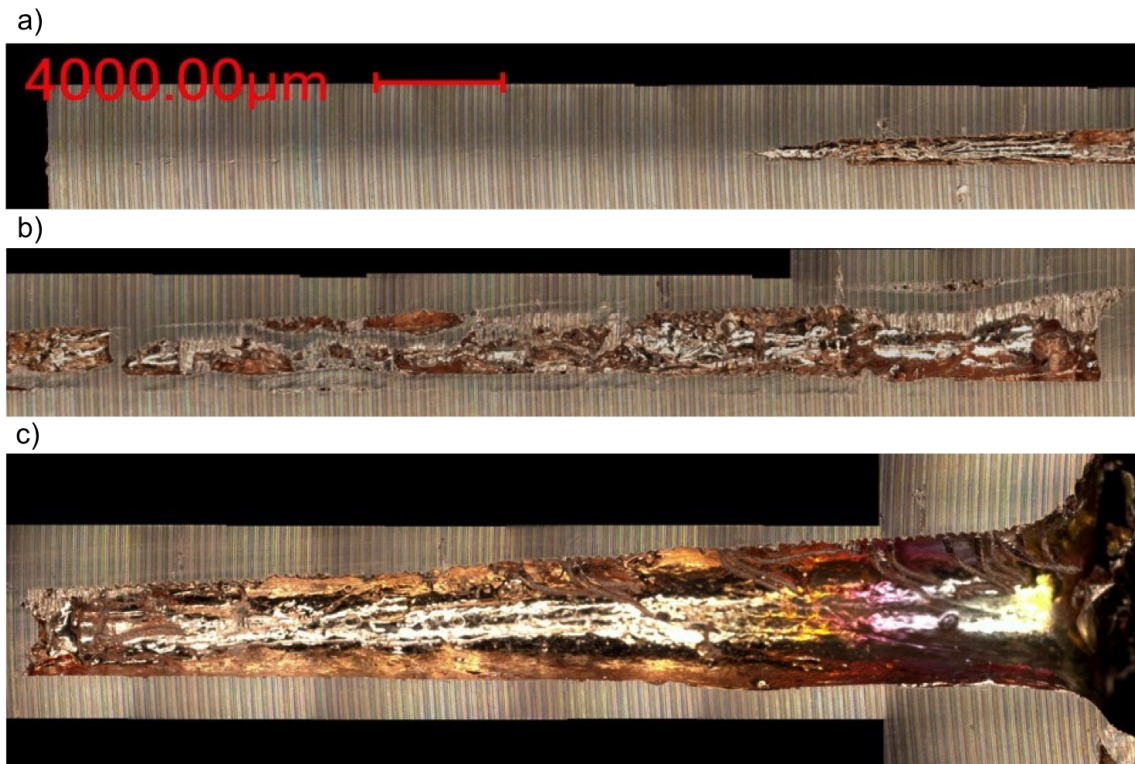


Fig. 6.20: Target 3, Cylinder 1. Microscopic analysis of the hole generated by the beam. a) first, b) second and c) last third of the first cylinder.

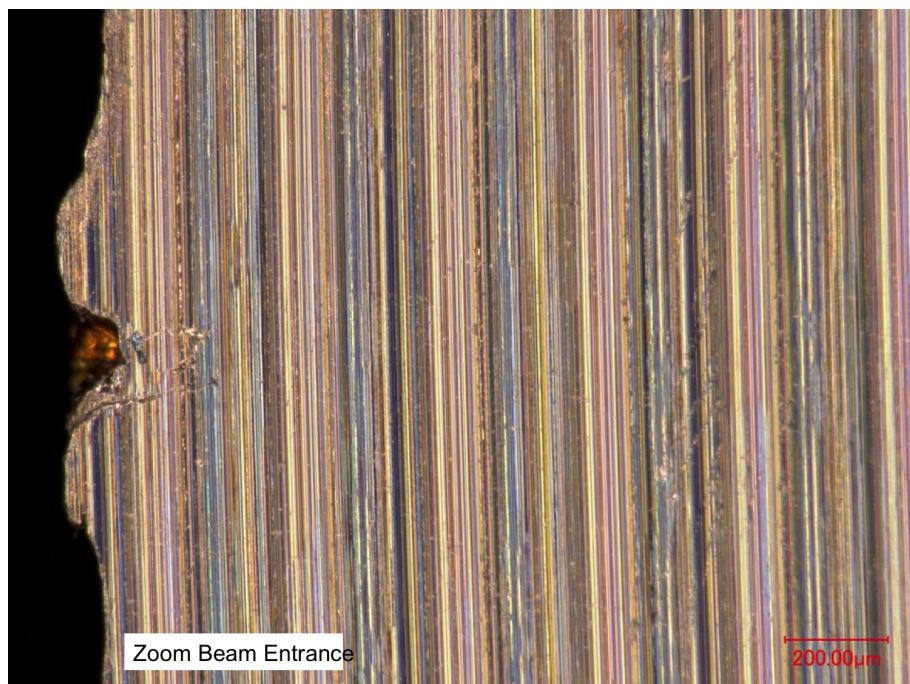


Fig. 6.21: Zoom into the beam entrance area of the first cylinder of target 3.



Fig. 6.22: 3D high-resolution picture of hole drilled by the beam in the first cylinder of Target 3. The region between $z = 2.4 - 2.6$ cm is shown with a magnification of 200x.

Figure 6.26 shows a micro cavity found at the end of the damaged region at $z = 85$ cm in target 3. This micro-cavity is located on beam axis. The same kind of micro cavities has been found in the last irradiated cylinder of the other targets; therefore the length of the damaged region was determined by determining the last visible micro-cavity.

6.4 Final result

In the microscopic analysis of the experimental results the length of the damaged region was determined by determining the last visible micro-cavity. The results are listed in Table 6.2.

Tab. 6.2: Final experimental results of the hydrodynamic tunneling experiment. The length of the damaged region was determined by determining the last visible micro-cavity.

Target	Length of damaged region (cm)
1	58
2	79.5
3	85



Fig. 6.23: 3D high-resolution picture of hole drilled by the beam in the first cylinder of Target 3. The region between 9.3 - 10 cm is shown with a magnification of 50 x. The coloring is real.

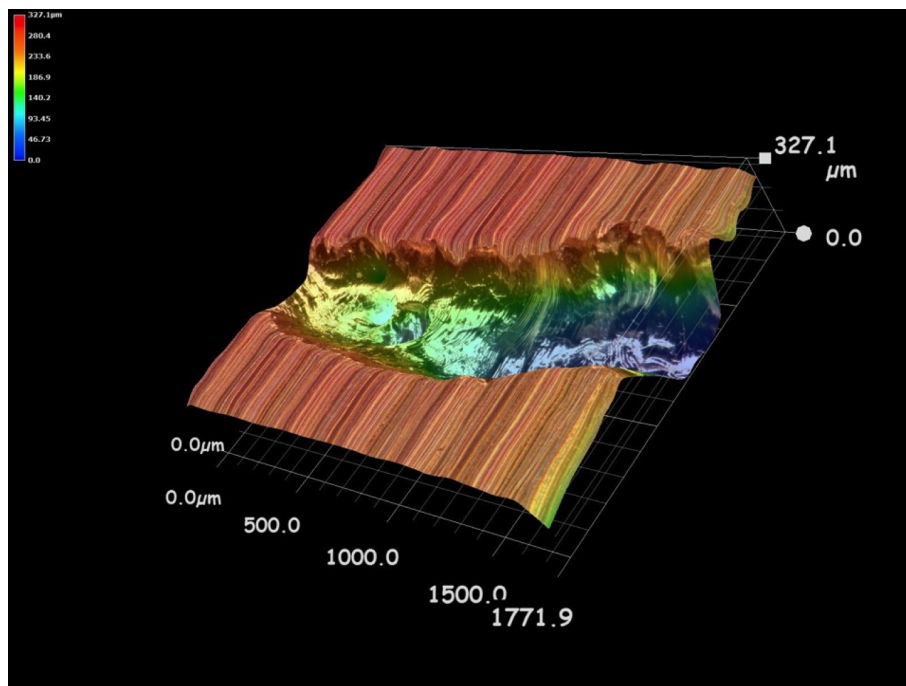


Fig. 6.24: 3D high-resolution picture with PC-made depth coloring of hole drilled by the beam in the first cylinder of Target 3. The region between $z = 2.4 - 2.6$ cm is shown with a magnification of 200 x. The hole radius was found to be $327 \mu\text{m}$.

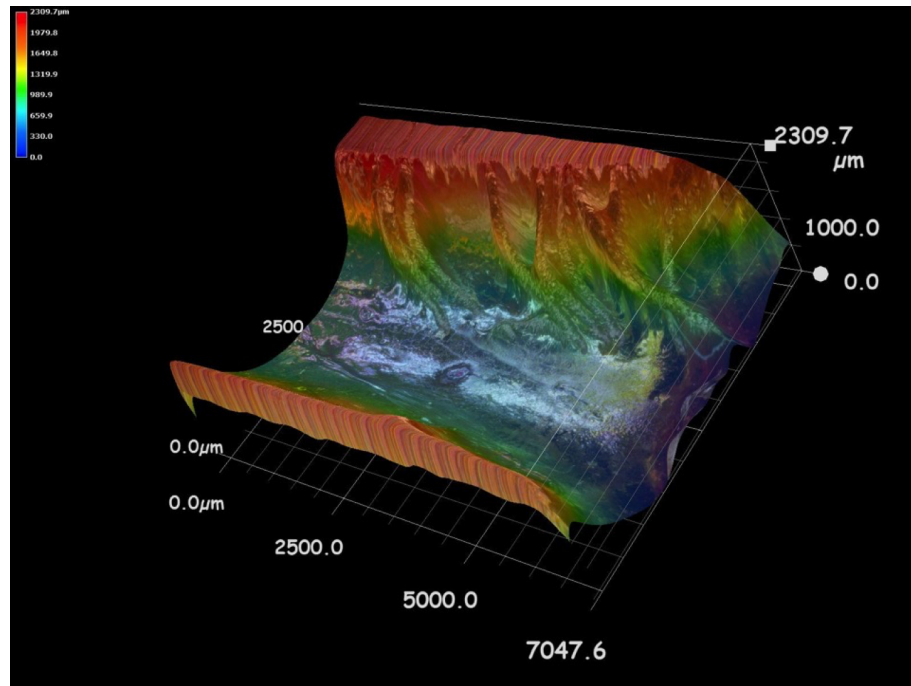


Fig. 6.25: 3D high-resolution picture with PC-made depth coloring of hole drilled by the beam in the first cylinder of Target 3. The region between 9.3 - 10 cm is shown with a magnification of 50x. The hole radius was found to be 2.3 mm.

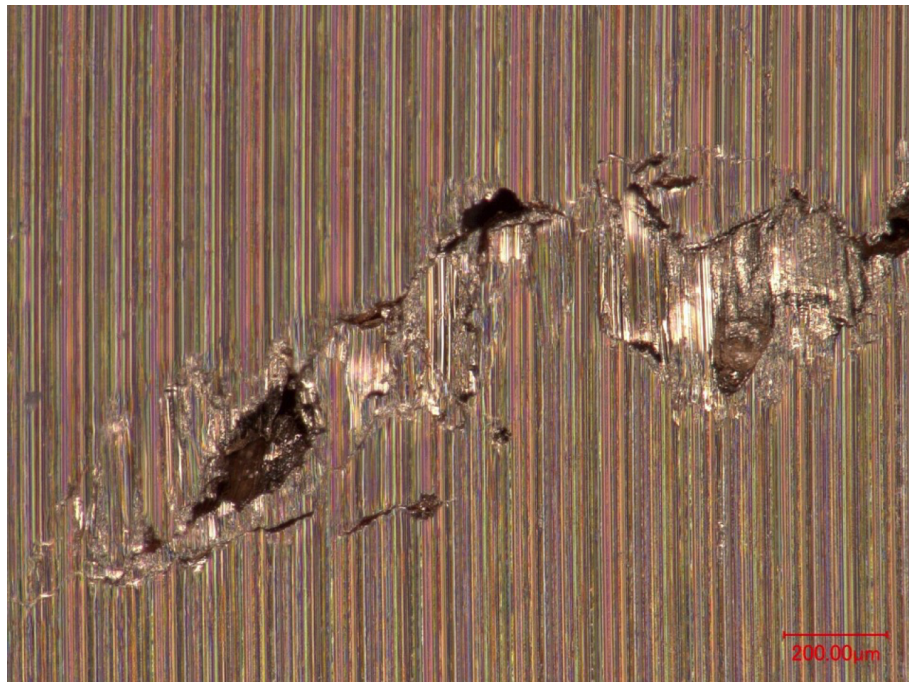


Fig. 6.26: Micro-Cavity at $z = 85$ cm in Target 3. The area is located on the beam axis with a surface of ~ 1.5 mm².

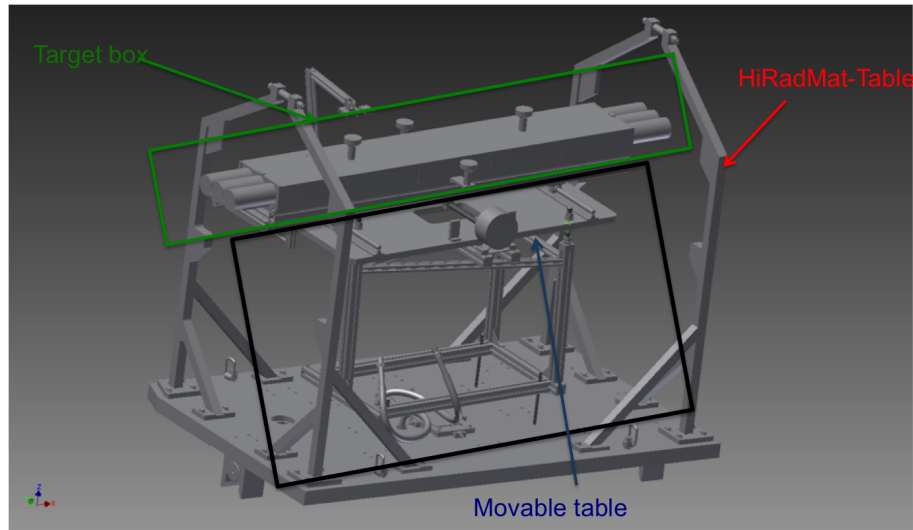


Fig. 6.27: Target assembly with the target box storing the copper cylinders, placed on the movable table, which is fixed on the HiRadMat table.

6.5 Removal of the target

In February 2015 it was decided to remove the target, including target box, movable table and the HiRadMat-table on which the setup was installed from the cool-down area of the HiRadMat-tunnel (so-called TNC). This section gives an overview on this action. The target assembly with target box, storing the copper cylinders, the movable table and the HiRadmat table is shown in Figure 6.27.

The activation of the closed target aluminum box was found to be between 14 and 27 $\mu\text{Sv/h}$. The activation of the copper cylinders is higher. The experimental setup shows a high risk of contamination, as molten copper splashes and activated dust can fall on the ground, contaminating the area. Therefore the full area had to be secured with plastic foil. The top cover was lifted to take out the last irradiated cylinder of each experiment. Additionally pictures of the front and back plate of each cylinder were taken. In the scope of the target opening, the end-caps were removed and replaced by aluminum plates. These end-caps were declared as radioactive waste. Afterwards the target box was closed again and the table was moved remotely from the cool-down area to the entrance of the HiRadMat-tunnel (TJ7). In TJ7 the full table had to be cleaned with ALCATUM, a decontaminating alcalin, to get rid of the contamination risk. Wipe test were performed after cleaning. The results shows, that the risk of contamination can be neglected, as long as the target box stays closed. The target assembly was then lifted up to the surface lab of BA7. In the lab the target box was separated from the movable table and the HiRadMat table. Afterwards the target box was placed in a double plastic foil and moved to the radioactive storage. The dose rate at 10 cm distance from the target box is 10 $\mu\text{Sv/h}$ (February 2015). Pictures of the different steps can be found in Figures 6.28 to 6.30.

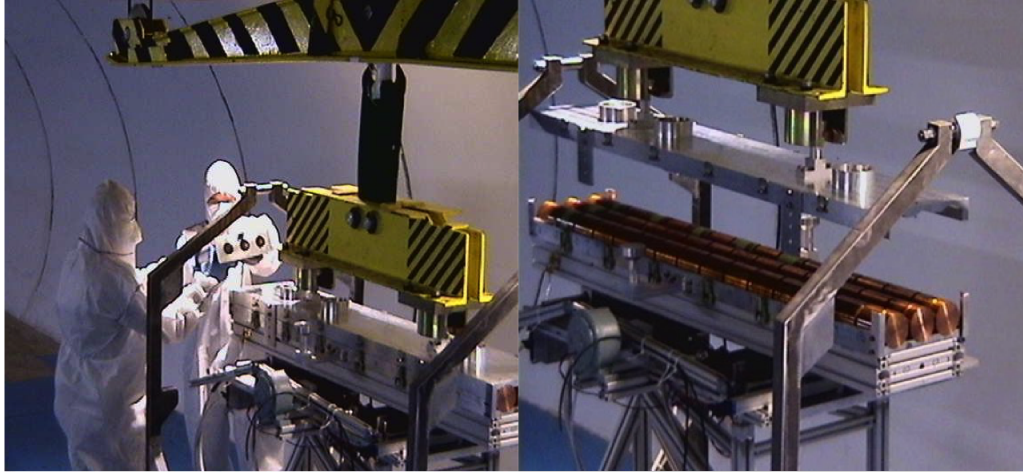


Fig. 6.28: Removal of the end caps (left) and lifting up the top cover of the target box (right).

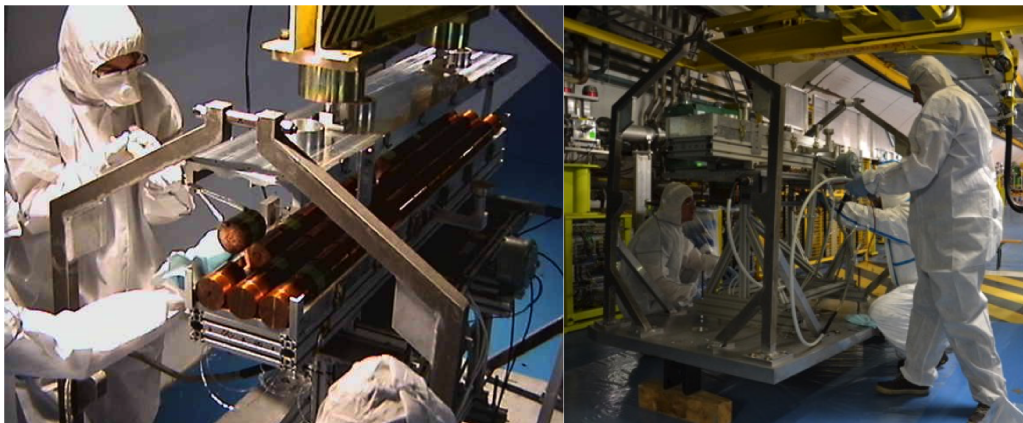


Fig. 6.29: Taking pictures of the front and back surface of each cylinder (left), cleaning the target assembly in TJ7 (right).

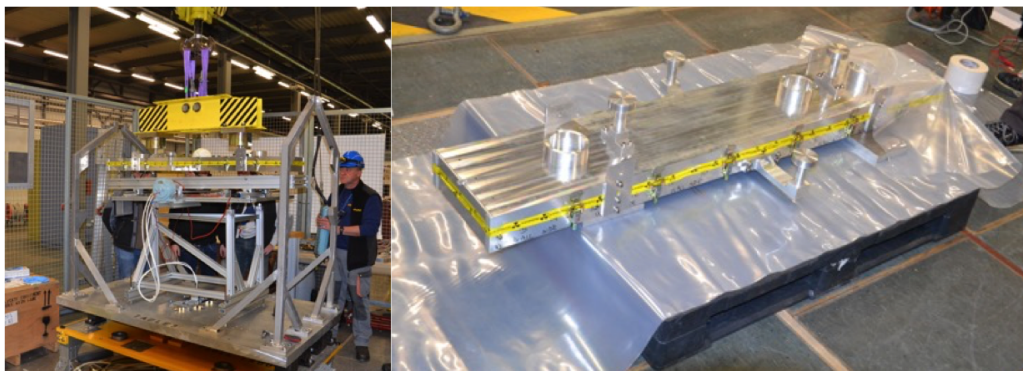


Fig. 6.30: Separation of the target assembly in the surface lab (left), target box on a pallet before wrapping in double plastic foil (right).

6.6 *Future work - Further analysis of irradiated copper cylinders*

The copper cylinders will be further examined to determine molten and re-solidified and solid parts of the material. As this was not directly visible during the microscopic analysis due to the domination of the milling machine traces, the samples have to be electro-polished. First experiments with non-irradiated samples showed that after a few hours of electro-polishing treatment these traces were sufficiently removed and the crystal structure was observable with a microscope. Further investigations with the irradiated samples, in accordance with radio-protection will follow.

7. SIMULATIONS WITH EXPERIMENTAL BEAM PARAMETERS

Previous theoretical work on beam-target heating has shown that in case of a bunched particle beam, like the one delivered by the LHC, energy deposited in the target by the protons delivered in the first few tens of bunches and the proton shower, causes strong heating of the solid material that leads to substantial increase in the temperature. The heated material undergoes phase transitions including liquification, evaporation and even conversion into weakly ionized strongly coupled plasma. The high temperature in the absorption zone generates a high pressure that launches a radially outgoing shock wave which causes substantial density reduction on the beam axis. As a consequence, the protons that are delivered in the subsequent bunches, penetrate much deeper into the target, the so-called hydrodynamic tunneling [28], [29]. This will lead to a significant lengthening of the projectile range. This phenomenon therefore has very important influence on the machine protection system design.

In the design phase of the experiment, described in chapter 6, (2011) simulations were performed to get an estimate of the beam penetration depth [30], [31], [32]. To benchmark the simulation code and verify the hydrodynamic tunneling process the experiment was re-simulated with the beam parameters used during the experimental phase. This chapter motivates the usage of the combined simulations with FLUKA and BIG2, in addition it will present and discuss the simulation process, the results and the comparison to the experimental results.

7.1 Motivation

The specific energy deposition along the target axis calculated with FLUKA for target 1 and target 3 is shown in Figure 7.1. This simulation uses the assumption, that all the beam particles hit instantaneously the target, excluding hydrodynamic simulations with BIG2. Therefore, these simulations are called static simulations in the following. The red and blue-dashed lines indicate the amount of the specific energy needed to melt and to evaporate the copper, respectively. For the first experiment using 144 bunches and $\sigma = 2$ mm, the beam deposits sufficient specific energy between $L = 6$ -47 cm, to melt the target. The energy deposition is not high enough to evaporate the copper. For the third experiment with 144 bunches and $\sigma = 0.2$ mm, the simulations show that the material is melted or evaporated along the axis up to $L = 67$ cm. A comparison between these simulations and the experimental measurements for the three experiments is given in Table 7.1. It shows a significant discrepancy between the experimental measurements and the simulations based on

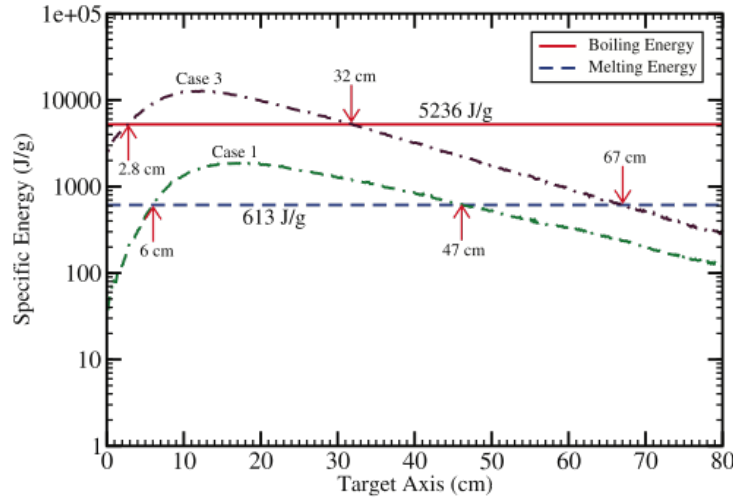


Fig. 7.1: Specific energy deposition along the target axis, evaluated with static FLUKA simulations. The energy deposition for experiment 1 (Case 1) and experiment 3 (Case 3) is shown. The blue-dashed line indicates the specific energy needed to melt copper, the red line indicates the specific energy needed to boil copper. For experiment 1 the copper is molten between 6 and 47 cm. In case of experiment 3 the molten zone is between beginning of the target and 67 cm.

a static approximation. The difference between static simulations and measured length of the molten zone is between 11 cm (Target 1) and 17 cm (Target 3). In order to get a more precise result detailed numerical simulations have been carried out running the energy deposition code FLUKA and the 2D hydrodynamic code BIG2 iteratively. In addition this experiment was used as a benchmark for the FLUKA - BIG2 simulation routine.

Tab. 7.1: Comparison between length of the molten zone, evaluated with static FLUKA simulation and the measured length of the hole. The difference is caused by the hydrodynamic tunneling effect.

Target	Simulated length of molten zone (cm)	Measured length of molten zone (cm)
1	47	58
2	64	79.5
3	68	85

7.2 Geometry, parameters and simulation routine

For the simplicity of simulations a single solid copper cylindrical target with 150 cm length, 4 cm radius and a density of 8.93 g/cm^3 was considered. The 1 cm gaps between neighboring cylinders, as in the experiment, do not affect the energy deposition and the hydrodynamic processes. These processes are much stronger in the

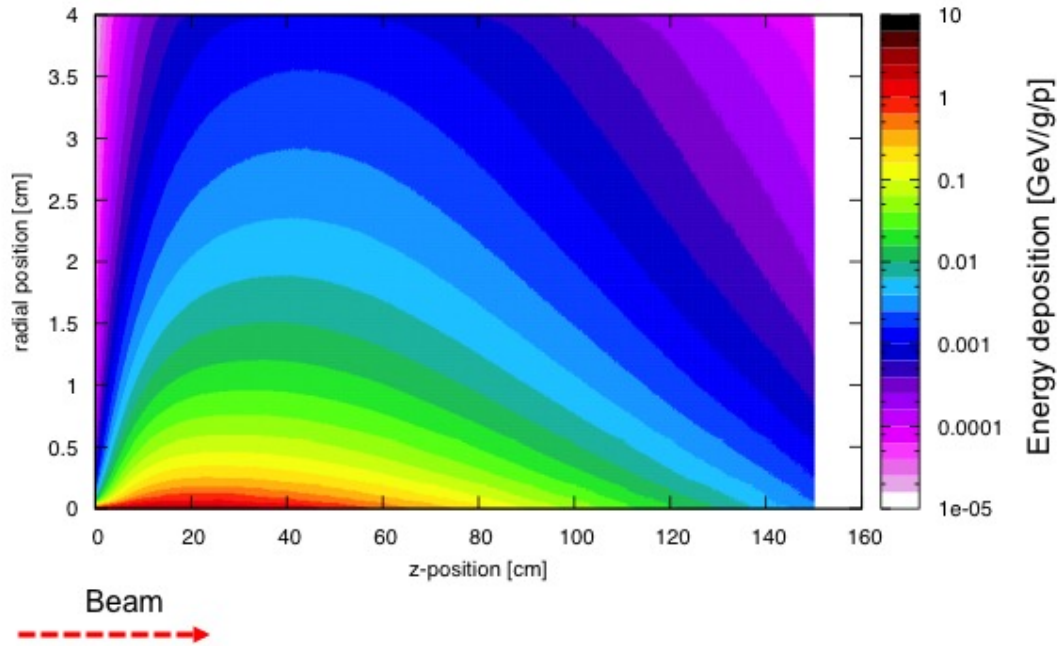


Fig. 7.2: Energy deposition map in GeV/g/p calculated by FLUKA. It shows the energy deposition after irradiation with 50 bunches. The beam is coming from the left side.

radial than in the axial direction in this type of experiment [42]. Therefore, these gaps were not included in the simulation model. The simulations have been carried out using FLUKA to evaluate the energy deposition due to a proton beam perpendicular impacting on the front plate of the first cylinder with the beam parameters from Table 6.1. The energy deposition is obtained using a two-dimensional Gaussian beam distribution (horizontal and vertical $\sigma = 0.2$ mm). 200.000 particles were simulated, which reduced the statistical error of the FLUKA simulation to less than 1%. The energy deposition map of the target in GeV/g/p with a resolution of 0.15 cm in longitudinal direction and 0.01 cm in radial direction was then converted to a BIG2 input file. This map was then used by BIG2 to calculate the density decrease in the target. To avoid instabilities of the simulation code and density oscillations, which would be unphysical, the maximum allowed density reduction for one iteration was 15%. This is equivalent to the changes in the target within 700 ns. A picture of the energy deposition map after 50 bunches delivered is shown in Figure 7.2. The output of BIG2, a density map, had to be converted into a FLUKA input format. As FLUKA and BIG2 use different geometries and meshes a conversion is required. For this conversion a Python script was used.

A plot of the density distribution after 700 ns (14 bunches) is shown in Figure 7.3. The density in the beam heated region is already reduced to 7.6 g/cm^3 from 8.96 g/cm^3 in solid copper. Note, that only the inner 3 mm (radial) of the target are plotted.

Due to the axial symmetry of the problem the data is given in cylindrical coordinates with $\theta = 0$. The target is arranged in 3 regions with different meshes,

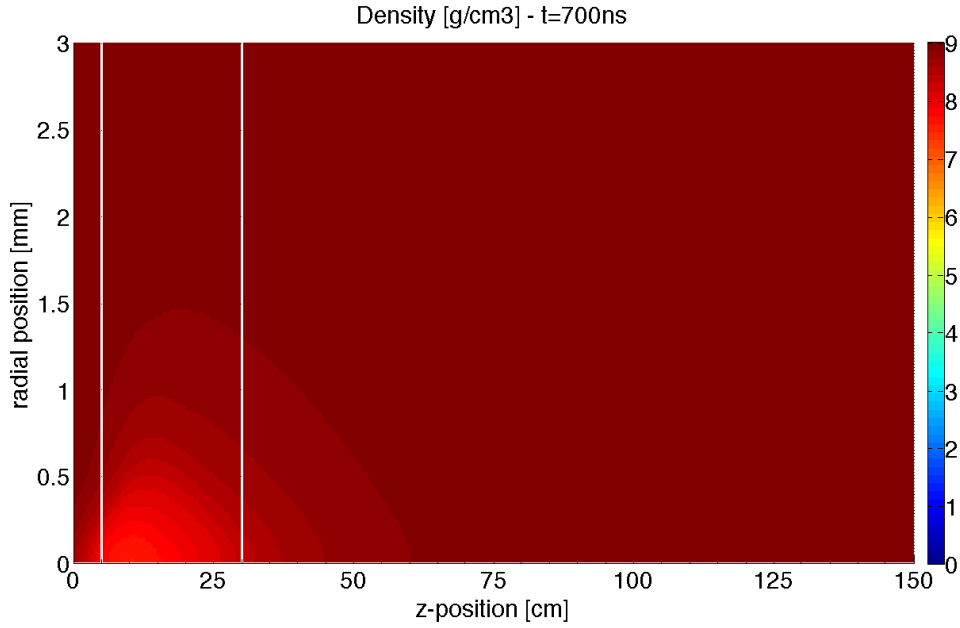


Fig. 7.3: Density map after 700 ns. The density in the beam heated region is reduced to 7.6 g/cm^3 . It is to be noted, that only the inner 3 mm are shown. The white lines indicates the regions with different meshes.

this is indicated in Figure 7.3 by the white lines. Table 7.2 shows the 3 regions and their respective bin sizes. The density data from each region is re-arranged into an individual matrix. Afterwards, all individual matrices are assembled together. Region 1 is the middle part from $z = 5.2 - 29.8 \text{ cm}$ with a resolution of $0.4 \text{ cm} \times 0.002 \text{ cm}$ (longitudinal x radial). Region 2 is the beginning of the target ($z = 0.2 - 5.0 \text{ cm}$) with a resolution of $0.4 \text{ cm} \times 0.004 \text{ cm}$. The last part of the target (Region 3) from $z = 30.2 - 150 \text{ cm}$ with the same resolution as Region 1.

Tab. 7.2: Density data matrix scheme of the target with the number of bins in longitudinal and radial direction.

	Region 1	Region 2	Region 3
Number of bins (l x r)	62 x 2000	11 x 1000	300 x 2000

In the next step the data has to be interpolated into a common mesh as the data points from BIG2 might not correspond to the geometry mesh. The interpolation is done using the `scipy.interpolate` function from the `scipy` package. In the last step neighboring points where the density change is limited have to be grouped [43]. Within these regions, the accumulated gradient in z and r is limited to a certain value. This value is calculated in a way that the total number of regions does not exceed 10000. This value is given by the maximum number of regions which can be handled by FLUKA. The highest density gradient and therefore the highest region density is given around the beam axis in the strong heated region. The FLUKA regions are build, using combinational geometry, by combining cylinders with different radii with planes at different longitudinal positions (x - y -planes). The boundaries of the

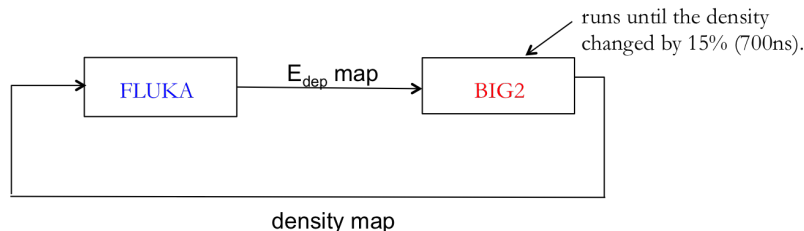


Fig. 7.4: Schematic of the iterative simulation process using FLUKA and BIG2.

regions in the radial and longitudinal direction (cylinders) are determined in that manner, that the density-gradient does not exceed a certain value. To reduce the number of regions even further, which will reduce the complexity of the given system, regions with similar densities has to be combined.

The script also assigns the correct material properties (A, Z) to the materials, sets the beam parameters (particle type, beam size, beam energy) and simulation parameters (start position, simulation type, name of the files). This new input file with the modified density after $\Delta t = 700$ ns is then used to calculate the energy deposition for the subsequent bunches. In this manner the two codes are applied iteratively to the problem of beam-matter interaction. For this experiment this routine was repeated 12 times. One step took approximately one week. A schematics of the simulation process is given in Figure 7.4 The simulations have been performed only for target 2 and target 3, in which the smaller focal spot size with $\sigma = 0.2$ mm was used.

7.3 Simulation results

Figure 7.5(a) shows the energy deposition distribution per proton (440 GeV) in units GeV/g assuming a solid material density. It can be seen that the particle showers range is about 65 cm into the target. The peak energy deposition is ~ 3.75 GeV/g/p at $z = 12$ cm. The FLUKA calculations also shows that approximately 40 % of the beam energy escapes while 60 % is absorbed in the target. The total energy in a single proton bunch of 1.15×10^{11} p is 10.56 kJ which means every bunch deposited 6.25 kJ in the target. Figure 7.5(b) shows the energy deposition data obtained with FLUKA, but using the density distribution provided by BIG2 at $t = 2.73 \mu\text{s}$ (irradiation with 50 bunches). The energy deposition distribution has been modified with a broadening of the energy peak that indicates deeper penetration of the protons and the shower into the target. The maximum value of the energy deposition has been reduced to around 2.4 GeV/g/p.

The energy deposition distribution plotted in Figure 7.5(c) has been calculated by using the density distribution obtained from BIG2 at $t = 4.75 \mu\text{s}$ (irradiation with 86 bunches). It shows a significant broadening of the energy peak while the maximum value of the energy deposition becomes about 1.6 GeV/g/p. This indicates an even longer penetration of the particle shower in the target. Figure 7.5(d) presents the energy deposition distribution at $t = 6.75 \mu\text{s}$ (irradiation with 122 bunches). Note that the distribution has a double peak behavior and the second peak is higher than

the first one. This is due to the fact that the density in the initially irradiated region of the target has decreased to such an extent that it contributes little to the beam stopping and the protons and the shower particles penetrate much deeper into the target, thereby generating the second peak in the energy distribution.

In Figure 7.6(a) the specific energy deposition in the target at $t = 5800$ ns, the time when the target was irradiated with 108 bunches, is presented. This corresponds to the status after irradiation of experiment 2. By this time, a maximum specific energy of 5.7 kJ/g has been deposited at the target center which gives rise to strong heating that leads to a maximum temperature of about 7900 K in the beam heated zone (see Figure 7.6(b)). The corresponding pressure distribution is presented in Figure 7.6(c) which shows a maximum pressure of 1.5 GPa and the high pressure region has spread in large part of the target due to the shock wave propagation in the radial direction. As the target heating is a localized effect only the inner 1 cm radial part of the specific energy and the temperature distributions are plotted. The pressure wave is a global phenomenon traveling throughout the full target. It is therefore necessary to show the pressure distribution in the entire target. The corresponding density distribution is depicted in Figure 7.6(d) which shows that the density at the target center has been reduced to 1.67 g/cm^3 which is about 19% of the solid copper density. The direct heating of the material has extended to about 80 cm in the longitudinal direction due to the hydrodynamic tunneling effect. The pressure wave, on the other hand, has traveled along almost the entire cylinder length (see Figure 7.6(c)).

In Figure 7.7(a) to d) the same variables as in Figure 7.6(a) - (d) are shown, but at $t = 7850$ ns, after the irradiation with 144 proton bunches which represents target 3. Figure 7.7(a) shows that a maximum specific energy of 6.3 kJ/g has been deposited at the target center that leads to a max. temperature of about 7600 K (see Figure 7.7(b)). This is lower than in Figure 7.6(b) due to the cooling caused by material expansion resulting from the hydrodynamic effects. It is seen in Figure 7.7(c) that the pressure waves have traveled throughout the target in the radial as well as in the longitudinal direction. The radial waves have already been reflected at the target surface whereas the high pressure region has also been extended to the opposite face of the target. The corresponding density distribution is presented in Figure 7.7(d) showing that the density at the target center has been reduced to 0.85 g/cm^3 , 10% of the solid copper density.

In Figure 7.8(a), the temperature profiles along the target axis ($r = 0$) at four different times, after irradiation with 36, 72, 108, and 144 bunches, is depicted. The flat region on the right part of each curve represents a zone where the material starts melting. It can be clearly seen that the melting zone propagates with increasing bunch number towards the right due to the deeper penetration of the protons resulting from the hydrodynamic tunneling. The reduction in the temperature in the low density region above the point $L = 25$ cm is shown in the curve corresponding to 144 bunches. Figure 7.8(b) shows the same four profiles as Figure 7.8(a) along the target length, but at $r = 1$ mm. It can be seen that the specific energy is high enough to melt the material at this distance from the axis and a maximum temperature of 5000 K is achieved around the region at $L = 25$ cm after irradiation with 144 proton

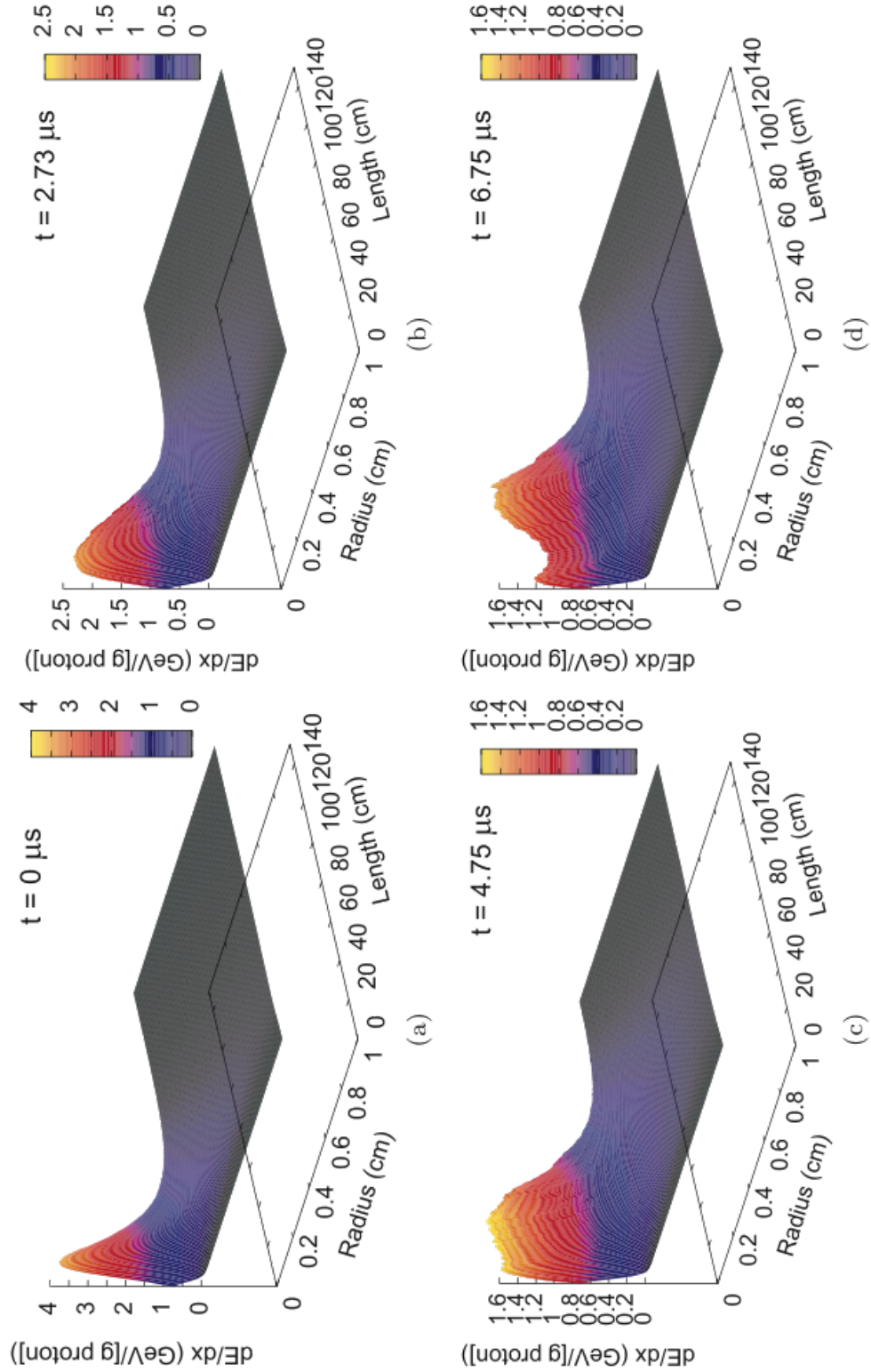


Fig. 7.5: Energy deposition in GeV/g of a proton calculated using FLUKA. (a) - (d) show the energy deposition in target 3 at $t = 0 \mu\text{s}$, $t = 2.73 \mu\text{s}$, $t = 4.75 \mu\text{s}$, $t = 6.75 \mu\text{s}$.

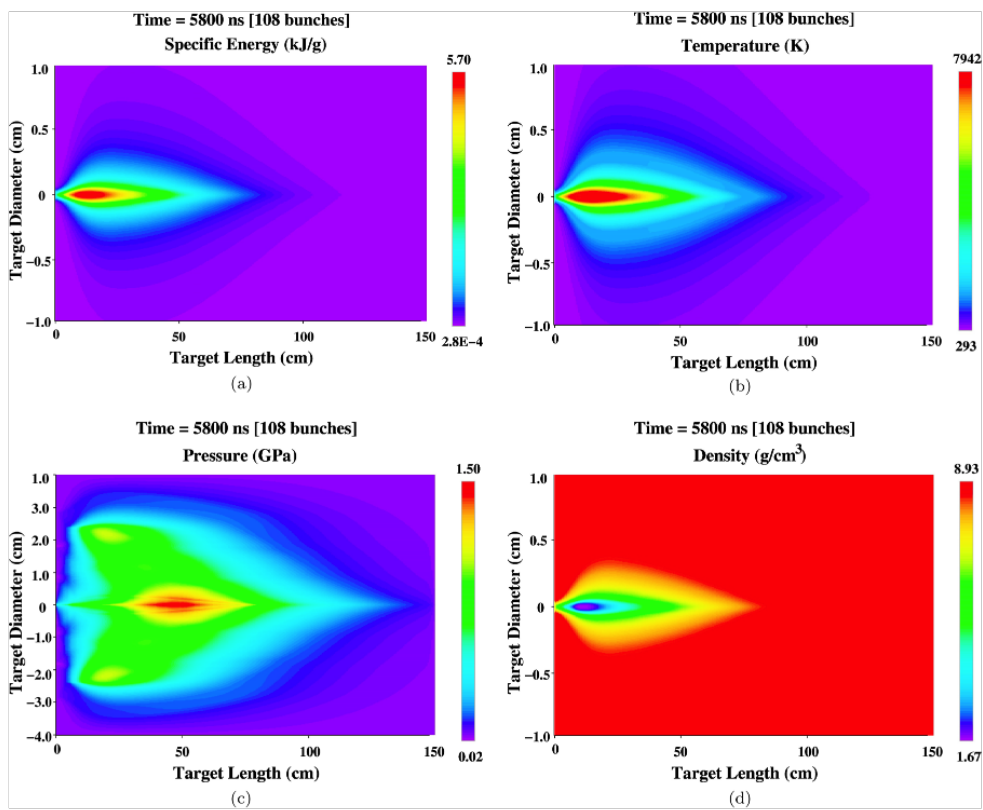


Fig. 7.6: Specific energy, Temperature, Pressure and Density after irradiation with 108 bunches (target 2).

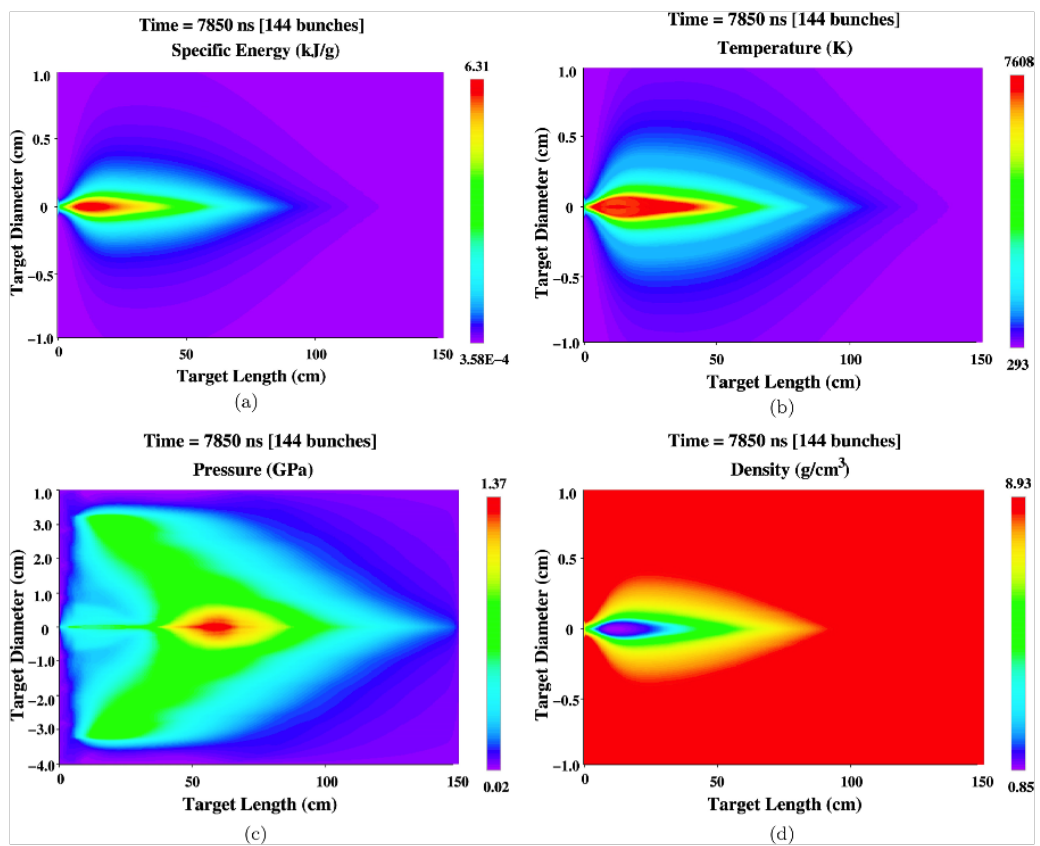


Fig. 7.7: Specific energy, Temperature, Pressure and Density after irradiation with 144 bunches. This is the status of target 3 directly after the irradiation.

bunches. Figure 7.8(c) shows the same temperature profiles at $r = 2$ mm. It can be seen that even at this distance from the axis, the material is melted and heated to a maximum temperature of 2500 K after the irradiation with 144 proton bunches.

In Figure 7.9(a) the density profiles corresponding to the temperature profiles presented in Figure 7.8(a) is shown. The density is systematically reduced as more bunches deposit their energy and the minimum density becomes less than 1 g/cm^3 after the impact of 144 bunches. This shows serious damage to the target along the axis. Figure 7.9(b) shows the same density profiles at a radial position of $r = 1$ mm. Significant density reduction is also clearly visible in this region and the minimum density decreases to 5.5 g/cm^3 after the irradiation with 144 bunches. Figure 7.9(c) shows the density profiles at a radial position of $r = 2$ mm. Again, a noticeable density reduction can be observed in this region.

The above analysis of the simulation results shows that a significant part of the target undergoes phase transitions and enters into the regime of the HED state [84] of copper. In Figure 7.10 the phase state of the target at $t = 7850$ ns (irradiation with 144 bunches) is plotted. This corresponds to the conditions in target 3. Different phase states of copper are clearly visible. These include a melting phase, a compressed as well as an expanded hot liquid state, a two-phase liquid-gas state and a gaseous phase.

7.4 Comparison experimental and simulation results

Figure 7.11 shows the density and temperature along the axis at $t = 5800$ ns, after irradiation with 108 bunches on target 2. The flat part of the temperature curve represents the melting region and lies within $L = 75$ -80 cm which is equivalent to the RHS half of the eighth cylinder. The temperature curve also shows that the material along the axis up to 75 cm is liquefied or even evaporated, depending on the temperature. Liquefied material escapes from the left face of cylinder number 8 and collides with the melted or gaseous material ejected from the right face of cylinder number 7. As a result of this collision, the material is splashed vertically and is deposited at the inner surface of the target cover above the gap between cylinder number 7 and 8.

Figure 7.12 shows the same parameters as Figure 7.11 but for experiment 3. The copper is liquefied till $L = 85$ -90 cm. This corresponds to a beam stopping in cylinder 9. The damaged region was defined as the region where a melting of the material is possible. Therefore the damaged region according to the simulation is 80 cm for target 2 and 90 cm for target 3.

In the microscopic analysis of the experimental results the length of the damaged region was determined by determining the last visible micro-cavity. The last micro-cavity was found at $L = 79.5$ cm (target 2) and at $L = 85$ cm (target 3). The measured penetration length of the beam and the results from the hydrodynamic simulations using FLUKA and BIG2 for all targets are summarized in Table 7.3. Excellent agreement between hydrodynamic simulations and experimental results was found. This work has further deepened the understanding of hydrodynamic tunneling for the LHC beam and has validated the use of the BIG2 code for simulating this effect.

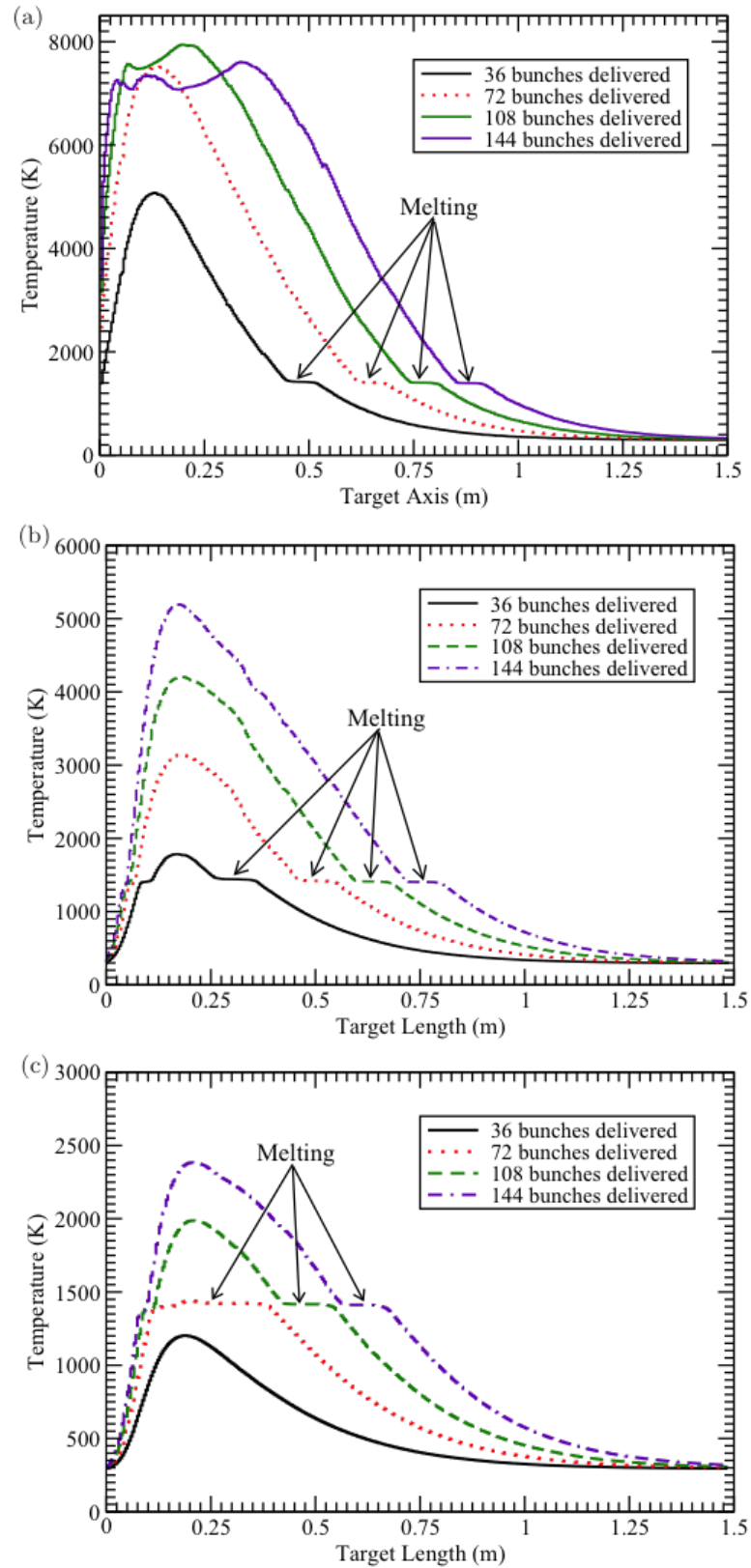


Fig. 7.8: Temperature along the target. (a) shows the status on beam axis, (b) at a radius of 1 mm (c) at a radius of 2 mm).

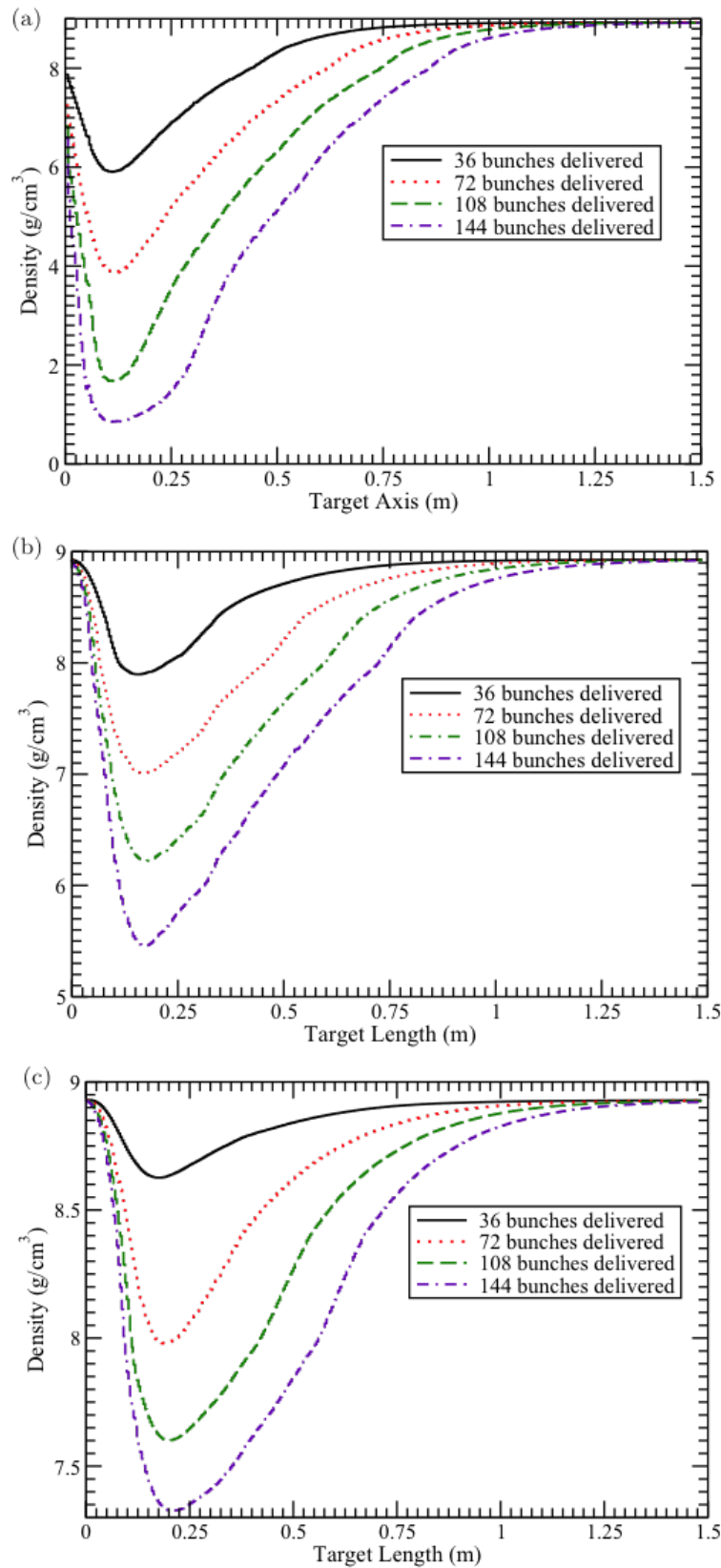


Fig. 7.9: Density along the target. (a) shows the status on beam axis, (b) at a radius of 1 mm (c) at a radius of 2 mm).

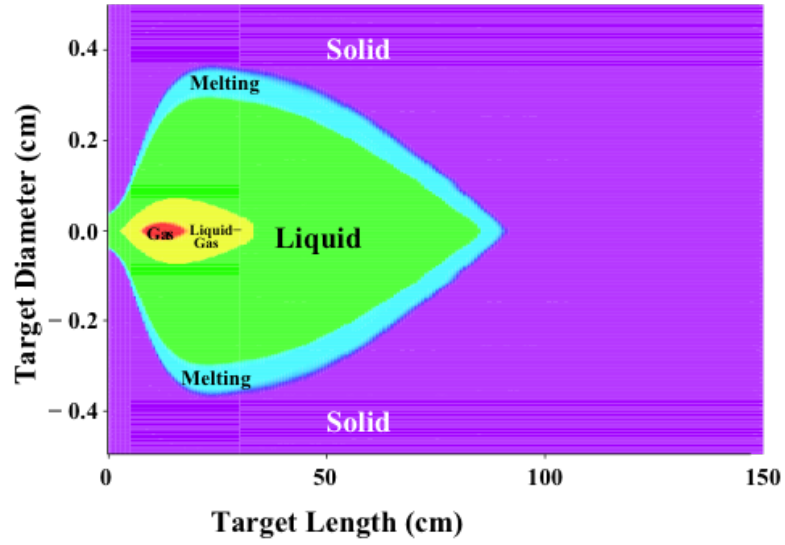


Fig. 7.10: Phase state of the target directly after the impact of 144 bunches.

The results verified the previous assumption for the penetration depth of the nominal LHC proton beam in copper of ~ 35 m.

Tab. 7.3: Simulation and experimental results for the three targets. No hydrodynamic simulation was performed for Target 1.

Target	Simulation results (cm)	Experimental results (cm)	Δ Exp. to sim. results (cm)
1	-	58	-
2	80	79.5	0.5
3	90	85	5

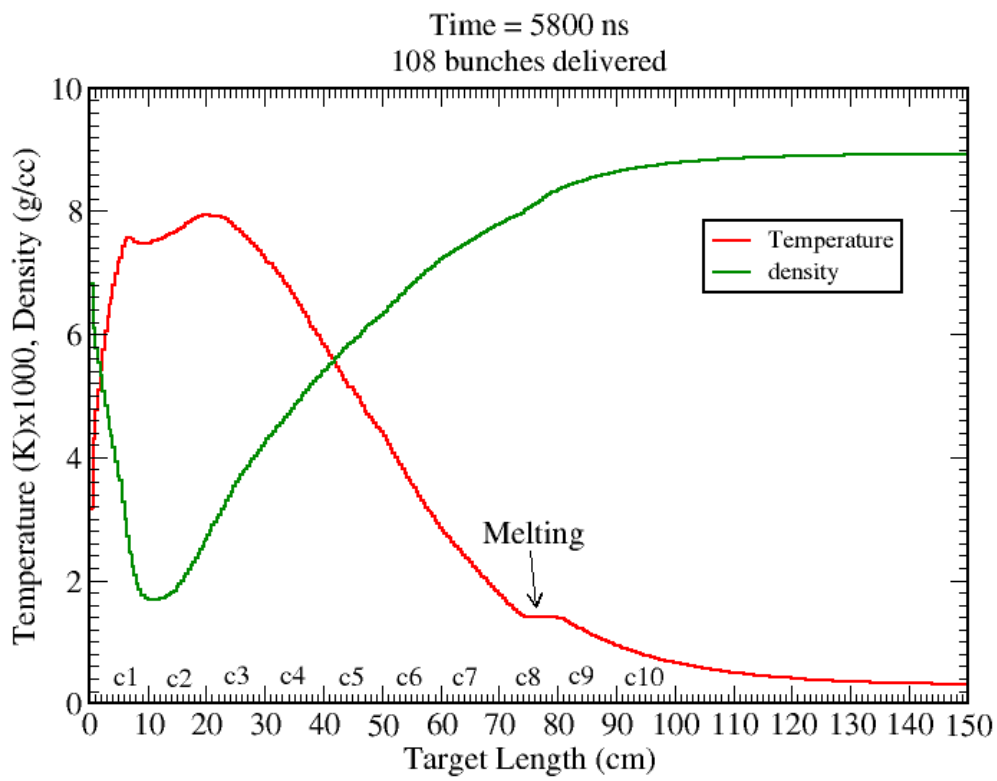


Fig. 7.11: Simulation result for target 2. It predicts that the copper is molten between $z = 0$ and $z = 80$ cm. This corresponds to a hole ending in the 8th cylinder.

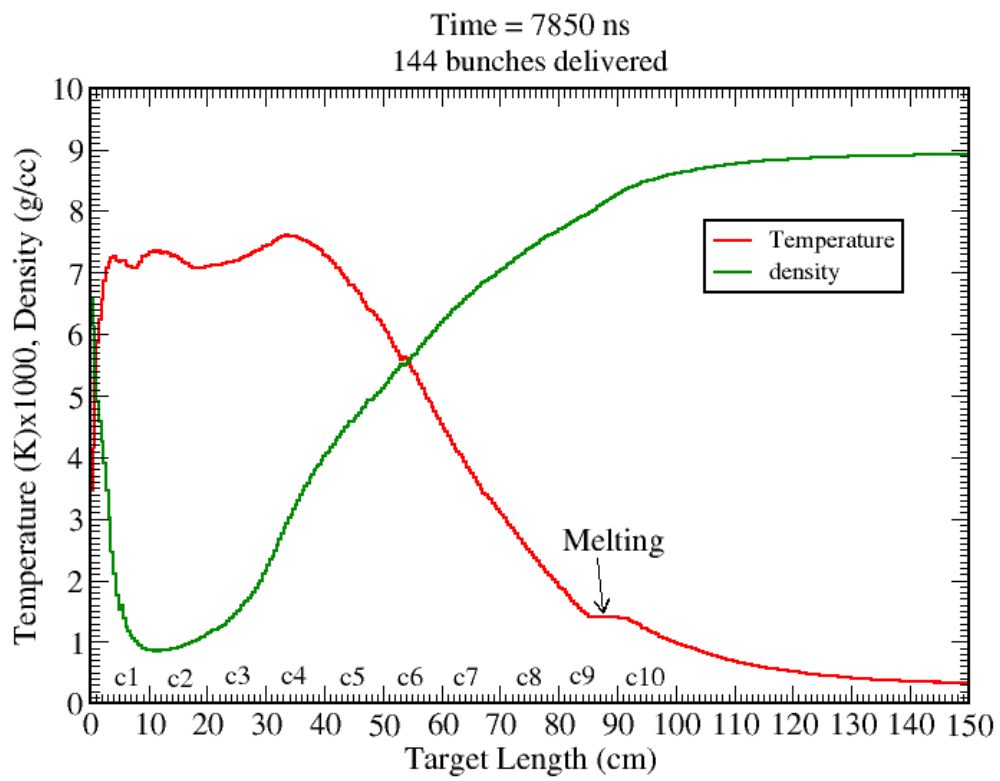


Fig. 7.12: Simulation result for target 3. It predicts that the copper is molten between $z = 0$ and $z = 90$ cm. This corresponds to a hole ending in the 9th cylinder.

8. DAMAGE SIMULATIONS FOR FCC

8.1 *Future high energy circular colliders*

Hydrodynamic tunneling of high intensity, high energy, bunched proton beams in target materials is an important process and has been observed and verified experimentally. For this, iterative FLUKA and BIG2 simulations has been benchmarked [28], [29], [74], [75]. This effect is very relevant for the LHC, therefore it must be even more present in accelerators with higher stored beam energy. For this reason a study was launched to get an estimate of the damage potential of the FCC beam. The current beam parameters of the FCC hadron beam can be found in Table 8.1. With these parameters the energy per bunch is 800 kJ and therefore a stored beam energy of 8500 MJ can be calculated. To get a first estimate a reduced beam momentum of 40 TeV/c was assumed. The outcome is important for the design of injection and extraction transfer lines and design of the beam dump, as well as the protection devices installed in the storage ring.

Tab. 8.1: Preliminary FCC beam parameters.

Particle type	protons
Beam momentum	40 TeV/c (nominal: 50 TeV/c)
Bunch intensity	1.0×10^{11} p
Number of bunches	10600
Beam size	0.2 mm
Bunch spacing	25 ns

8.2 *Geometry and simulation routine*

The simulations started in spring 2014 by using the same iteration scheme as described in chapter 7. The simulation target was made of copper, it had a radius of 2 cm and a length of 5 m. These dimensions were chosen in order to derive a good compromise between resolution (10 μ m in radial and 0.5 cm in longitudinal direction) and time required to simulate the energy deposition. To avoid instabilities of the simulation code and density oscillations, which would be unphysical, the maximum allowed density reduction for one iteration was 15 %. During the first part of the simulations, this was equivalent to the changes in the target within 25 ns, which corresponds to 1 bunch. In the later stage with reduced density decrease per step, this could be increased to 50 ns (2 bunches) and 100 ns (4 bunches) respectively. To reduce the error of the energy deposition simulation below 5 %, 70000 protons had to

be simulated. As the time consumption of the FLUKA simulations is proportional to the particle energy one simulation step took very long (~ 2.5 weeks).

8.3 Results

After the simulation of 1250 ns (51 bunches) and a total simulation time of ~ 15 months the density decrease per iteration step becomes constant. Therefore it was possible to stop the iterative simulations and extrapolate the results to the final numbers of bunches. The simulated density decrease is depicted in Figure 8.1. It shows the density along the target axis for different simulation steps. It has to be noted, that not every simulation step is plotted. For the first ~ 350 ns the energy is deposited in a very small volume, therefore the density decrease is higher compared to the later stage, in which the energy is deposited in a larger volume due to the lengthening of the projectile range. After 800 ns the density decrease per iteration step becomes constant. This effect is marked in Figure 8.1 with the distances x_1 , x_2 and x_3 at a density of 6 g/cm^3 . By using the time interval Δt of 450 ns between the f and i curve a propagation speed of $v = 1.1 \cdot 10^6 \text{ m/s}$ of the density decrease was evaluated. For the extrapolation of the penetration depth L to FCC beam parameters the following equations were used:

$$t_{\text{beam duration}} = 10600 \cdot 25 \text{ ns} = 265 \mu\text{s} \quad (8.1)$$

$$L = v \cdot t_{\text{beam duration}} = 1.1 \cdot 10^6 \cdot 265 \mu\text{s} = 291.5 \text{ m}. \quad (8.2)$$

During the simulation process the particle energy of the FCC proton beam was set to 50 TeV. As the simulations are very time consuming, the given result has to be extrapolated. Therefore the final result of the iterative FLUKA - BIG2 simulations give a penetration depth of $\sim 350 \text{ m}$.

Figure 8.2 shows the temperature after the last simulation step after 1250 ns, which corresponds to 51 bunches impacting on the target. For a better visibility only the inner 5 mm in diameter are plotted. On beam axis a maximum temperature of 119000 K was evaluated. Figure 8.3 and Figure 8.4 show the region, where the copper is above melting (1357 K) and boiling temperature (2835 K), respectively. The copper is above melting temperature up to a radius of 15.5 mm and a length of 3.25 m. It is above boiling temperature up to a radius of 8.2 mm and a length of 2.9 m. In the inner 1 mm radius and a length of $\sim 1 \text{ m}$ the target is in plasma state.

Figure 8.5 and Figure 8.6 show the pressure and density map of the target after the last simulation step after 1250 ns, which corresponds to 51 bunches impacting on the target. The pressure wave has maximum of 44.7 MPa. As the maximum energy deposition is moving deeper into the target the start point of the pressure wave is also moving. Therefore the pressure map shows a wing-shape. It can be clearly seen, that the pressure waves is not yet arrived at the target boundary. The density map shows that the lowest density with 0.94 g/cm^3 (10% of solid copper density) can be

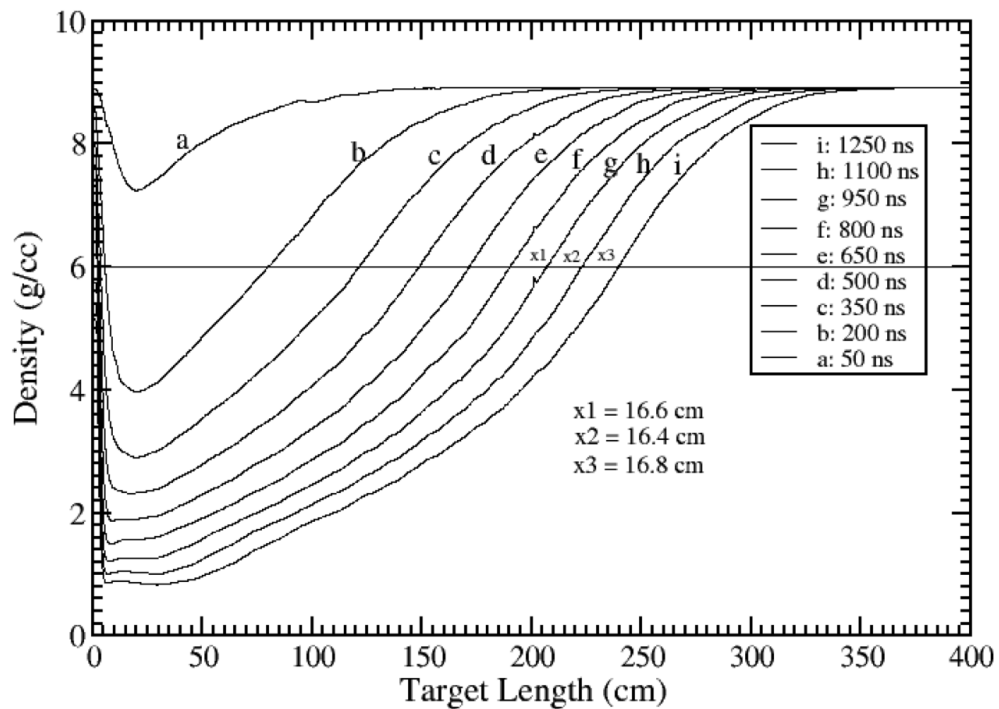


Fig. 8.1: Simulation result for the density decrease on beam axis for different time steps. For the first ~ 350 ns the energy is deposited in a very small volume, therefore the density decrease is higher compared to the later stage, in which the energy is deposited in a larger volume due to the lengthening of the projectile range. After 800 ns the density decrease per iteration step becomes constant. This effect is marked with the distances x_1 , x_2 and x_3 at a density of 6 g/cm^3 . By using the time interval Δt of 450 ns between the f and i curve the propagation speed of the density decrease was calculated.

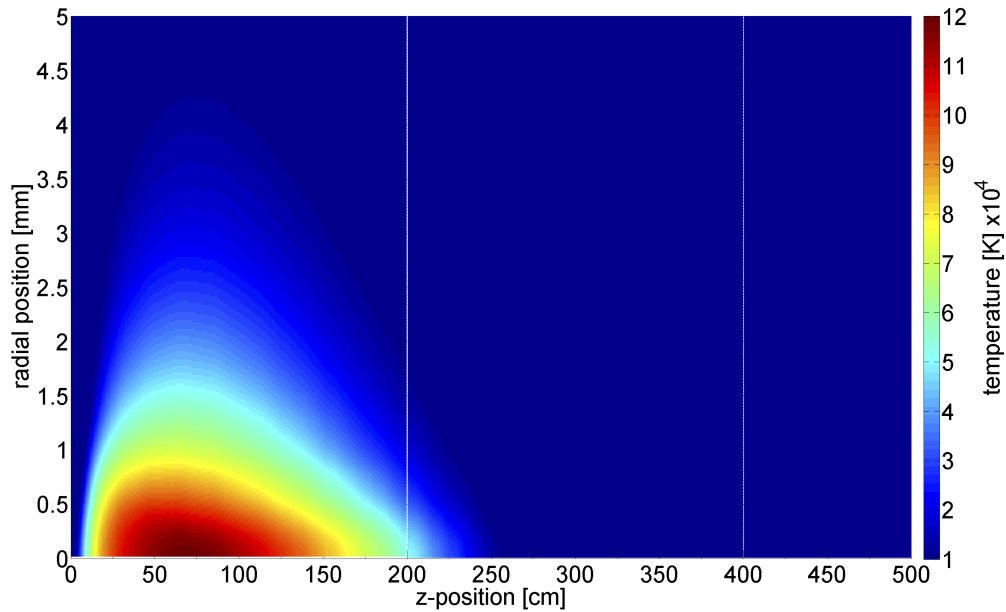


Fig. 8.2: Temperature map of the target after the irradiation with 51 bunches. The maximum temperature is 119000 Kelvin. Note: only the inner 5 mm in diameter are plotted.

found on beam axis at ~ 40 cm. The maximum density with 10.1 g/cm^3 (113% of solid copper density) is located at a radial position of 8 mm, this clearly shows that material is moved radially outwards.

The result of a penetration depth of the FCC beam of 291.5 m in solid copper will be taken into account for the design of the FCC and several accelerator components around FCC. For the FCC, new materials have to be developed and the beam size, for example in the beam dump region will be increased. Additionally, redundant system will be installed to avoid this failure case.

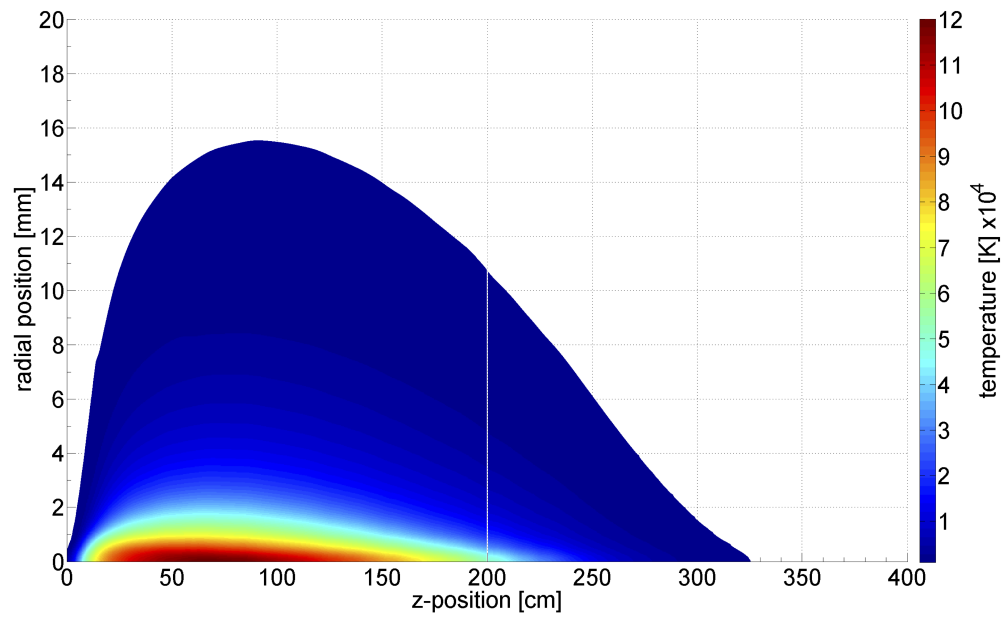


Fig. 8.3: Temperature map of the region, where the copper is above melting temperature (1357 K). It is above melting temperature up to a radius of 15.5 mm and a length of 3.25 m.

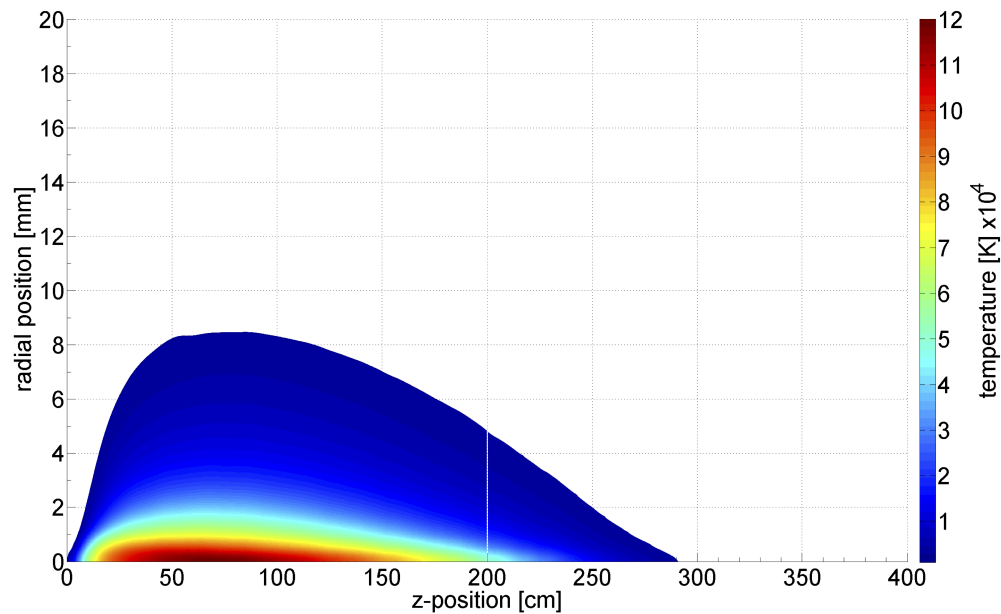


Fig. 8.4: Temperature map of the region, where the copper is above boiling temperature (2835 K). It is above boiling temperature up to a radius of 8.2 mm and a length of 2.9 m. In the inner 1 mm radius and a length of ~ 1 m the target is in plasma state.

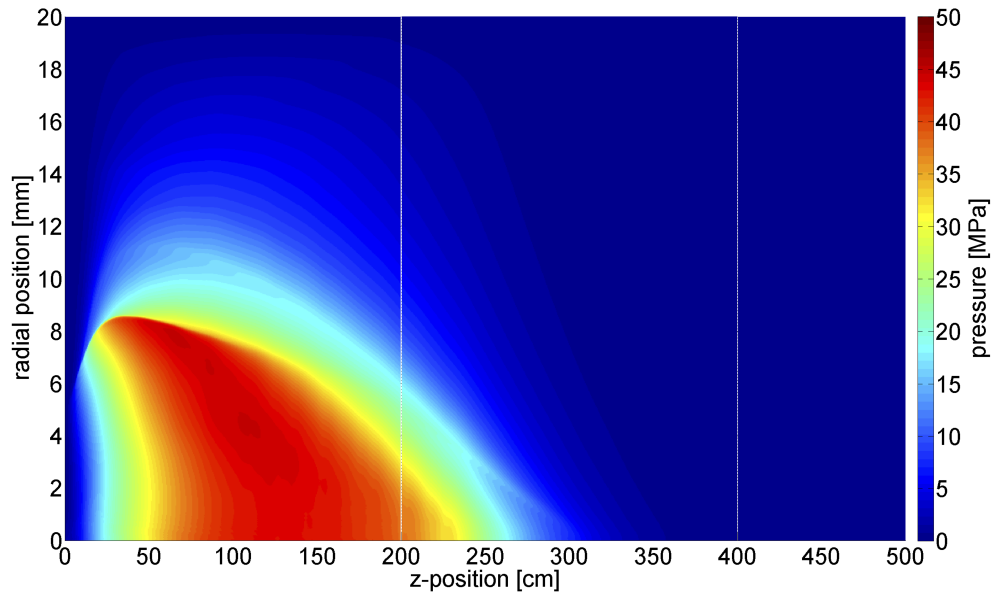


Fig. 8.5: Pressure map of the target after the irradiation with 51 bunches. The maximum pressure is 44.7 MPa. As the maximum energy deposition is moving deeper into the target the start point of the pressure wave is also moving. Therefore the pressure map shows a wing-shape. It can be clearly seen, that the pressure waves is not yet arrived at the target boundary.

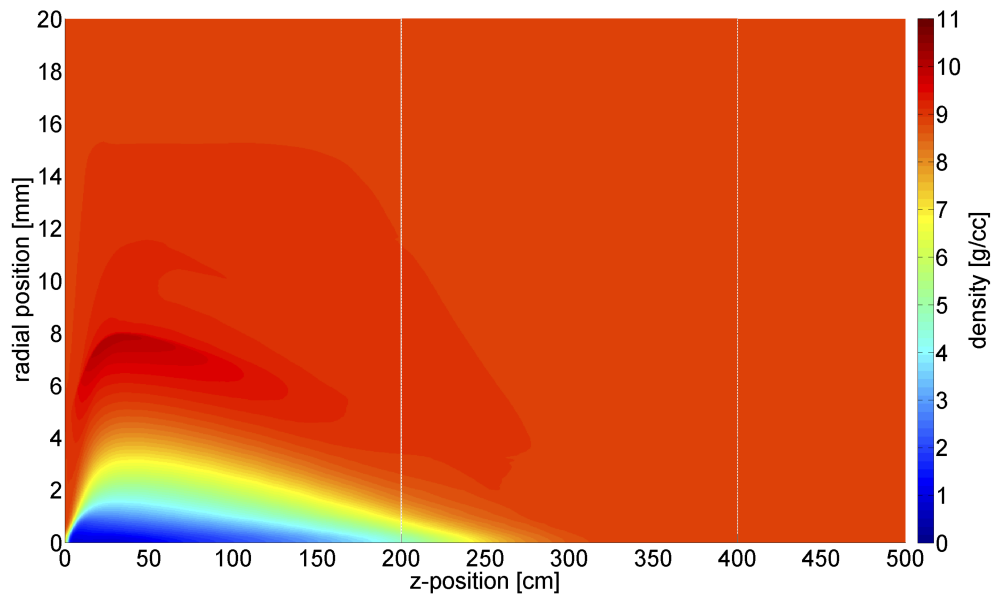


Fig. 8.6: Density map of the target after the irradiation with 51 bunches. The lowest density can be found along the beam axis with 0.94 g/cm^3 . The outgoing pressure wave moves the material outwards, therefore the maximum density of 10.1 g/cm^3 can be found in a radial distance of 8 mm.

9. CHARACTERIZATION OF DIAMOND DETECTORS

9.1 Motivation

Understanding the sources of ultra-fast failures, with durations of less than 3 LHC turns, is important for a safe operation of the LHC, as only passive protection is possible in these time scales. Diamond particle detectors (dBLMs) with bunch-by-bunch resolution and high dynamic range have been successfully used to improve the understanding of some new ultra-fast loss mechanisms discovered in the LHC during the so-called run 1 (2009-2012). To fully exploit their potential, diamond detectors were characterized with a high-intensity electron beam (10^4 to 10^9 electrons per shot). For the first time their efficiency and linearity has been measured in such a wide range of bunch intensities.

9.1.1 Measurements during hydrodynamic tunneling experiment

For the first time three dBLMs were used during the hydrodynamic tunneling experiment described in chapter 6. The goal was to online-monitor the hydrodynamic tunneling process. Therefore the dBLMs were mounted onto the experimental setup to detect the particle showers. For target 1 where only some tunneling was expected, the signal from the dBLMs should not change with time. On the contrary, for target 2 and 3 where hydrodynamic tunneling was expected, the diamond signals should increase with time reflecting the density changes in the target. The measured signals for 144 bunches can be found in Figure 6.3 and a zoom in between the bunch trains in Figure 6.4. The temporal profile of the 144 bunches proton beam shows a decay of the signal amplitude. This does not indicate a droop of the bunch intensity, it is due to a discharge of the supply capacitance in the diamond detector. The bunch intensity was constant along the four trains. The strong discharge of the high-voltage capacitor results in a decrease of the charge collection distance and efficiency of the diamond. The time constant of the capacitor with 111 ms is compared to the irradiation duration of $7.2 \mu\text{s}$ very large. Therefore the capacitor does not recharge during the irradiation. To correct for this effect a correction of the measured charge per shot was performed [43]. The correction algorithm has not considered all dynamic effects in the diamond detector. In addition different behaviors of the three used dBLMs were observed. Therefore, it was decided to characterize the dBLM with a particle beam in the high intensity range above 10^4 MIPs per shot to study saturation effects and efficiencies.

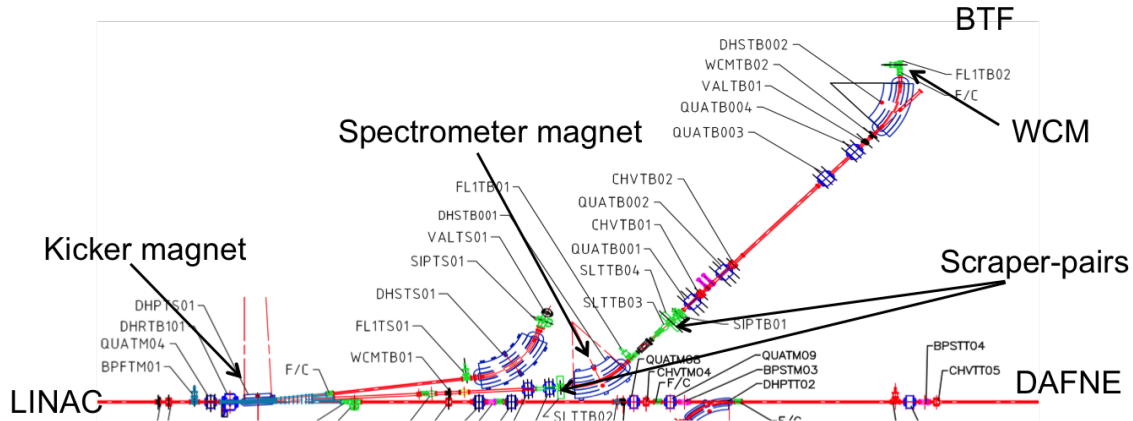


Fig. 9.1: Schematic drawing of the BTF transfer line complex.

9.2 Efficiency and Linearity of dBLMs

9.2.1 BTF at INFN, Frascati

The DAFNE Beam Test Facility (BTF) at the Istituto Nazionale di Fisica Nucleare (INFN), Laboratori Nazionali di Frascati (LNF) is a beam transfer line optimized for the delivery of a pre-determined number of electrons or positrons. It can provide electron or positron beams from single particles up to 10^{10} particles per pulse with an energy from a few tens of MeV up to 800 MeV with an energy spread of 1 %. The pulse width can be adjusted between 1 and 10 ns. The maximum repetition rate is 50 Hz [51], [52]. The facility is particularly suitable for particle detector testing purposes, i.e. for efficiency and linearity measurement, high-energy detector calibration, low energy calorimetry, electronic equipment aging measurements, beam diagnostics device tests, etc. The BTF is a part of the DAFNE accelerator complex, consisting of a double ring electron-positron collider, a high current linear accelerator (Linac), an intermediate damping ring and a system of 180 m transfer lines connecting the whole system. The e^+ / e^- beam produced by the LINAC is stacked and damped in the accumulator ring, from which it is extracted and injected into the main rings. In BTF operation mode the bunches are sent from the Linac to the experimental area with a kicker magnet, the following beam transfer line is composed of different dipoles, quadrupoles, correctors and couples of vertical and horizontal scrapers. The beam line ends at the beam exit window, which is followed by a 100 m² experimental hall, where experimental equipment can be installed. The beam parameters of the Linac can be found in Table 9.1. A schematic drawing of the BTF beam transfer line is presented in Figure 9.1 [51].

During BTF operation, the high current Linac beam can be attenuated by a target (downstream of the kicker magnet) in order to strongly increase the energy spread of the primary beam. Afterwards the secondary particles are energy selected by means of a spectrometer, respectively bending magnet and slits system. The energy selector only accepts a small fraction of the resulting energy distribution, thus reducing the number of particles in the beam by a large and tunable factor. With this method an intensity range in the experimental area between 1 and 1×10^4 particles

Tab. 9.1: Linac parameters for electrons and positrons of the INFN, Frascati.

	electrons	positrons
Energy (MeV)	510 (nominal), 750	510 (nominal)
Max. current / bunch (mA/bunch)	500	100
Transv. emittance (mm · mrad) @ 510 MeV	1	10
Energy spread @ 510 MeV	1 %	2.5 %
Pulse duration (ns)	1 - 10	1 - 10
Repetition rate (Hz)	1 - 50	1 - 50

per pulse can be covered. The full Linac pulse (without target operation) can be tuned by changing the aperture of the upstream and/or downstream horizontal and vertical collimators. In particular, the measured multiplicity increases by increasing the slits aperture until the intrinsic beam spot size is exceeded. This operation mode covers an intensity range between 1×10^4 and 1×10^{10} particles per pulse with an energy of 510 MeV.

The BTF is equipped with beam screens (scintillating screens and Medipix) to measure the beam position and beam size. A Integrating Current Transformer (ICT) directly upstream of the beam exit window and an external calorimeter to measure the pulse intensity. A picture of the beam transfer line in the experimental hall is shown in Figure 9.2. The beam is entering on the right, is focussed with two quadrupole magnets (orange) and bend with the last dipole magnet (red) before the beam passes the ICT and the 0.1 mm thick beryllium beam window, which seals off the beam line (on the left). The experimental area is equipped with a movable table and a laser system to align the experimental setup to the beam. The facility provides a beam trigger to the users [52].

9.2.2 Experimental setup

During the beam times three 100 μm thick dBLMs, specially designed for high-fluence experiments (in collaboration with CIVIDEC, Vienna, Austria) dBLMs and two 500 μm thick standard LHC dBLMs were studied. The scope of this thesis is the characterization of the 100 μm thick dBLMs, called H1, H2 and H3. The standard LHC dBLMs are topic in an other thesis. The setup for the dBLM characterization was installed 50 cm downstream of the beam window. The detector circuit board with the active polycrystalline diamond was fixed on the front plate of a hollow copper cylinder (20 cm length, 5 cm diameter). To increase the angular acceptance the diameter of the hole in the cylinder had a diameter of 6 mm, i.e. 1 mm larger than the active detector material. Furthermore the hole's diameter in the copper cylinder was increased stepwise by 1 mm every 5 cm, leading to an angular acceptance of 10 mrad. To minimize the Bremsstrahlung a 6 cm long hollow lead cylinder with a diameter of 16 mm hole was added after the copper cylinder. The goal of these collimators was to stop all the particles, which haven't interacted with the active area of the dBLM. Particles interacting with the dBLM will travel directly to the reference detector. A schematic drawing of the used collimator can be found in Figure 9.3.

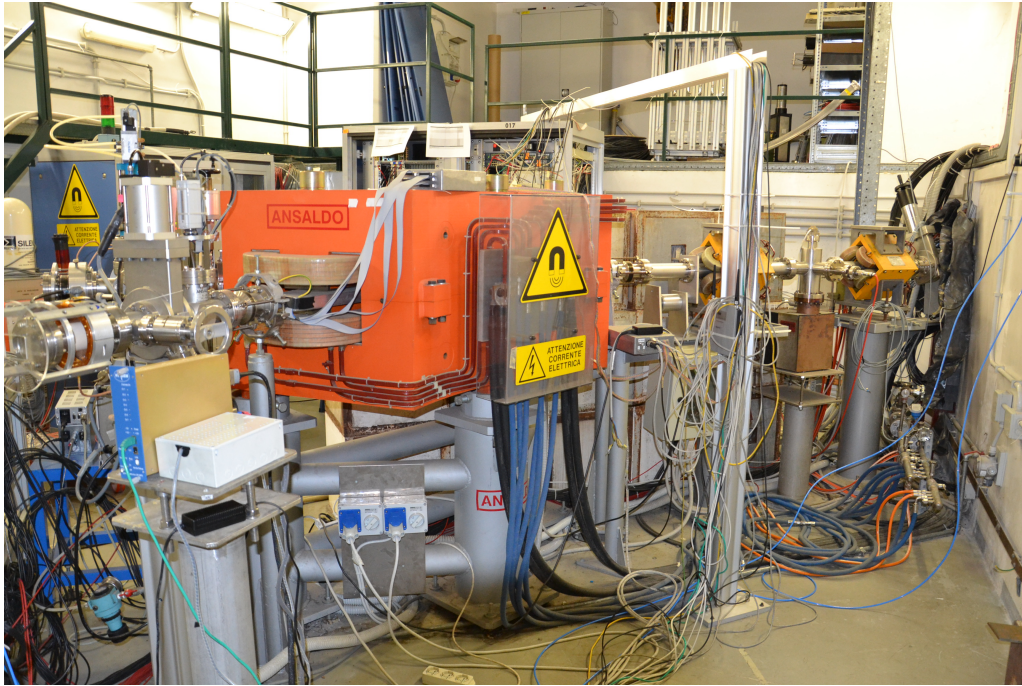


Fig. 9.2: Picture of the last meters of the BTF beam line. The beam is entering on the right, passing 2 quadrupole magnets (orange), followed by a bending magnet (red). The ICT and the beam window can be seen on the left at the end of the beam line.

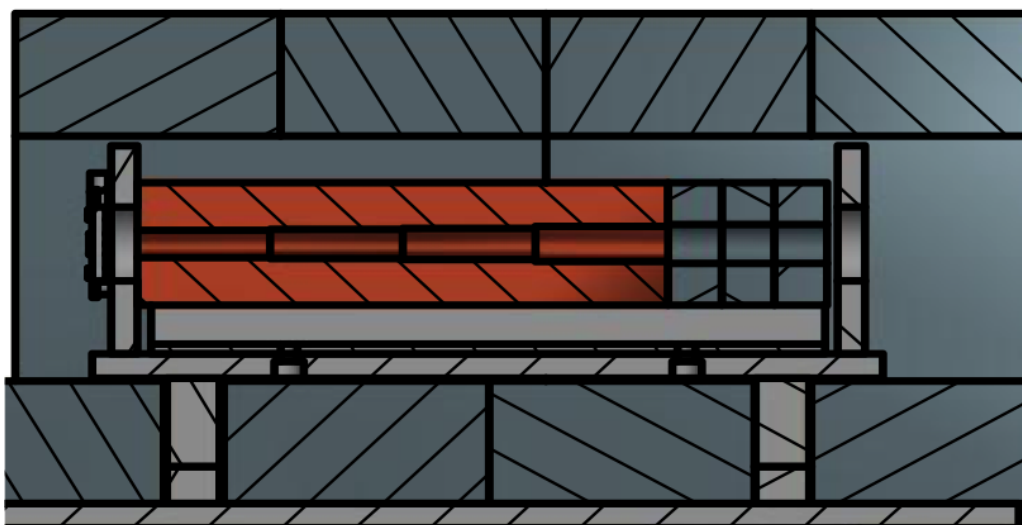


Fig. 9.3: Schematic drawing of the collimator. The copper part is colored in brown, the lead part further downstream is gray. The lead shielding surrounds the collimator.

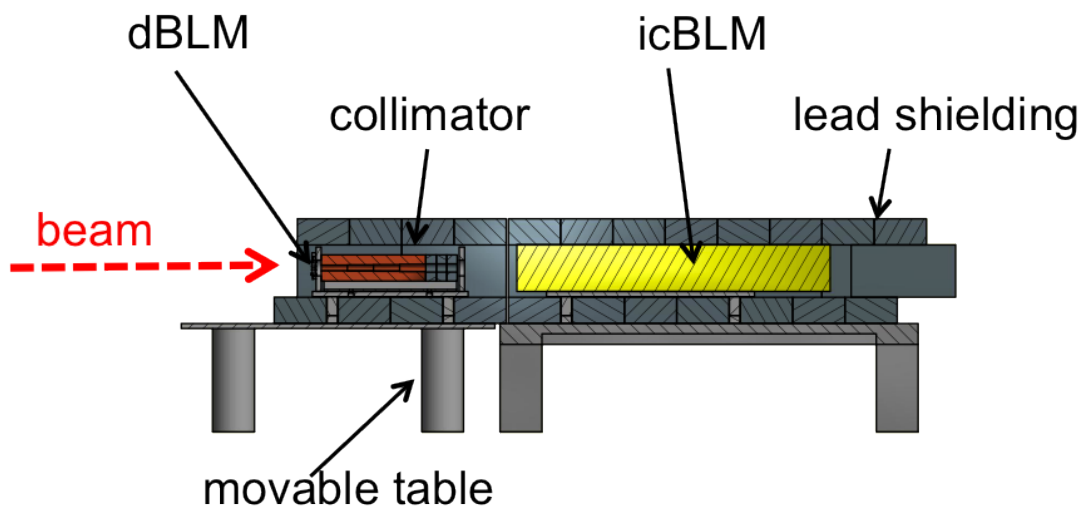


Fig. 9.4: Schematic drawing of the experimental setup with the diamond detector (dBLM) and the ionization chamber (icBLM).

The setup was aligned during installation with the help of the installed laser system. In addition, the movable support allowed a beam-based alignment of the detector setup with a incremental transverse adjustment of 0.5 mm. The angular misalignment of the setup was small (δ hor. plane: 0.5 mrad, δ vert. plane: 0.5 mrad) in respect to the angular acceptance of the setup. As reference detector a standard LHC ionization chamber (icBLM) was used which was installed 10 cm downstream the collimator on a fixed table. A schematic drawing of the experimental setup can be found in Figure 9.4. It is to be noted, that only the dBLM and the collimator are placed on the movable experimental table. The icBLM is placed on a fixed table. This won't reduce the accuracy of the experiment, because the full setup was aligned to the beam with the laser system. The beam based alignment with the movable table was done with only a few steps in each direction (maximum displacement of 1.5 mm). This influences the accuracy of the dBLM setup, but it has no influence on the icBLM setup due to big acceptance of the icBLM (10 cm diameter).

By using scrapers the particle intensity of the 10 ns long bunches could be decreased from 1×10^{10} down to 1×10^4 electrons per pulse. Additional intensity measurements were conducted with the ICT which was installed directly upstream of the experimental setup. The sensitivity limit of this device was found to be 1×10^7 electrons per pulse. An overview of the experimental beam parameters is shown in Table 9.2.

To minimize the radiation in the experimental hall, FLUKA dose rate simulations were performed to study the necessary shielding of the experimental setup. The results showed that surrounding the experimental setup with a 5 cm thick lead shielding and 40 cm lead shielding downstream of the icBLM is sufficient to reduce the dose rate to $0.75 \mu\text{Sv} / \text{shot}$ of 1×10^9 electrons in a distance of 50 cm from the beam axis. The results of these simulations are presented in Figure 9.5. The inner structure of collimator and the icBLM is shown, surrounded by the lead shielding.

Tab. 9.2: BTF beam parameters used during the beam time.

Particle type	electrons
Energy (MeV)	510
Intensity / pulse	$10^4 - 10^9$
Pulse duration (ns)	10
Repetition rate (Hz)	1 - 5

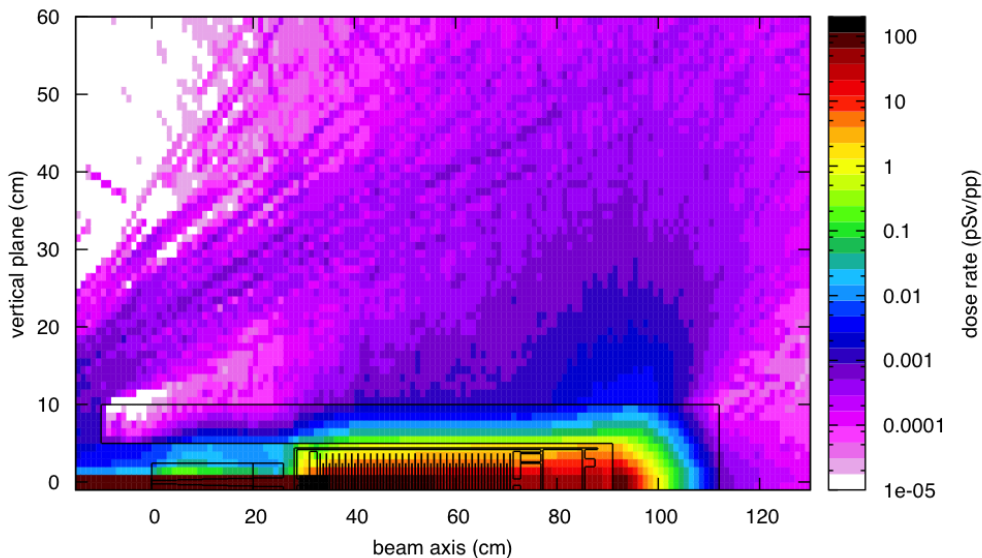


Fig. 9.5: Simulated dose rate (pSv/h/pp). The picture shows the collimator and the icBLM with the lead shielding. A dose rate of $0.75 \mu\text{Sv}/\text{shot}$ of 10^9 electrons in a distance of 50 cm from beam axis was evaluated.

The regions with the highest dose rates outside the setup can be found in the air - gap, between setup and beam window and at the end of the icBLM, where the particles are stopped. During experimental phase no significantly increased dose rate was observed by the radio-protection team of the LNF, which approves the shielding design of the setup.

The experimental setup with and without the lead shielding structure during the installation is shown in Figure 9.6 and Figure 9.7.

As read-out system an Agilent DSO 9254 oscilloscope with 2.5 GHz bandwidth on 4 analog channels and a maximum sampling rate of 20 GSa/s was used. As an alternative a Keithley 6517B electrometer can be used. The oscilloscope was used to receive the beam trigger signal of the facility and trigger the electrometer. The signal of the dBLM and the signal of the icBLM was recorded by the oscilloscope, cross-check measurements of the icBLM with the electrometer were performed to have an additional read-out for the icBLM. To attenuate the signal in case of high ionization in the diamond material. Standard CIVIDEC attenuators with -20 dB, -40 dB and -60 dB were used.

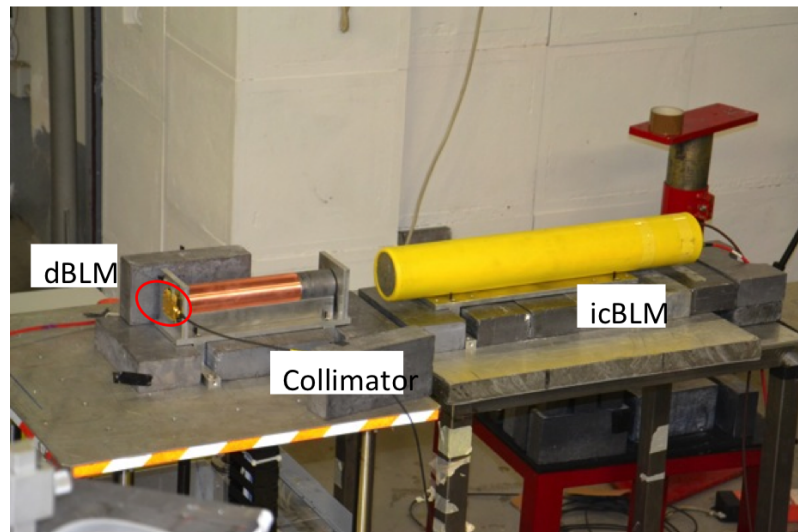


Fig. 9.6: Experimental setup. The dBLM and the collimator are installed on a movable table. The reference detector (icBLM) is placed downstream on a fixed table.

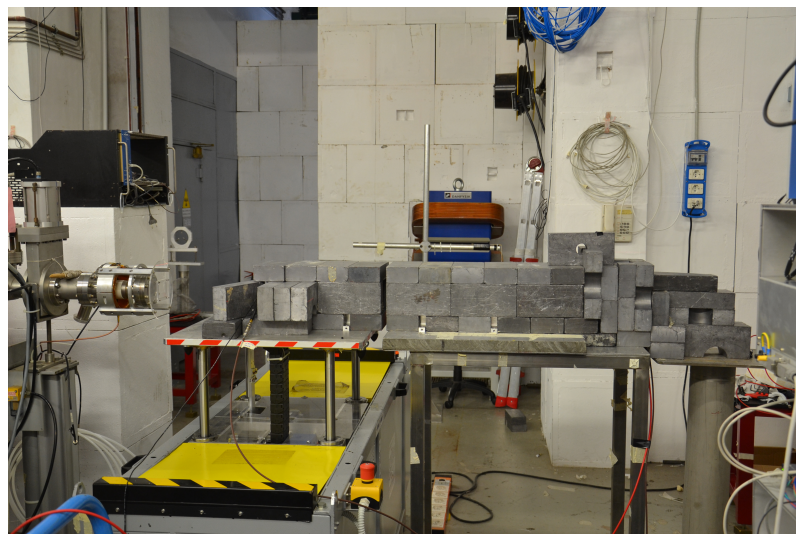


Fig. 9.7: Experimental setup with lead shielding. On the left hand the beam exit window can be seen.

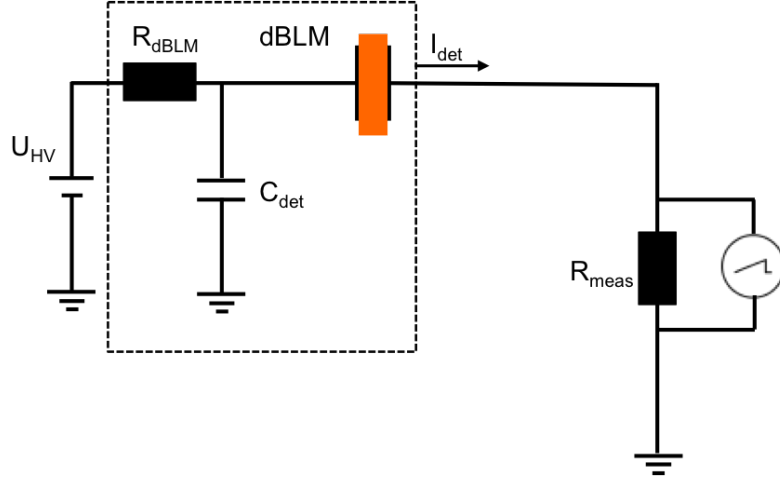


Fig. 9.8: dBLM electrical circuit. The dBLM box is marked with the dashed line. The diamond itself is marked in orange.

50 Ω read out system

During the first beam time in March 2014 the standard LHC dBLM 50 Ω read-out system was used. The corresponding circuit diagram is shown in Figure 9.8. U_{HV} was set to 100 V, which corresponds to an electric field strength of 1 V/ μm across the diamond. The dBLM box is marked with a dashed line. R_{dBLM} is 1 M Ω , the capacitance in the dBLM has 111 nF and the measurement resistance is 50 Ω .

1 Ω read out system

In the second beam time end of November 2014 an additional 1 Ω read-out system was used and tested. A circuit diagram of this system is presented in Figure 9.9. The shunt consists of a resistance of $R_{shunt} = 1\Omega$. The resistance of the oscilloscope is still $R_{meas} = 50\Omega$. The dBLM is simplified pictured as a box with the output the I_{det} as detector current. The total resistance of the measurement system R_{tot} can be calculated as shown in the following equation:

$$\frac{1}{R_{tot}} = \frac{1}{R_{shunt}} + \frac{1}{R_{meas}} \quad (9.1)$$

$$R_{tot} = 0.98\Omega. \quad (9.2)$$

The other components of the set-up have the same values as described in the 50 Ω set-up, see Figure 9.8.

9.2.3 Results of dBLM characterization

Figure 9.10 shows the first signals of the three detectors used during the beam time, dBLM in blue, icBLM in red, ICT in green. The signal of the ICT was

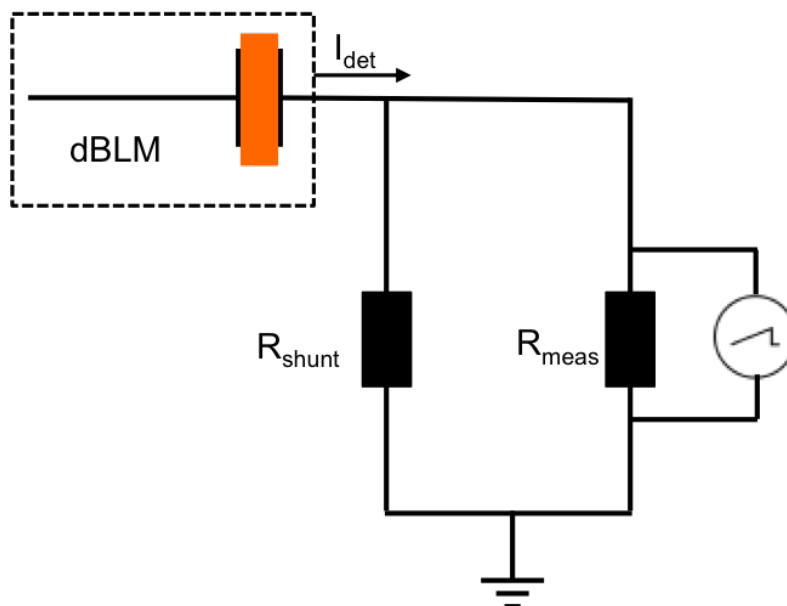


Fig. 9.9: Circuit diagram of the used $1\ \Omega$ shunt system. The dBLM box is marked with the dashed line, delivering the detector current I_{det} .

artificially increased by a factor 5000. The signals were recorded with oscilloscope, described above. It is clearly visible, that the dBLM has the faster response time and, in addition the shortest FWHM. The analysis shows that the ICT has the lowest signal-to-noise ratio (SNR). Table 9.3 lists the average SNR for the three detectors.

The first measurements were taken with the standard $50\ \Omega$ read-out system. Due to the limited amount of time during the first beam time, the measurements were conducted only in two intensity ranges with bunch intensities between 8×10^4 and 5×10^4 as well as 1×10^8 and 4×10^9 electrons. During these measurements the response and the efficiency for different bias voltages of the three dBLMs was studied. Due to the resolution of the oscilloscope only one half of the icBLM signal, the part induced by impacting electrons, was recorded. Therefore the icBLM signal has been corrected by a factor 2. This correction factor was calculated from experiments with ICT and icBLM and verified by previous tests in CERNs PS [98].

Tab. 9.3: Signal to noise ratio (SNR) of the three detector types.

	ICT	icBLM	dBLM
SNR	6.5	1670	4238

Figure 9.11 shows the measured signals in the two intensity ranges. The signal of the dBLM is plotted vs. intensity measured by the icBLM, the colour indicates the different electric fields, induced by the different bias voltages, across the diamond. The signal for a given intensity increases by a factor 2.2 for field strengths between 0.7 and $2.3\ \text{V}/\mu\text{m}$. Figure 9.12 and Figure 9.13 show a zoom in the lower and higher intensity range. In the lower intensity range, all response measurement points show a linear behaviour with a slight variation of the gradient. The gradient indicates

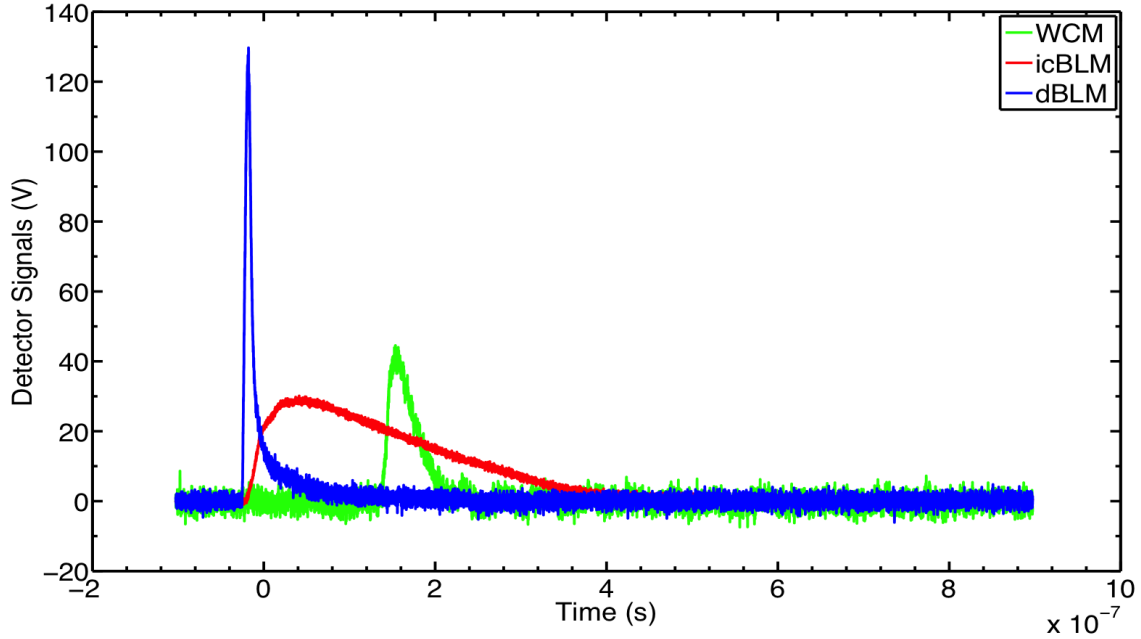


Fig. 9.10: First signals of ICT (*5000) in green, icBLM in red and dBLM marked in blue.

the conversion factor from diamond detector signal in Coulomb to the number of particles. In the higher intensity range the response is non-linear. Due to fact that the intensity range was too small the transition between linear and saturation behaviour of the measurement points for the different electric field strengths was not found.

At high intensities a very high ionization in the diamond material was observed. This leads to a high detector current and a high measured voltage. This phenomenon will decrease the electric field in the diamond as the bias voltage, U_{HV} , voltage at the diamond, $U_{diamond}$, and measured voltage, $U_{measurement}$, are coupled as shown in the following equation.

$$U_{HV} = U_{diamond} + U_{measurement} \quad (9.3)$$

Therefore the maximum achievable detector current is limited to:

$$I_{det,limit} = \frac{U_{HV}}{50\Omega} \quad (9.4)$$

i.e. for $U_{HV} = 100$ V the detector current is limited to 2 A. Due to the decrease of the electric field across the diamond material, the drift velocity of the electron-hole pairs is reduced. This will lead to a longer dwell time of the electron-hole pairs in the diamond, which leads to a higher probability of recombination. Therefore a part of the signal is lost. This effect can be observed in the FWHM of the signal response. With increasing intensity, the FWHM increases significantly.

As described above this saturation observed in Figure 9.13 is caused by the resistance of the read-out system. When the amplitude of the signal reached ~ 60

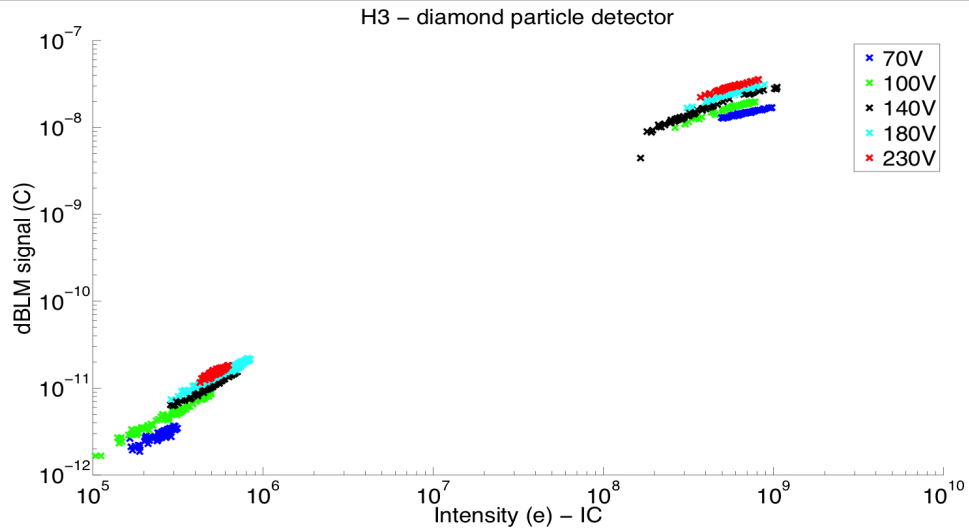


Fig. 9.11: All measurements recorded from the reference detector (ic) and the dBLM. The two intensity ranges are clearly visible. The plot shows all the measurements for the different bias voltages.

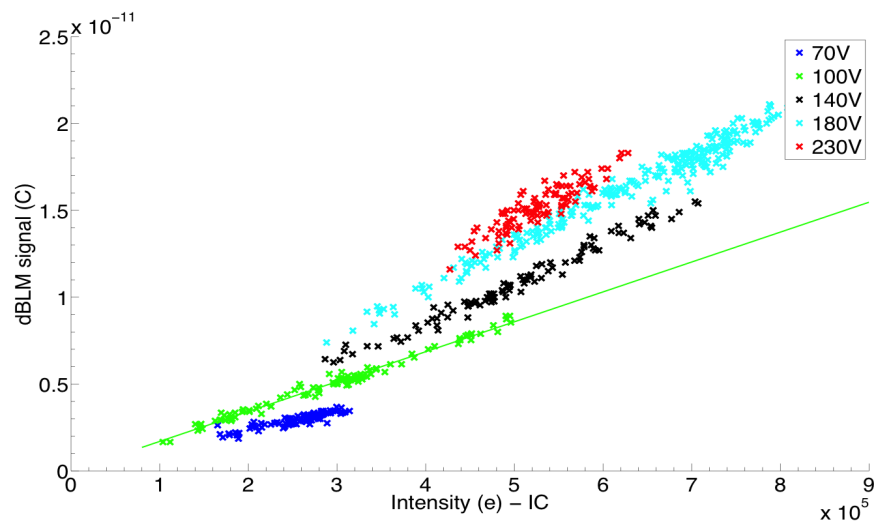


Fig. 9.12: Zoom in the lower intensity range. All response measurement points show a linear behaviour with a slight variation of the gradient. The gradient indicates the conversion factor from diamond detector signal in Coulomb to the number of particles.

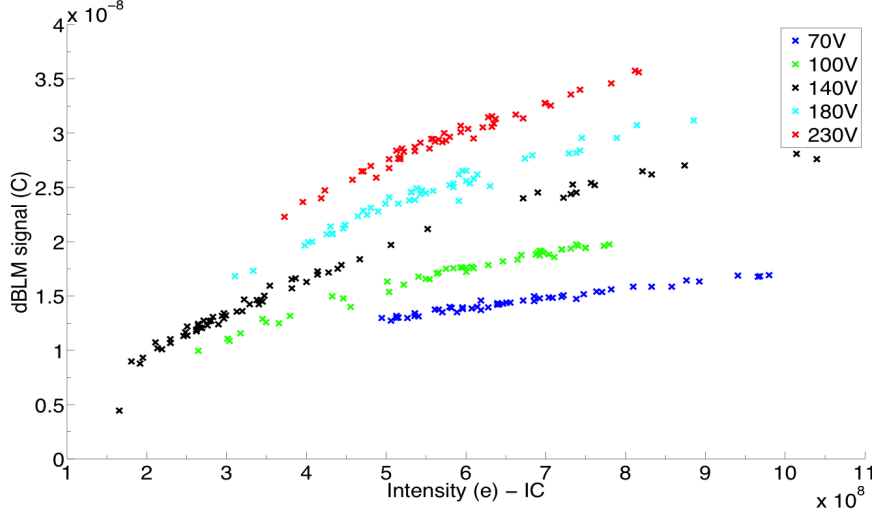


Fig. 9.13: Zoom in the higher intensity range. The response behavior is non-linear. Due to fact that the intensity range was too small the transition between linear and saturation behaviour of the measurement points for the different electric field strengths was not found.

% of the bias voltage the signal went into saturation and only the FWHM increased further. Figure 9.14 shows the FWHM vs. peak amplitude for different bias voltages in an intensity regime between 1×10^8 and 5×10^8 . For a bias voltage of 70 V, this dBLM was already in saturation at the beginning of the plotted intensity range.

For the first time this effect of a limitation in the dynamic range caused by the read-out electronics was seen. To avoid this limitation a 1Ω high-frequency shunt was built by CIVIDEC. This system was used in the second beam time at the BTF. For this read-out system the detector current I_{det} was calculated using Ohms law.

$$I_{det} = \frac{U_{meas}}{R_{tot}} \quad (9.5)$$

The maximum detector current for a pulse can be calculated with the following equation:

$$I_{det,max} = \frac{U_{meas,max}}{R_{tot}} \quad (9.6)$$

For this 1Ω shunt system the dynamic range limitations due to the read-out system were shifted to:

$$I_{det,limit} = \frac{U_{HV}}{R_{tot}} \quad (9.7)$$

therefore the maximal achievable detector current with the used 100 V bias voltage is 102.04 A. During this beam time a maximum detector current of 18 A was recorded.

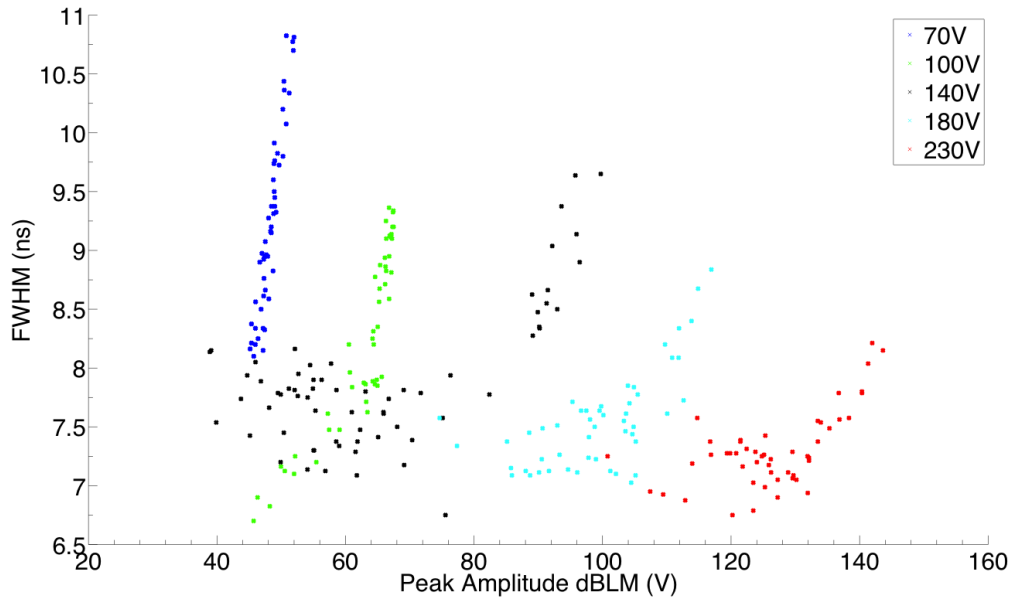


Fig. 9.14: FWHM vs. peak amplitude of the dBLM for different bias voltages.

9.2.4 Response measurements

To cover 5 orders of magnitude intensity range a set of attenuators (-20 dB and -40 dB) was used. They were installed in-between the BNC-cable and the scope. To avoid limitations due to the $50\ \Omega$ read-out system at high intensities a $1\ \Omega$ shunt was installed between the dBLM and the BNC-cable to the scope. With a given attenuator-shunt configuration an intensity range of about two orders of magnitude was covered. The measurements with different attenuators respectively shunt were performed with an overlap to allow a comparison of the different configurations. The dBLMs, and the icBLM were operated at their nominal bias voltages of 100 V and 1500 V respectively.

For the analysis automated scripts were developed to allow a first quick online analysis during the experiment, for the final analysis, these scripts were refined. The measured voltage signal has to be integrated and divided by the resistance of the read-out system to get the measured charge. To minimize the effects of dark currents the offset of the signal was corrected. To reduce the noise on the signal the signal curve was flattened. The flattening function was set in this way, that the error due to this process is below 1%. Signal losses due to damping effects in the cable of fast signals dBLM signals (FWHM of ~ 10 ns) were compensated by applying a correction factor ($c_{cable} = 1.23$). This factor was measured in the lab by using a fast pulse generator and the original cable set-up. For the measurements where an attenuator was used the signal was corrected by a factor 10 for -20 dB and a factor 100 in the case of -40 dB. These values were re-measured and approved in the lab at CERN. Another correction factor $c_{icBLM} = 2$ was used to correct the signal of the icBLM. Due to resolution limits only the electron or ion part of the signal could be measured. Analysis of the two pulses showed a relation of the two signals is 1:1.

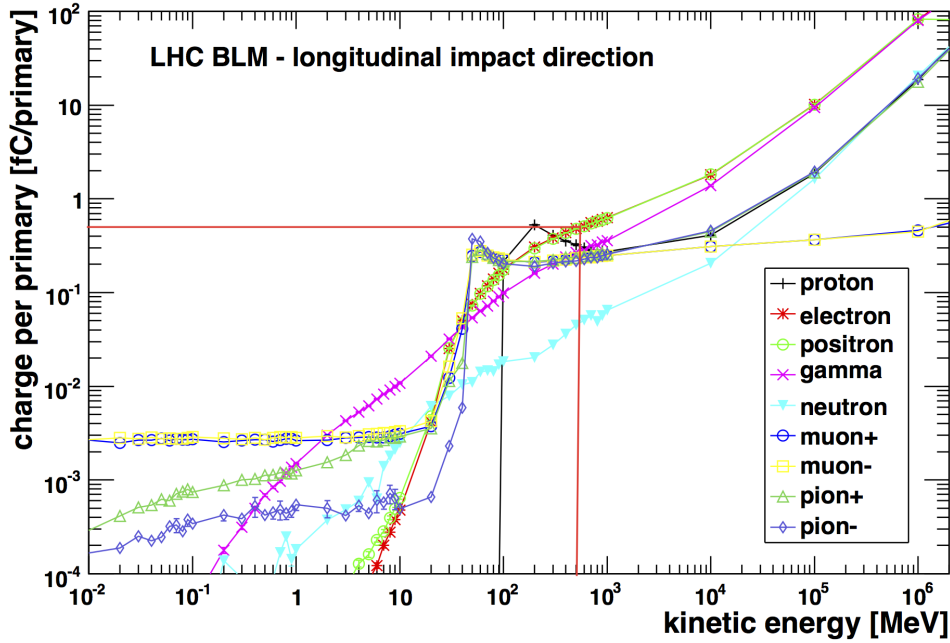


Fig. 9.15: Response curves for different particles impacting orthogonally on a standard LHC beam loss monitor ionization chamber. Electrons are marked with red stars. The response factor for 500 MeV electrons is $r_{icBLM} = 0.5$ fC/electron (marked with the red lines). Courtesy: B. Dehning.

With an energy of 500 MeV the electrons are minimum ionising particles (MIP) and a response factor $r_{icBLM} = 0.5$ fC/electron was applied to the signal of the icBLM to receive the number of particles impacting on the icBLM, Figure 9.15 shows the response curves for different particles impacting orthogonally on a standard LHC beam loss monitor ionization chamber. The curve for electrons is marked with red stars, the corresponding value for 500 MeV electrons is marked with the red lines. This response factor has an error of $\sim 10\%$. Table 9.4 lists all the correction and response factors used during the analysis.

Tab. 9.4: Correction and response factors used during the analysis of the dBLM characterization.

icBLM response factor for 500 MeV electrons	0.5 fC/electron
Correction due to signal loss in the cable	1.23
Correction due to recording of electron peak only	2
ICT gain	10
Attenuator -20 dB	10
Attenuator -40 dB	100

In Figure 9.16 the measured response of all three dBLMs (H1, H2 and H3) are shown.

The lower intensity limit is given by the resolution limit of the DAQ which is $\sim 3 \times 10^4$ electrons/shot. Below this value it is necessary to install an amplifier for the

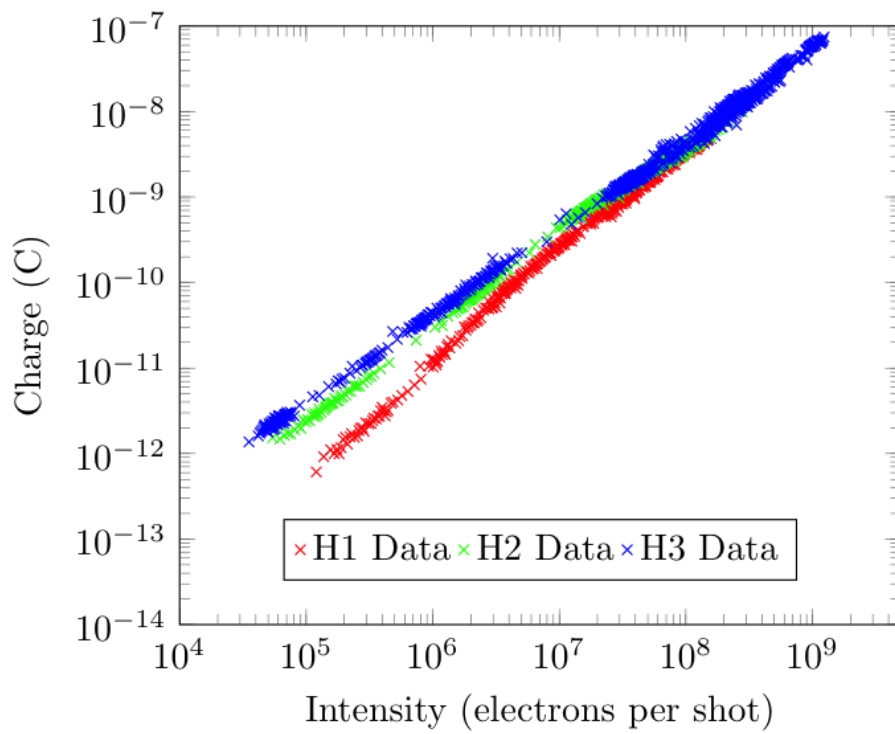


Fig. 9.16: Response of the three dBLMs (H1, H2 and H3). On the x-axis the measured intensity from the icBLM in electrons per shot is shown. The y-axis represents the measured charge from the dBLM.

dBLM. Amplifiers of +20 dB and +40 dB from CIVIDEC can be used. With the use of these amplifiers intensities down to tens of electrons can be measured. But also the icBLM is at its resolution limit, therefore also a change in the reference detector from icBLM to a calorimeter should be considered for the lower intensity range. As the scope of the beam times was to measure the high intensity response of the dBLMs the measurements were stopped at this level. The upper intensity limit at 1×10^9 electrons/shot is given by the radiation protection system of the BTF. At this level the radiation thresholds in the experimental hall were exceeded. Intensities up to $\sim 10^{10}$ electrons per shot can be measured with a dBLM for even higher intensities hardware damage on the dBLM and the shunt might be possible.

During the measurements the full range between 10^4 and 10^9 electrons per shot was covered almost completely and without major gaps. For every detector more than 4000 measurements were performed, in case of the H3 detector more than 10000. Note: in Figure 9.16 only every 10th point is plotted to allow a better readability of the plot, in addition the data was intensity - binned.

9.2.5 Efficiency measurements

The efficiency ϵ of the detectors was calculated as:

$$\epsilon = \frac{Q_{dBLM}}{Q_{icBLM} \cdot d \cdot \eta} \cdot 100 \quad (9.8)$$

with the charge generated in the dBLM, Q_{dBLM} , the charge generated in the icBLM, Q_{icBLM} , the thickness of the active detector material d in μm and the number of electron/hole pairs created by a MIP passing $1 \mu\text{m}$ of diamond material, $\eta = 36$.

The efficiency of H1 and H2 is shown in Figure 9.17 and Figure 9.18. They show a change of the efficiency over four orders of magnitude of absolute 5 %. The trend of the change is comparable for both detectors. The significant change of efficiency between 10^6 and 10^7 electrons/shot can be explained by changing the beam parameters due to changing the scraper positions during data taking. As not only the beam intensity but also the beam size is influenced by the scraper positions. A change of beam size would lead to a different area of irradiation on the diamond material. A detailed analysis of this phenomenon is not possible as no shot by shot beam size monitoring is available at the BTF.

The efficiency behavior at lower intensities can be explained by the scraper position, mentioned above. For this case the gap opening of the scrapers was about $100 \mu\text{m}$. Due to the polycrystalline structure of the diamond, the local efficiencies might differ. With small beam sizes it is possible that only an area with lower efficiency was irradiated. The detectors have a mean efficiency of 5.7 % (H1) and 9.2 % (H2).

The efficiency of the H3 detector is shown in Figure 9.19. It shows a linear behavior within the measurement tolerances of ± 20 %. A decrease of the efficiency for the measurements with the -40 dB attenuator (blue) can be observed. This is due to the quenching of the bias voltage while using the 50Ω read-out system. This effect does not appear in the data when the shunt was used (black). The increase of efficiency for the high intensity range (orange) might come from the effect described

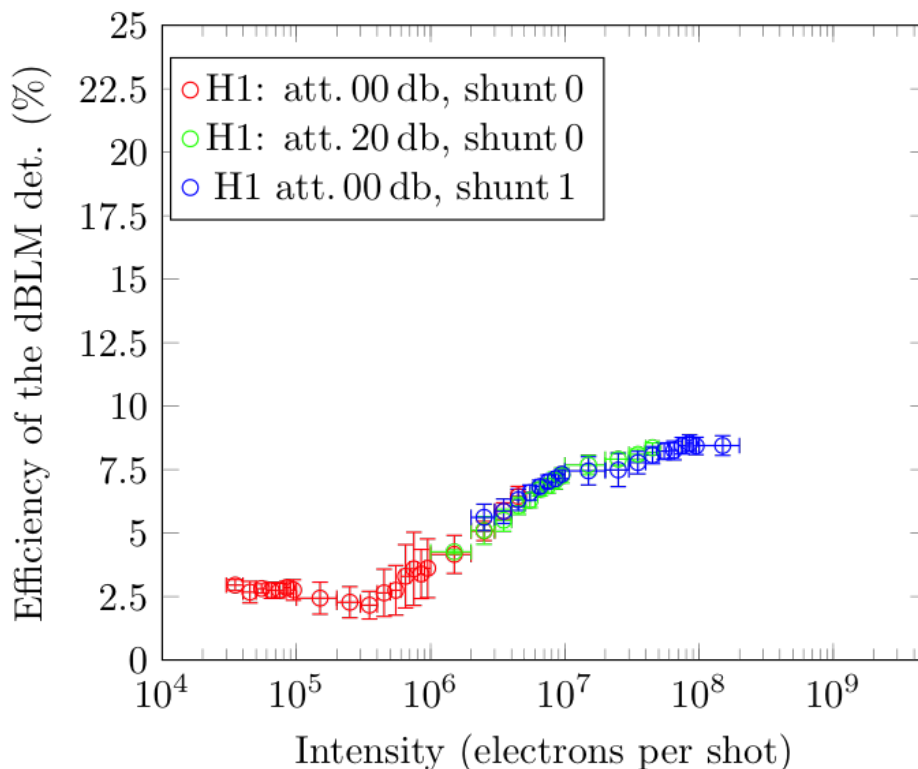


Fig. 9.17: Measured efficiency of H1 vs intensity. The change in efficiency can be explained by changing the scraper positions during data taking. The plateau at low intensities (red) is due to irradiation of an area with lower efficiency in the diamond material. This is a specific effect of the poly-crystalline material.

above, as the scrapers were moved during data taking. Also during 1×10^6 and 4×10^6 they were moved. The red points were measured at another date with different settings of the beam line. For the rest of the measurement the scrapers were moved before the data taking. This detector has a mean efficiency of 10.7 %.

A summary of the efficiencies for the three detectors is shown in Table 9.5. For the next beam time, it should be required to ensure a constant irradiation of the full detector surface, also changing the scraper positions during data taking should be avoided.

Tab. 9.5: Measured Efficiency and the standard deviation of the tested dBLMs.

Detector	Efficiency (%)	Std (absolute %)
H1	5.65	2.17
H2	9.21	1.84
H3	10.68	2.31

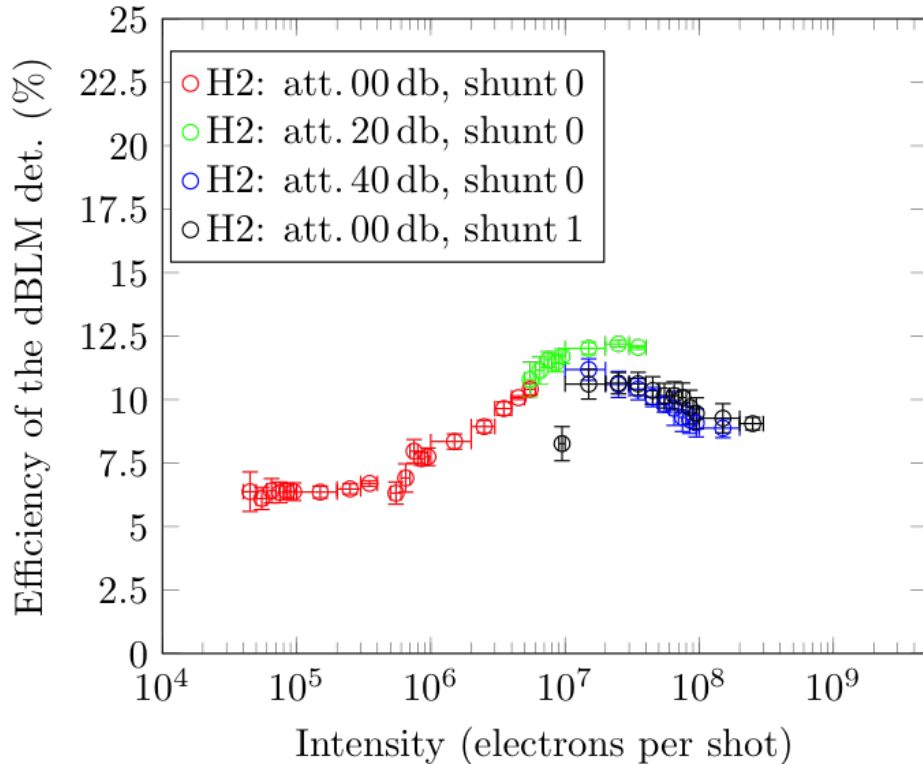


Fig. 9.18: Measured efficiency of H2 vs. intensity.

9.3 Applications of dBLMs

9.3.1 Alignment

In the second experiment in HiradMat 2012 a crystal, in the future maybe used as primary deflectors in the LHC collimation system, was irradiated to measure their robustness and integrity and to evaluate the risk associated to the installation of such a crystal in the LHC. For this experiment 500 μm thick polycrystalline diamond based particle detectors were used for the first time to align the crystal to the beam. The detectors were installed symmetrically to the beam axis on the target tank. Figure 4.18 shows the experimental setup. The red rectangles indicate the position of the dBLM. The left one is already installed, the right detector support is still empty.

A stainless steel strip fixed in a defined distance from the crystal was installed for alignment purposes. The steel stripe was moved through the beam, with the strip in the beam, secondary particles were created and then detected by two diamond detectors located downstream left and right side of the beam axis. Figure 9.20 shows the normalized to bunch intensity peak voltage of the diamond detectors versus position of the steel strip for different step sizes. At the maxima of curve the strip was placed in the beam producing the highest amount of shower particles, which were detected by the diamond detector. It is to be noted, that the detectors have a different efficiency, therefore the signal strength is different.

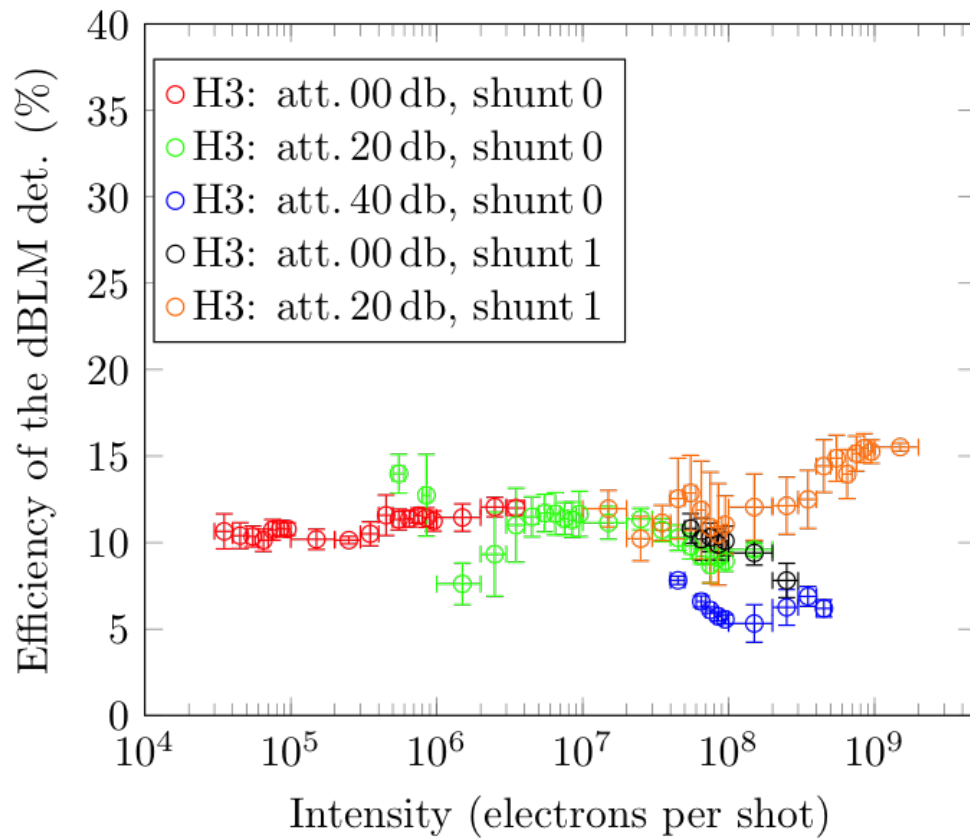


Fig. 9.19: Measured efficiency of H3 vs. intensity. The 50 Ohm limitation is visible in the blue data points. Changing scraper positions during data taking explains the oscillations at 10^6 electrons per shot (green) and in the high intensity range (orange).

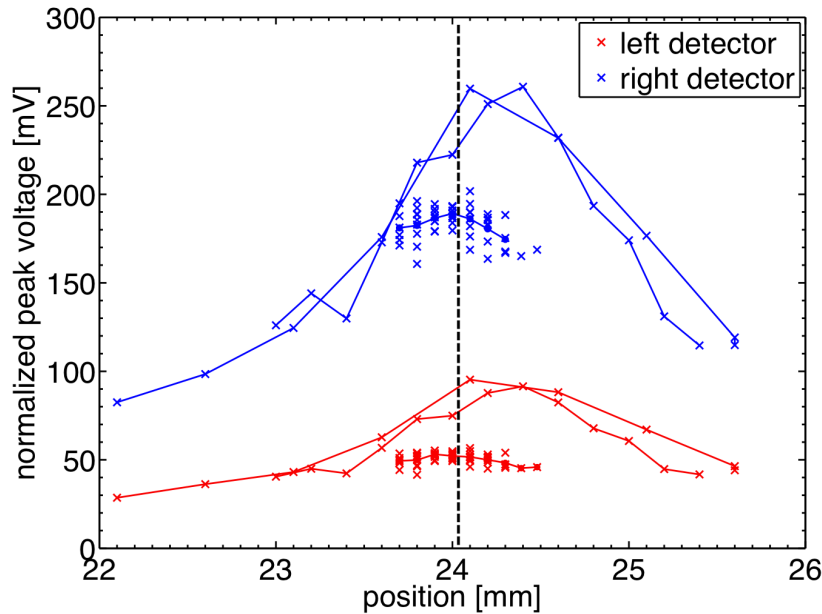


Fig. 9.20: Usage of diamond detectors as an alignment tool. In this case, a stainless steel strip was moved (with different step sizes) through the beam. The signal of two detectors (in red: downstream left, in blue: downstream right) is plotted versus position of the strip.

9.3.2 Online tunneling measurement

Unfortunately the discharge of the high-voltage capacitor during the HiRadMat experiment was so strong that it results in a decrease of the efficiency of the dBLMs. The time constant of the capacitor was too slow compared to the irradiation duration. Therefore the capacitor does not recharge during the irradiation. In addition, the limitations due to a 50 Ohm read-out system were not known during the experiment. For further experiments, the capacitor in the dBLM should be increased to its maximum and the tested shunt system should be used. Another possibility would be to mount the dBLMs with a higher distance from the beam axis, the disadvantage of this method would be the decrease of resolution. With these methods an online analysis of the hydrodynamic tunneling effect should be observable.

9.3.3 Bunch structure measurements around LHC

Diamond based particle detectors are also installed around LHC to measure the bunch-by-bunch losses during operation. These measurements were taken with the pCVD with a time resolution of 1 ns. Partially the signals were amplified with +20 or +40 dB. The dBLMs are installed at:

- Injection regions (IR2 and IR8) to observe losses during injection caused by injection oscillations.
- At the dump region (IR6) to detect losses due to un-bunched protons in the abort gap. These protons are lost during the rise time of the MKD current.

- In the collimation region (IR7) to study various losses, like beam instabilities and UFO events. During 2012 run several UFO events with a time resolution of ~ 1 ns were observed with the these dBLMs [61].

9.3.4 Abort gap monitoring

dBLMs are also used as a novel method of monitoring the abort gap population. These detectors will detect the interactions of protons in the abort gap with neon gas, injected in the beam pipe by the beam gas ionization monitors (BGI), located at IR4. In these special shaped beam chambers a pressure bump is created by neon gas. The particles of the beam collide with the neon gas atoms in the BGI and create secondary showers. By measuring the rate of the showers impacting on the dBLM, the abort gap population can be calculated if the neon gas pressure is known [100].

To realize this monitoring setup a detector with a high time resolution and ideally the ability of detecting single particles is a precondition. This can be reached by using single crystalline CVD diamond, which were already used at the LHC and in the CMS experiment during the first run. These detectors have an efficiency of above 95 %. The setup has been installed on both beams. During the commissioning phase of the LHC measurements this method will be tested in a dedicated MD time. The results will be described in another PhD thesis [101].

9.4 Future work - CALIFES

As the dBLMs shows different efficiencies, it is planned to characterize every dBLM with an electron beam directly at CERN. A test stand is located at Two-beam Test-stand (TBTS), which is a part of the CLIC Test Facility CTF3 [3], At this test facility the two-beam acceleration scheme is studied. A high frequency electron beam (the drive beam) is sent to a Power Extraction Structure (PETS). The PETS transfers the extracted beam energy into an RF structure where it is used to accelerate the so called probe beam. The detector test stand is located at a beam line previously used as dump line for the probe beam. The electrons have an energy of 180 MeV, the bunch intensity can be adjusted in the range of 1×10^9 and 1×10^{13} by attenuating the optical density on the source laser used to drive the gun photocathode. As a reference detector the previous dump block can be used as a Faraday cup. However the present instrumentation (beam charge monitor) is not yet adapted to bunch intensities below 5×10^{10} . The beam size can be 35 micrometers (σ_x or σ_y), especially with low charge the emittance is in the order of 4 mm.mrad. The necessary cabling for the test stand (signal cables, motor control cables for linear stages) is already installed, also the support system for the detector fixation is on place. Figure 9.21 and Figure 9.22 show the beam line before and after the installation of the diamond detector support. A movable target to reduce the bunch intensities by at least 3 orders of magnitude should be installed to allow the characterization of all types of dBLMs.



Fig. 9.21: Picture of the beam line before the modification. The kicker magnet to send the beam to beam line is shown on the right, followed by a screen station to monitor the beam profile and position. Further downstream the beam can be dumped on the dump block, which can be additionally used as Faraday-cup for intensity measurements.

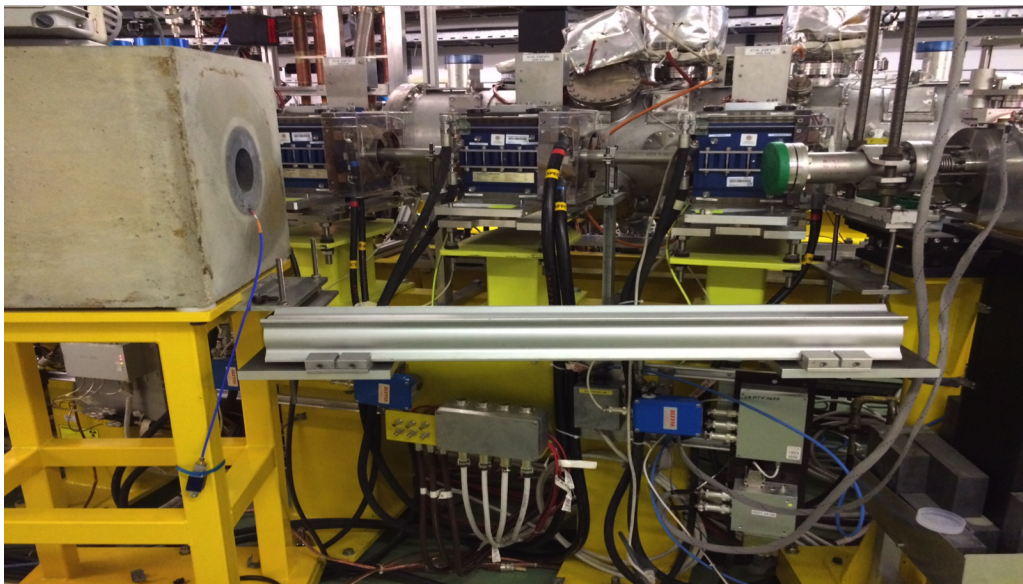


Fig. 9.22: Picture of the installed dBLM support in between the screen station and the beam dump. On the aluminum support dBLMs, linear stages and reference detectors can be installed.

10. CONCLUSION

The 362 MJ stored beam energy in each LHC beam is sufficient to melt ~ 500 kg of copper. Even a small fraction of this can damage or even destroy accelerator equipment. Machine protection systems should ensure the safe machine operation and handle all possible accidental cases. Knowing the damage potential of the stored beam is therefore a key parameter for the design of a machine protection system.

During this PhD different failure scenarios, their detection and the impact on machine operation were studied. The damage potential of proton beams due to the impact on a target for particle energies between 50 MeV and 40 TeV was evaluated as a function of beam size using the Monte-Carlo simulation code FLUKA. The damage itself was defined as the melting of 1 mm^3 of copper, which would cause fatal damage to a superconducting magnet. The results give safe beam intensities for this wide range of particle energies.

To correctly estimate the damage potential of bunched beams the so-called hydrodynamic tunneling effect has to be taken into account. It describes the density depletion along the beam axis due to energy deposition with the beam-target heating followed by a radially outgoing pressure wave. This effect was predicted in earlier simulations using LHC beam parameters. A penetration depth of 35m in solid copper was predicted. This effect and the previous simulation results were successfully verified with an experiment in CERN's HiRadMat facility. The experimental setup consisted of 3 copper cylinder targets. The targets were irradiated with up to 144 LHC type proton bunches, each at 440 GeV and an intensity of 1.15×10^{11} protons. The smallest beam sigma was 0.2 mm. Detailed visual and microscopic investigations were performed after a cool-down time of the experiment, including cutting the irradiated cylinders. It was evaluated that the beam had penetrated up to 85 cm the target. The first cylinder was cut longitudinally and a beam-made cone shaped hole was visible. The other cylinders showed a hole going through the cylinder. The last cylinder with a visible damage showed cracks and micro-cavities.

Iterative FLUKA and BIG2 simulations were carried out with the experimental beam parameters. The results of these simulations showed that a region of up to 90 cm on beam axis is above melting or even evaporation temperature. The results of the simulations were in very good agreement with the experimental results. In addition, the simulations predicted the existence of the cone-shaped hole in the first cylinder and the hole and cracks up to the last cylinder.

As the hydrodynamic tunneling will play a major role for the design of protection

elements and absorbers for high stored beam energy accelerators the studies were expanded by using the beam parameters for the Future Circular Collider (FCC). The FCC is a design study for a future circular collider. It consists of a 100 km circumference storage ring to accelerate protons up to particle energies of 50 TeV. The stored beam energy will reach 8.5 GJ per beam. The results showed that for a head-on impact the FCC proton beam would penetrate up to 350 m in solid copper. These simulation results are the starting point for future, un-conventional beam dumps, e.g. based on water.

The detection of accidental beam losses in case of (fast) failures is very important for machine protection. It is the basis for a fast reaction like a beam abort. Single crystalline diamond based beam loss monitors (dBLMs) were already used in the LHC experimental areas ATLAS and CMS to measure the beam quality. These high sensitive detectors were modified by using poly-crystalline detector material to withstand also higher loss levels. With their resolution in the nanosecond time range they are able to detect high beam losses with bunch-by-bunch resolution in the LHC and its accelerator chain. During this thesis they were used for the first time in damage experiments in the HiRadMat facility, to allow an online observation of the beam impact and to align the target to the beam.

To characterize the dBLMs response with beam three measurement campaigns were conducted at the Beam Test Facility (BTF) at the Istituto Nazionale per la Fisica Nucleare (INFN), Frascati, Italy. For these experiments a specially designed set-up was developed including detector holders, beam collimator, reference detectors and DAQ. During these experiments, the dBLMs were characterized between $5E4$ and $2E9$ charges per bunch. For high bunch intensities saturation effects caused by the combination of detector and 50 Ohm read-out system were found and studied. To avoid exceeding this limit in the future, a 1 Ohm shunt system was tested during this diamond detector characterization. With this new system no saturation effects and DAQ limitations were observed. This can be applied for dBLMs installed in a high-fluence environment. A variation of detector efficiency up to a factor two was found in the experiments. This variation can be explained by the poly-crystalline detector material and shows that it is necessary to characterize diamond based particle detectors before their use for absolute loss measurements.

Following the successful beam based characterization at high bunch intensities, detectors of this type were installed in the LHC collimation, injection and extraction areas.

11. DEUTSCHE ZUSAMMENFASSUNG

Jeder der beiden Protonenstrahlen im LHC hat eine gespeicherte Energie von 362 MJ, womit man ca. 500 kg Kupfer schmelzen kann. Das sind zwei Größenordnungen mehr als in früheren Hochenergiespeicherringen. Schon ein Bruchteil dieser Energie kann zur Beschädigung oder Zerstörung von Beschleunigerausrüstung führen. Deshalb gewährleisten Maschinensicherheitssysteme den sicheren Betrieb des Beschleunigers und gegebenenfalls den Strahlabbruch im Fehlerfall. Für die Entwicklung von Maschinensicherheitssystemen für zukünftige Hochenergiespeicherringe ist es deshalb unerlässlich das Schadenspotential der Teilchenstrahlen zu kennen.

In der vorliegenden Doktorarbeit werden unterschiedliche Fehlerfälle, ihre Detektion und Auswirkungen auf den Betrieb des Beschleunigers untersucht. Das Schadenspotential der Protonenstrahlen bei Interaktion mit Materie im Teilchenenergiebereich von 50 MeV bis 40 TeV wurde, in Abhängigkeit von der Strahlgröße, mit Hilfe des Monte-Carlo-Simulationskodes FLUKA analysiert. Als Zerstörungsgrenze wurde das Schmelzen von 1 mm³ Kupfer gewählt, welches zu einer gravierenden Beschädigung eines supraleitenden Magneten führen würde. Für jede der Teilchenenergien wurde dann aus den Simulationsergebnissen die maximale Verluststraten berechnet.

Der Teilchenstrahl ist üblicherweise in Teilchenpakete unterteilt, die sogenannten Bunche. Um in diesem Fall das Schadenspotential des Teilchenstrahles abzuschätzen muss der sogenannte hydrodynamische Tunneleffekt berücksichtigt werden. Dieser Effekt verursacht eine Verringerung der Materialdichte entlang der Strahlachse aufgrund der Interaktion von Strahl und Materie und der daraus resultierenden, radial ausgehenden Druckwelle. Dieses Verhalten wurde schon in älteren Simulationen mit LHC Strahlparametern gezeigt wobei eine maximale Eindringtiefe von 35 m in Kupfer vorhergesagt wurde. Zum ersten Mal wurde der hydrodynamische Tunneleffekt und die beschriebenen Simulationsergebnisse durch ein Experiment an CERNs HiRadMat Anlage bestätigt. Der Versuchsaufbau bestand aus 3 parallelen Reihen von jeweils 15 Kupferzylindern, die mit Strahlen mit bis zu 144 Protonenbunchen mit jeweils 1.5E11 Protonen pro Bunch, einer Energie von 440 GeV und einem Bunchabstand von 50 ns beschossen wurden. Dabei wurden Strahlgrößen von $\sigma = 0.2$ mm und $\sigma = 2$ mm verwendet. Bild 11.1 zeigt ein Foto des experimentellen Aufbaus.

Diese Doktorarbeit umfasst detaillierte visuelle und mikroskopische Analysen der Kupferzylinder, die auch das Aufschneiden eines Teils der bestrahlten Zylinder einschliesst, um das Schadensbild im Detail zu untersuchen. Eine Eindringtiefe des Teilchenstrahls von 85 cm wurde gemessen. Im Inneren des ersten Zylinders wurde ein vom Strahl produzierter kegelförmiger Hohlraum sichtbar (siehe Bild 11.2). Bei

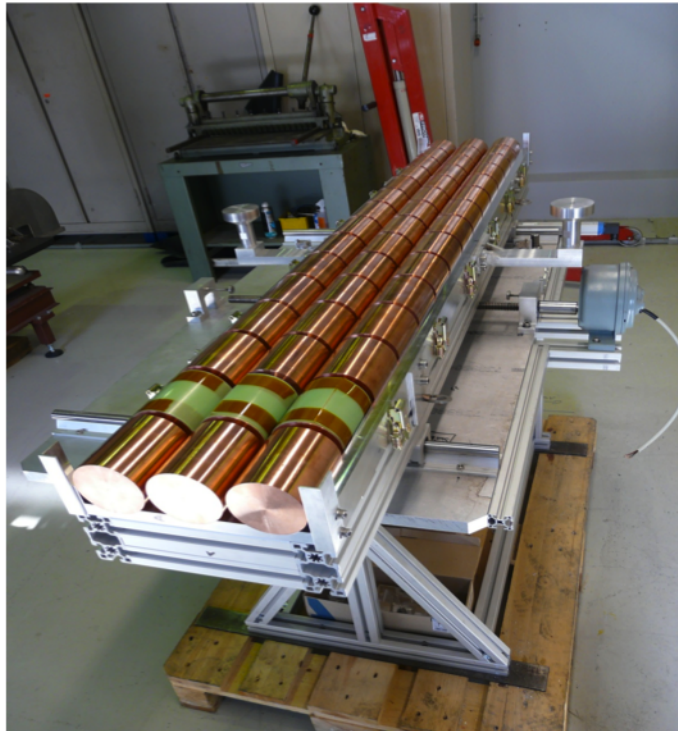


Fig. 11.1: Versuchsaufbau vor dem Einbau in HiRadMat. Ein Aluminiumgehäuse enthält 3 Reihen bestehend aus 15 Kupferzylindern, mit einem Radius von je 4 cm und einer Länge von 10 cm.

den folgenden Zylindern wurde ein durchgehender Hohlraum gefunden. Bild 11.3 zeigt das Foto der Vorder- und Rückseite des zweiten Zylinders. Die jeweils letzten Zylinder mit sichtbaren Schäden (Zylinder Nr. 6, 8 und 9) zeigten Risse und kleine Hohlräume auf der Strahlachse.

Parallel zu den mechanischen Untersuchungen wurden iterative Simulationen mit den Codes FLUKA und BIG2 unter Verwendung der experimentellen Strahlparameter durchgeführt. Die Ergebnisse dieser Simulationen zeigen, dass das Kupfer auf der Strahlachse über eine Länge von bis zu 90 cm zum Schmelz- oder gar dem Verdampfungspunkt erhitzt wurde. Eine graphische Darstellung der Simulationsergebnisse für Temperatur und Dichte ist in Bild 11.4 zu sehen. Die Ergebnisse der Simulationen stimmen sehr gut mit den experimentellen Ergebnissen überein. Auch der kegelförmige Hohlraum im ersten Zylinder und die Risse im letzten beschädigten Zylinder werden gut von der Simulation reproduziert.

Wegen der grossen Bedeutung des hydrodynamischen Tunneleffekts für die Entwicklung von Absorberelementen für Hochenergiebeschleuniger wurden die Simulationen auf Strahlparameter des sogenannten Future Circular Colliders (FCC) ausgedehnt. Der FCC ist eine Designstudie eines zukünftigen Beschleunigers, bestehend aus einem 100 km langen Speicherring in dem zwei Teilchenstrahlen auf bis zu 50 TeV beschleunigt und in Kollision gebracht werden sollen. Dabei erreicht die in ei-

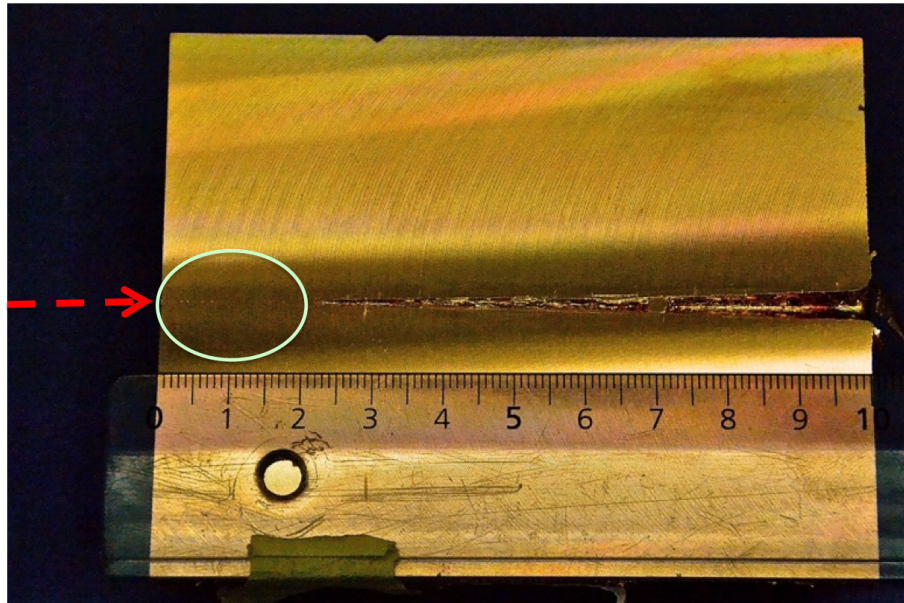


Fig. 11.2: Bild des aufgeschnittenen ersten Zylinders. In den ersten 2,3 cm kann man Mikrohöhlräume erkennen, denen ein kegelförmiger Hohlraum folgt.

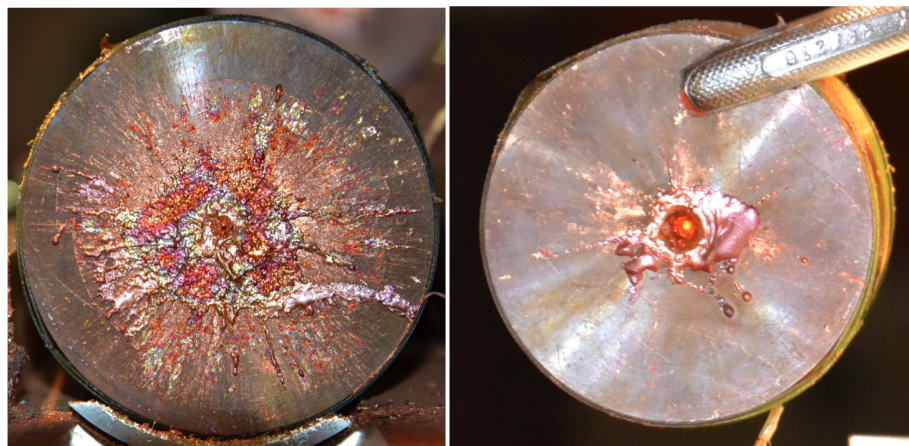


Fig. 11.3: Bild der Vorder- (links) und Rückseite (rechts) des zweiten Zylinders. Auf der Vorderseite ist erstarrter Kupferauswurf aus dem ersten Zylinder erkennbar. Die Rückseite zeigt den vom Strahl erzeugten Hohlraum. Das Kupfer in diesem Zylinder war gasförmig und wurde unter hohem Druck ausgestossen.

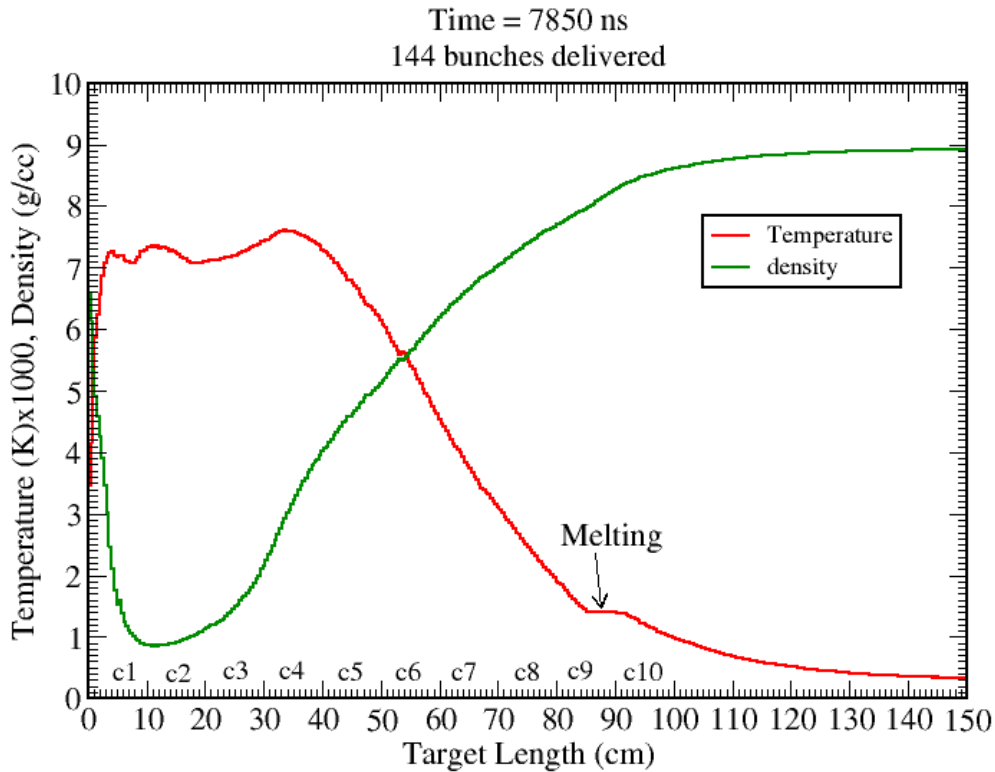


Fig. 11.4: Die Simulationsergebnisse für die dritte Reihe von Kupferzylindern ($\sigma = 0,2\text{cm}$, 144 Bunche) zeigen, dass das Kupfer auf der Strahlachse über eine Länge von 90 cm eine Temperatur oberhalb des Schmelzpunktes erreicht hat. Dieses Ergebnis stimmt mit den experimentellen Ergebnissen sehr gut überein.

nem der beiden Teilchenstrahlen gespeicherte Energie 8,5 GJ. Die Simulationsergebnisse zeigen, dass der FCC Protonenstrahl, im Fall eines Frontaleinschlags, Kupfer auf einer Länge von 350 m schmelzen, bzw. verdampfen würde. Die Dichtereduktion entlang der Strahlachse für verschiedene Simulationsschritte ist in Bild 11.5 zu sehen.

Die Messung von schnellen Strahlverlusten, die durch Fehler während des Beschleunigerbetriebs auftreten, ist die Basis für die Einleitung schneller Interventionen wie z.B. ein Strahlabbruch und damit wesentlich für die Maschinensicherheit. Strahlverlustmonitore auf Diamantbasis (dBLMs) werden bereits in den großen LHC Experimenten ATLAS und CMS verwendet, um die Strahlqualität zu bestimmen. Um die Empfindlichkeit dieses Detektorentyps zu reduzieren und damit höhere Strahlverluste messen zu können, wurden polykristalline Diamantblättchen mit einer Dicke von nur $100\mu\text{m}$ verwendet. Mit ihrer Zeitauflösung im Nanosekundenbereich können dBLMs die Strahlverluste pro Teilchenbunch messen. Im LHC und dessen Beschleunigerkette werden sie an bestimmten Punkten zur Beobachtung von Verlusten eingesetzt.

Im Rahmen dieser Doktorarbeit wurden sie zum ersten Mal bei Experimenten zur Bestimmung des Schadenspotentials von Hochenergieteilchenstrahlen in CERNs HiRadMat Anlage verwendet, um eine Online-Messung der Interaktion von Teilchenstrahl mit dem Target Material zu ermöglichen. Weiterhin wurden dBLMs zur Ausrichtung des Targets zum Teilchenstrahl verwendet. Zur Charakterisierung der dBLMs wurden während dieser Doktorarbeit drei Messreihen an der sogenannten Beam-Test-Facility (BTF) am Istituto Nazionale per la Fisica Nucleare (INFN), Frascati, Italien durchgeführt. Der Messaufbau für diese Experimente bestand aus Detektorhalter, Kollimator, Referenzdetektoren (Standard LHC Ionisationskammer) und Datenerfassungssystem. Während dieser Messungen wurden die dBLMs für Intensitäten von $5E4$ und $2E9$ Ladungen pro Teilchenbunch charakterisiert. Bild 11.6 zeigt die Signale von drei Detektoren im oben genannten Intensitätsbereich.

Bei Intensitäten oberhalb von $5E8$ pro Bunch wurden Sättigungseffekte, verursacht durch die Kombination des Detektors und des 50 Ohm-Auslesesystems, beobachtet und untersucht. Ein 1 Ohm Shuntsystem zur Vermeidung dieser Sättigungseffekte wurde während der Charakterisierung erfolgreich getestet. Weiterhin zeigten die Messungen eine Variation der Detektoreffizienz zwischen einzelnen Detektoren von bis zu einem Faktor zwei. Diese kann durch das polykristalline Detektormaterial erklärt werden und verdeutlicht die Notwendigkeit der Charakterisierung jedes einzelnen Detektors. Nur auf diese Weise kann die Teilchenfluenz durch den Detektor absolut kalibriert werden.

Nach ihrer erfolgreichen Charakterisierung wurden diese und vergleichbare Detektoren im LHC in den Kollimations-, Injektions- und Extraktionregionen und im SPS und PS bei der Strahlextraktion installiert.

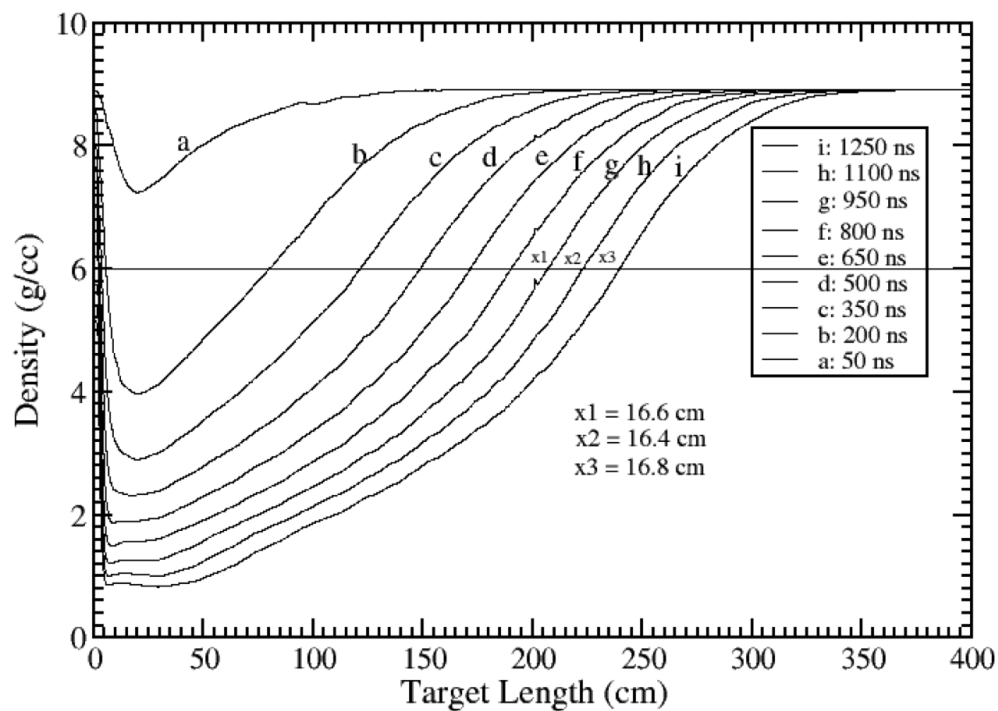


Fig. 11.5: Dichtereduktion in einem Kupfertarget entlang der Strahlachse als Funktion der Zeit. Die Simulation wurde mit FCC Strahlparameter durchgeführt. In den ersten 350 ns wird die Energie in einem sehr kleinen Volumen abgegeben, was zu einer erhöhten Dichtereduktion pro Zeitintervall im Vergleich zu späteren Zeitpunkten führt, bei welchen die Energieabgabe auf ein größeres Volumen verteilt wird. Nach ungefähr 800 ns erreicht die Dichtereduktion pro Zeitintervall einen konstanten Wert. Dieser Bereich ist markiert mit den Linien x_1 , x_2 and x_3 bei einer Dichte von 6 g/cm^3 . Unter Verwendung des Zeitintervalls Δt von 450 ns zwischen den Dichtekurven f und i kann die Ausbreitungsgeschwindigkeit der Dichtereduktion berechnet werden. Eine Eindringtiefe von 350m wurde für 50 TeV Strahlenergie ermittelt.

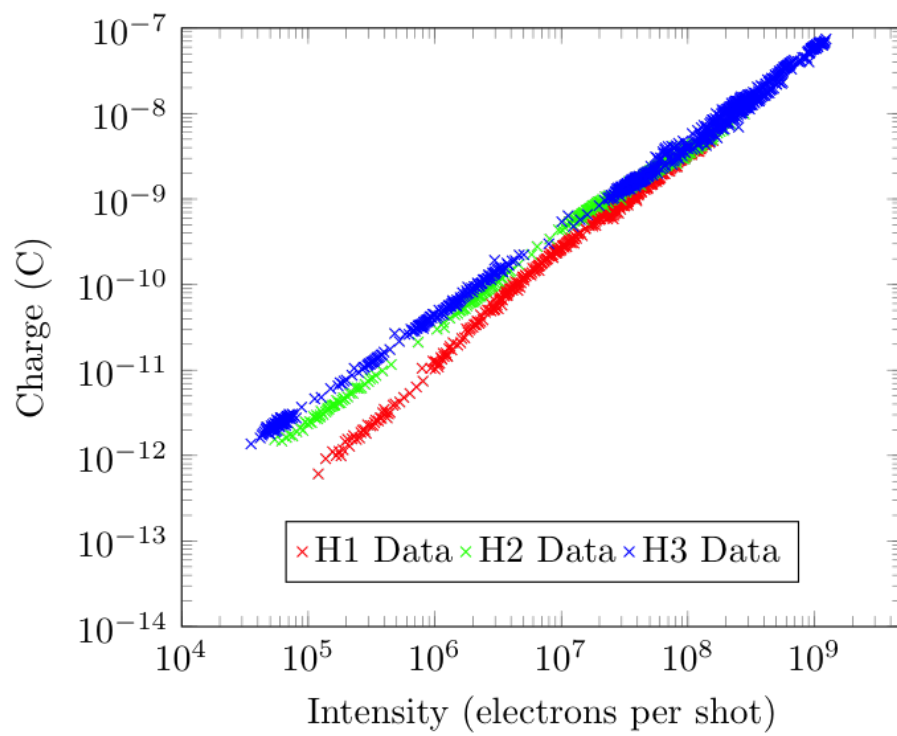


Fig. 11.6: Signale von drei dBLMs (H1, H2 and H3). Auf der x-Achse ist die gemessene Intensität des Referenzdetektors aufgetragen, die y-Achse zeigt die gemessene Detektorladung des dBLMs.

12. ACKNOWLEDGEMENTS

Firstly I would like to thank my supervisor Prof. Dr. Ulrich Ratzinger from the institute for applied physics (IAP) at the Goethe-University Frankfurt for his constant support through the different stages of my scientific career and during the process of writing this thesis. I am thankful for his encouragement and the interesting discussions we had over the years.

I owe deep gratitude to my CERN supervisor, Dr. Daniel Wollmann, for giving me the possibility to write this thesis at CERN, for his support, his critical comments, discussions and scientific supervision. I appreciated the balance he established between mentoring and letting me work autonomously. In addition, I would like to thank Dr. Rüdiger Schmidt and Dr. Arjan Verweij for their continuous support and advice.

Great support was given by the whole MPE-PE section, thanks for the helpful discussions during all the meetings. Especially I want to thank my office mates, Dr. Vera Chetvertkova, Andrea Appolonio, Tobias Griesemer and Vivien Raginel.

I wish to thank my colleague Oliver Stein for the friendship, the great collaboration and the assistance during the diamond characterization. It is a pleasure to thank Dr. Erich Griesmayer from CIVIDEC, Maria Hempel, Christina Weiss and Moritz Guthoff for their help and sharing their deep knowledge of the diamond detector world.

The hereby presented study of the hydrodynamic tunneling process required the expertise of Dr. Naeem Tahir from GSI. I owe deep gratitude to him as he always patiently answered my questions. I would like to thank him for his contribution, his support and all the fruitful discussions.

Many other people were involved in this work, I would like to thank Dr. Bernd Dehning, Dr. Eduardo Nebot, Raymond Tissier, Bernard Collignon, Ewald Effinger for the beam loss monitor support. Dr. Anton Lechner and Dr. Francesco Cerutti for all the FLUKA-questions. Dr. Adrian Fabich and Dr. Nikos Charitonidis from the HiRadMat team. Alexandre Gerardin, Dr. Stefano Sgobba, Jacky Tonoli for their advice in cutting the cylinders. Kurt Weiss, Chris Theis, Helmut Wincke for all the radio-protection related questions. A big thank you goes to my friends Frank, Christin, Michaela, Miriam, Oliver, Bastian, Janet, Vera and Daniel.

I thank the Wolfgang-Gentner-Programme of the Bundesministerium für Bildung

und Forschung for the financial support and Dr. Michael Hauschild, the coordinator of the programme, for his assistance and advice.

Finally, I am grateful for my family, Sonja and Manus, for their love and the support during these exciting but stressful times. Thank you very much!

13. ACRONYMS USED IN THIS PHD THESIS

BCM: beam condition monitor
BIC: beam interlock controller
BIS: beam interlock system
BLM: beam loss monitor
BTF: beam test facility
BPM: beam position monitor
CCD: charge collection distance
CCE: charge collection efficiency
CLIC: compact linear collider
dBLM: diamond beam loss monitor
FCC: future circular collider
HiRadMat: High radiation to materials
icBLM: ionization chamber beam loss monitor
INFN: istituto nazionali die fisica nucleare
IP: interaction point
IR: insertion region
LBDS: LHC beam dumping system
LHC: large hadron collider
LNF: laboratory nazionali di frascati
MKB: dilution kicker magnet
MKD: LHC extraction kicker magnet
MKI: injection kicker magnet
MSE: extraction septum magnet
MSI: injection septum magnet
SPS: super proton synchrotron
TCDQ and TCDS: target collimator dump for beam extraction
TCP: target collimator primary
TCS: target collimator secondary
TPSG: septum protection absorber block
TL: transfer line
TDE: LHC beam dump block
TDI: beam absorber for injection
QPS: quench protection system
WCM: wall current monitor
WDM: warm dense matter

CURRICULUM VITAE

Persönliche Daten

Name Florian Burkart
Geburtsdatum 20. Mai 1984
Geburtsort Oberkirch, Deutschland

Ausbildung

2003 Abitur

2006 -2012 Studium der Physik, Goethe Universität Frankfurt

2010 Abschluss: Bachelor of Science,
Bachelorarbeit: Conceptual design of an experimental setup
to measure the magnetic field strength of a superconducting undulator,
geschrieben am Karlsruher Institut für Technologie, Karlsruhe, Deutschland.

2012 Abschluss: Master of Science,
Masterarbeit: Beam Loss and Beam Shape at the LHC
collimators, geschrieben am CERN, Genf, Schweiz.

2012 - 2015 Doktorarbeit am CERN, Genf, Schweiz.
Titel: Expected damage to accelerator equipment due to the impact
of the full LHC beam: beam instrumentation, experiments and simulations.

Akademische Lehrer:

B. Ahrens, A. Bechthold, C. Blume, R. Dörner, G. Franchetti, C. Greiner, C. Gros, W. Hofstetter,
M. Huth, J. Jacoby, M. Lang, W. Mäntele, J. Müller, H. Podlech, R. Reifarth, U. Ratzinger,
H. Roskos, A. Schempp, J. Stroth, W. Toll, J. Weidmann

BIBLIOGRAPHY

- [1] O. Bruening, P. Collier, S. Myers et al., The LHC design report, v1. The LHC Main Ring, CERN, Geneva, 2004.
- [2] R. Schmidt, Introduction to accelerator protection course. Joint International Accelerator School on Beam Loss and Accelerator Protection, Newport Beach, USA, 2014.
- [3] L. Linssen et al., Physics and Detectors at CLIC: CLIC Conceptual Design Report, 2012.
- [4] A. Caldwell et al., AWAKE Design Report: A Proton-Driven Plasma Wakefield Acceleration Experiment at CERN, 2013.
- [5] <http://home.web.cern.ch/about/accelerators/antiproton-decelerator>
- [6] www.ams02.org
- [7] www.isolde.web.cern.ch
- [8] LEP design report, CERN, 1984.
- [9] CERN accelerator complex, www.espace.cern.ch/acc-tec-sector.
- [10] M. Benedikt et al., Challenges for highest energy circular colliders, in proceedings of IPAC 2014, Dresden, Germany, 2014.
- [11] fcc.web.cern.ch
- [12] W. Demtroeder, Experimentalphysik 4: Kern-, Teilchen- und Atomphysik, Springer-Verlag 2005.
- [13] K Nakamura, PD Group, Review of particle physics., Journal of Physics G: Nuclear and Particle Physics 37 (7A), 075021
- [14] K. A. Olive et al., Particle Data Group, Chin. Phys. C, 38, 090001 (2014)
- [15] A. Ferrari and P.R. Sala, The Physics of High Energy Reactions, in Nuclear Reaction Data and Nuclear Reactors Physics, Design and Safety, 1996.
- [16] H.A.Bethe, Zur Theorie des Durchgangs schneller Korpuskularstrahlen durch Materie, Ann. Physik, vol. 5, pp. 325-400, 1930. Selected Works of Hans A. Bethe, World Scientific, Singapore 1996, p. 77-154.

- [17] H.A. Bethe, Bremsformel fuer Elektronen relativistischer Geschwindigkeit, Z. Phys., vol. 76, pp. 293-299, 1932.
- [18] F. Bloch, Bremsvermoegen von Atomen mit mehreren Elektronen Z. Phys., vol. 81, pp. 363-376, 1933.
- [19] G. Z. Molire, Theorie der Streuung schneller geladener Teilchen II. Mehrfach- und Vielfachstreuung, 1948.
- [20] Y.S. Tsai, Pair production and bremsstrahlung of charged leptons., Rev. Mod. Phys., vol. 46, p. 815, 1974.
- [21] H.A. Bethe, Molires Theory of Multiple Scattering, Physical Review, vol. 89, pp. 1256-1266, March 1953. AA (Laboratory of Nuclear Studies, Cornell University, Ithaca, New York).
- [22] Gary J. Russell, Los Alamos National Laboratory, Los Alamos, New Mexico, Spallation Physics - An Overview, 1CANS-XI International Collaboration on Advanced Neutron Sources KEK. Tsukuba. October, 1990
- [23] S. Atzeni, J. Meyer, The Physics of inertial fusion: Beam Plasma Interaction, Hydrodynamics, Hot Dense Matter, 2009
- [24] N.A. Tahir et al., Prospects of warm dense matter research at HiRadMat facility at CERN using 440 GeV SPS proton beam, Tech. Rep. EuCARD-PUB-2013-005, 2013.
- [25] N. A. Tahir et al., The Large Hadron Collider and the Super Proton Synchrotron at CERN as Tools to Generate Warm Dense Matter and Non-Ideal Plasmas, Tech. Rep. EuCARD-PUB-2011-017, 2011.
- [26] N. A. Tahir et al., Generation of warm dense matter and strongly coupled plasmas using the High Radiation on Materials facility at the CERN Super Proton Synchrotron, no. EuCARD-PUB-2009-032, 2009.
- [27] N.A. Tahir et al., J. Appl. Phys, vol. 97, p. 083532, 2005.
- [28] R. Schmidt, J. Blanco Sancho, F. Burkart, D. Grenier, D. Wollmann, N.A. Tahir, A. Shutov and A.R. Piriz, Phys. Plasmas, vol. 21, p. 080701, 2014.
- [29] N.A. Tahir, F. Burkart, A. Shutov, R. Schmidt, D. Wollmann and A.R. Piriz, Phys. Rev. E, vol. 90, p. 063112, 2014
- [30] N. Tahir et al., J. Appl. Phys, vol. 97, p. 083532, 2005.
- [31] N. Tahir et al., Phys. Rev. E, vol. 79, p. 046410, 2009.
- [32] N. Tahir et al., Phys. Rev. Special Topics Accel. Beams, vol 15, p. 051003, 2012.

-
- [33] T.T. Bohlen, F. Cerutti, M.P.W. Chin, A. Fasso, A. Ferrari, P.G. Ortega, A. Mairani, P.R. Sala, G. Smirnov, and V. Vlachoudis, The FLUKA Code: Developments and Challenges for High Energy and Medical Applications, Nuclear Data Sheets 120, 211-214 (2014)
- [34] A. Ferrari, P.R. Sala, A. Fasso, and J. Ranft, FLUKA: a multi-particle transport code, CERN-2005-10 (2005), INFN TC 05.11, SLAC-R-773
- [35] <http://www.fluka.org/fluka.php>
- [36] V.E. Fortov et al., Nucl. Sci. Eng. 123 (1996) 169.
- [37] I.V. Lomonosov, Laser Part. Beams 25 (2007) 567.
- [38] S. Evrard et al., HiRadMat safety file - descriptive part, EDMS 1145711, 20011.
- [39] I. Efthymiopoulus et al., HiRadMat facility overview, AMAT workshop, CERN, 2013.
- [40] S. Montesano et al., HiRadMat experiment scientific motivation, EDMS 1213282, 2015.
- [41] C. Baud et al., TPSG4 validation at HiRadMat, HiRadMat scientific board meeting, April 2012.
- [42] Private communication with N. Tahir, GSI, Darmstadt, Germany.
- [43] J. Blanco Sancho, Machine Protection and High Energy Density States in Matter for High Energy Hadron Accelerators, CERN-THESIS-2014-041, 2014
- [44] C. Kurfuerst, Quench protection of the LHC quadrupole magnets, CERN-Thesis-2010-070.
- [45] R. Schmidt, Machine protection issues and strategies, EPAC 2004, Lucern, Switzerland.
- [46] A. Verweij, Heat Capacity (C_p) values of Copper as a function of the temperature
- [47] V. Kain et al., Beam induced damage-What is a safe beam?, Proceedings of Chamonix 2009 Workshop on LHC Performance
- [48] V. Kain et al. Material Damage Test with 450 GeV LCH-Type Beam
- [49] B. Goddard et al., Damage During 2004 High Intensity SPS Extraction
- [50] G. Rosell, Damage limits of accelerator equipment, Summer student report, 2014.
- [51] Proceedings of First BTF Users Workshop, 6th - 7th May 2014, INFN, Frascati, Italy.

- [52] BTF documentation, <http://wiki.infn.it/struttura/Inf/da/btf/>
- [53] de.wikipedia.org/wiki/Diamant
- [54] C. Weiss, A CVD diamond detector for (n,α) cross-section measurements. CERN-THESIS-2014-101.
- [55] J. W. Anthony et al., Handbook of mineralogy, Mineralogical Society of America (1990).
- [56] J. Koike et al., Displacement threshold energy for type IIa diamond, Applied physics letters, 60:1450-2452 (1992).
- [57] A. R. Lang, The properties of diamond, Academic Press, London (1979).
- [58] J. E. Field, The properties of natural and synthetic diamond, Academic Press, London (1979).
- [59] L.S. Pan et al., Diamond: Electronic properties and applications, Kluwer Academic Publ., Boston, MA (1995).
- [60] B. Dehning et al., Overview of LHC beam loss measurements, Proceedings of IPAC 2011, San Sebastian, Spain.
- [61] M. Hempel et al., Bunch to bunch loss diagnostics with diamond detectors at the LHC, Proceedings of Advanced Beam Dynamics Workshop on High-Intensity and High-Brightness Hadron Beams, 2012.
- [62] F. Burkart et al., Diamond particle detector properties during high-fluency material damage tests and their future application for machine protection in the LHC, Proceedings of IPAC 2013, Shanghai, China.
- [63] J. Isberg, CVD Diamond for electronic devices and sensors, Chapter 2, John Wiley and Sons, Ltc. (2009)
- [64] E. Griesmayer, Measurements with diamond detectors at temperatures up to 520 K.
- [65] M. R. Bartosik, Cryogenic beam loss monitors for a future LHC, 3rd oPAC topical workshop on beam diagnostics, 2014.
- [66] H. Pernegger et al., Charge carrier properties in synthetic single-crystal diamond measured with the transient-current technique, J. Appl. Physics, 97(073704), 2005.
- [67] H. Pomorski et al., Development of single-crystal CVD diamond detectors for spectroscopy and timing, Phys. Status Solidi A, 203(12):3152-3160, 2006.
- [68] W. Shockley, Currents to conductors induced by a moving point charge, J. Appl. Physics, 9:635-636 (1938).

-
- [69] E. Griesmayer, www.cividec.at and private communication.
- [70] M. Guthoff, Radiation Damage to the diamond-based Beam Condition Monitor of the CMS Detector at the LHC. CERN-THESIS-2014-216.
- [71] J. Asmussen et al., Diamond films handbook, Marcel Dekker, Inc., 2002.
- [72] R. Mildred et al., Optical engineering of diamond, Wiley-VCH, 2013.
- [73] C. Canali et al., Electrical properties and performances of natural diamond nuclear radiation detectors, Nuclear instruments and methods A, 160:73-77, 1979.
- [74] F. Burkart et al., Comparison of the Results of a hydrodynamic tunneling experiment with iterative FLUKA and BIG2 simulations, in Proceedings of IPAC14, Dresden, Germany, 2014.
- [75] F. Burkart et al., Experimental and simulation studies of hydrodynamic tunneling of ultra-relativistic protons, Proceedings of IPAC 2015, Richmond, USA.
- [76] F. Burkart, Beam loss and beam shape at the LHC collimators. CERN-THESIS-2012-046.
- [77] R. W. Assmann, The final LHC collimation system, EPAC 2006, Edinburgh, GB.
- [78] R. W. Assmann et al., Requirements for the LHC collimation system. In Proceedings of EPAC 2002, Paris, France.
- [79] R. W. Assmann et al., The phased implementation of LHC collimation. In Proceedings of HHH, 2008.
- [80] C. Bracco, Commissioning scenarios and tests for the LHC collimation system, CERN-THESIS-2008.
- [81] R. Demolaize, Design and performance optimization of the LHC collimation system, Grenoble, 2006.
- [82] A. Bertarelli et al., The mechanical design for LHC collimators. In Proceedings of EPAC 2004, Lucerne, Switzerland.
- [83] R. W. Assmann, Summary of collimation upgrade plans. In Proceedings of EuCard, 2010.
- [84] HED on www-pls.llnl.gov
- [85] Rober Craig Group, Measurement of the inclusive jet cross section using the midpoint algorithm in run 2 at the collider detector at Fermilab, University of Florida, 2006
- [86] www.inspirehep.net/record/810115/files/
- [87] Density functional theory for warm dense matter, University of Florida.

- [88] O. Bruening, P. Collier, S. Myers et al., The LHC design report, Chapter 17, Beam Dumping System, CERN, Geneva, 2004.
- [89] www.lhc-machine-outreach.web.cern.ch/lhc-machine-outreachcomponents/beam-dump.htm
- [90] T. Baer et al., UFOs in the LHC, In Proceedings of IPAC 2011, San Sebastian, Spain.
- [91] J. Wenninger, Machine protection and operation for LHC, Joint accelerator school, Newport, USA, 2014.
- [92] The LHC quench protection system, CERN publication, DG-CO, BUL-NA-2009-103.
- [93] B. Todd, A beam interlock system for CERN high energy accelerator. PhD thesis, Brunel, London, 2006.
- [94] E. B. Holzer et al., Design of the beam loss monitoring system for the LHC ring. In Proceedings of EPAC04.
- [95] M. Stockner et al., Classification of the LHC BLM ionization chambers, In Proceedings of DIPAC07.
- [96] B. Dehning et al., First experience with LHC beam loss monitoring system. In Proceedings of PAC09.
- [97] E. Nebot, private communication.
- [98] E. Gschwendtner, PS-Booster Measurements for the LHC -BLM, October 2002, CERN.
- [99] E. Griesmayer et al., Diamond detectors for LHC, In Proceedings of IBIC2012, Tsukuba, Japan.
- [100] O. Stein et al., Feasibility study of monitoring the population of the CERN-LHC abort gap with diamond based particle detectors. In Proceedings of IPAC2015, Richmond, USA.
- [101] O. Stein, PhD thesis, to be published.